Reflective Phase Imaging of Ultra-Fast Laser-Induced Plasma Expansion on Solid Targets

Dissertation

submitted in fulfillment of the requirements for the degree of

Doctor rerum naturalium

in

Physics

at the

Faculty of Mathematics and Natural Sciences

of the

Heinrich-Heine-Universität Düsseldorf

submitted by

Nico Michael Potzkai

from Düsseldorf

Düsseldorf, 09.09.2026

aus dem Institut für Laser- und Plasmaphysik
der Heinrich-Heine-Universität Düsseldorf

PHASER

PHASE-STABILIZED HEINE LASER

Gedruckt mit der Genehmigung der
Mathematisch-Naturwissenschaftlichen Fakultät der
Heinrich-Heine-Universität Düsseldorf

Berichterstatter:

1. Prof. Dr. Georg Pretzler
   Institut für Laser- und Plasmaphysik
   Heinrich-Heine-Universität Düsseldorf

2. Prof. Dr. Götz Lehmann
   Institut für Theoretische Physik
   Heinrich-Heine-Universität Düsseldorf

Tag der mündlichen Prüfung: 05.11.2026

Abstract

Ultra-short laser-plasma interactions on solid-density targets evolving on femtosecond timescales remain largely inaccessible to conventional plasma diagnostics like spectroscopy, leaving pump-probe experiments as effectively the only viable approach. Overcritical plasma density renders a target optically opaque, preventing transmissive techniques and requiring a reflective approach. This work develops reflective phase imaging by Mach-Zehnder pump-probe interferometry, achieving 30 fs temporal, 15 µm spatial, and 0.1 rad phase resolution, which is sufficient to resolve the spatial expansion of overcritical plasma on timescales inaccessible to prior reflective techniques. To this end, a theoretical model for laser reflection on expanding plasma gradients was developed, moving beyond the standard critical-density-reflection assumption, which neglects the gradual density profile characteristic of a developing plasma.

The developed ray-tracing model shows that a laser ray curves through the plasma gradient, rather than traversing linearly and reflecting at a sharp interface as predicted by Fresnel theory. Diffraction simulations further reveal a previously undescribed effect. Finite numerical apertures compress phase and for large wavefront deformations, clip the measured phase, limiting the resolvable phase profile. Experimental data from glassy carbon, copper and gold-coated fused silica targets confirm the Multi-fs-simulated plasma size trends and display the predicted phase clipping and phase rings. This limits the reliable interpretation to early plasma times $t < 5$ ps due to available numerical aperture. This work establishes the gradient-ray-tracing correction as a universally applicable refinement, especially in late-stage plasma, and demonstrates that high numerical apertures are essential for reliable measurements beyond the earliest plasma stages, establishing clear design guidelines for future experiments.

Zusammenfassung

Ultrakurze Laser-Plasma-Wechselwirkungen auf Festkörper-Targets, die sich auf Femtosekunden-Zeitskalen entwickeln, bleiben für konventionelle Plasmadiagnostik wie Spektroskopie weitgehend unzugänglich, wodurch Pump-Probe-Experimente effektiv den einzigen vielversprechenden Ansatz darstellen. Überkritische Plasmadichte macht ein Target optisch undurchsichtig, wodurch transmissive Verfahren ausgeschlossen werden und ein reflektiver Ansatz erforderlich ist. Diese Arbeit entwickelt reflektive Phasenbildgebung mittels Mach-Zehnder Pump-Probe Interferometrie und erreicht dabei eine zeitliche Auflösung von 30 fs, eine räumliche Auflösung von 15 µm sowie eine Phasenauflösung von 0.1 rad, was ausreicht, um die räumliche Expansion überkritischen Plasmas auf Zeitskalen aufzulösen, die für bisherige reflektive Verfahren unzugänglich waren. Zu diesem Zweck wurde ein theoretisches Modell für die Laserreflexion an expandierenden Plasmagradienten entwickelt, das über die gängige Annahme der Reflexion an der kritischen Dichte hinausgeht, welche das graduelle Dichteprofil eines sich entwickelnden Plasmas vernachlässigt. Das entwickelte Ray-Tracing-Modell zeigt, dass ein Laserstrahl durch den Plasmagradienten gekrümmt wird, anstatt sich linear auszubreiten und an einer scharfen Grenzfläche gemäß der Fresnel-Theorie reflektiert zu werden. Beugungssimulationen zeigen desweiteren den bisher unbeschriebenen Effekt, dass eine endliche numerische Apertur die Phase komprimiert und bei großen Wellenfrontverformungen die gemessene Phase abschneidet, wodurch das auflösbare Phasenprofil begrenzt wird. Experimentelle Daten von Targets aus glasartigem Kohlenstoff, Kupfer, sowie mit Gold beschichtetem Quarzglas bestätigen die Trends der mit Multi-fs simulierten Plasmaexpansion und zeigen die vorhergesagte Phasenkompression sowie Phasenringe. Dies beschränkt die zuverlässige Interpretation auf frühe Plasmazeiten $t < 5$ ps. Diese Arbeit etabliert die Ray-Tracing-Korrektur des Plasmagradienten als universell anwendbare Verfeinerung, die besonders in späten Plasmastadien zum Tragen kommt, und zeigt, dass hohe numerische Aperturen für verlässliche Messungen jenseits der frühesten Plasmastadien essenziell sind, wodurch klare Designrichtlinien für zukünftige Experimente etabliert werden.

Contents

1 Introduction 1

2 Theoretical Basics 4
2.1 Laser Pulses . . . 4
2.1.1 Wave Propagation . . . 4
2.1.2 Gaussian Pulses . . . 5
2.1.3 Temporal Pulse Shape . . . 6
2.1.4 Spatial Energy Distribution . . . 8
2.1.5 Pulse Intensity . . . 9
2.1.6 Dispersion Coefficients . . . 10
2.1.7 Self-Focusing and Self-Phase Modulation . . . 12
2.2 Maxwell Equations . . . 14
2.3 The Drude-Model . . . 15
2.3.1 DC Model . . . 16
2.3.2 AC Model . . . 17
2.3.3 Thermal Conductivity . . . 19
2.4 Phase Effects Introduction . . . 20
2.5 Plasma . . . 22
2.5.1 Appleton-Hartree Equation . . . 23
2.6 Refractive Index Gradients . . . 25
2.7 Fresnel Description . . . 26
2.7.1 Electric Field Description . . . 27
2.7.2 Absorbing Media . . . 29
2.7.3 Lenses . . . 30
2.8 Goos-Hänchen-Shift . . . 32
2.8.1 Artmanns Description - Steady Phase . . . 33
2.8.2 Complex Shifts . . . 35
2.9 Phase Effects Summary . . . 36
2.10 Phase Images . . . 40
2.10.1 Algorithm . . . 40
2.10.2 Interference and Forking Fringes . . . 41

3 Experiment 46
3.1 Laser System . . . 46
3.2 Beam Profile . . . 48

3.3 Targets . . . 48
3.3.1 Fused Silica Target Coated with Gold . . . 48
3.3.2 Carbon Target . . . 50
3.3.3 Copper Target . . . 50
3.3.4 Surface Accuracy and Preparation . . . 51
3.4 Pump-Probe . . . 51
3.4.1 Interferometer Alignment . . . 53
3.4.2 Resolution . . . 55
3.4.3 Fringe-Direction Discussion . . . 56
3.4.4 Complications and Things to Consider . . . 57
3.5 Craters . . . 60

4 Simulation 64
4.1 Multi-fs . . . 64
4.2 Phase-Correct Ray Tracing Algorithm . . . 70
4.2.1 Ray and Surface Definitions . . . 70
4.2.2 Reflection Calculation . . . 70
4.2.3 Error Analysis . . . 71
4.2.4 Ray Tracing in Electron Density Distributions . . . 75
4.3 Combined Multi-fs and Ray Tracing . . . 86
4.4 Diffraction . . . 88
4.4.1 2D-Integrals . . . 89
4.4.2 Fresnel Number . . . 93
4.4.3 Sampling Considerations and Nyquist Limits . . . 93
4.4.4 2D Evaluation . . . 94
4.4.5 Reduction to Radial Symmetry . . . 95
4.4.6 Radial Diffraction Results . . . 96
4.5 Reconstruction of Phase Images / Summary Simulations . . . 100

5 Results 102
5.1 Plasma Phase Images . . . 102
5.2 Plasma Phase Development . . . 103
5.2.1 Relation to Reference Phase Shift . . . 105
5.2.2 Comparison with Simulation . . . 106
5.3 Phase Rings . . . 109
5.3.1 Time Frame . . . 110
5.3.2 Phase Rings by Diffraction . . . 110

6 Conclusion 113

A Phase Shift Due to Drude Model 127
A.1 Solid State . . . 127
A.1.1 Debye Temperature . . . 127
A.2 Phase Shifts by Electron Density and Collision Time Variation . . . 128
A.3 Phaserings Described by Drude Model . . . 129

B Pulse Contrast Measurement 132

C Carbon Crater Corona 133

D Correlation and Error Analysis of Phase Movements 134

E Multi-fs: Practical Configuration Notes 137

F Plasma Shape Fitting 138

G Electron Density Model for a Plasma Bubble 140

H Diffraction Integral Evaluation 142

I Analyzing Different Simulation Combinations 151

AI Disclosure 154

Danksagung 155

Declaration 156

Chapter 1

Introduction

Ultra-fast lasers have a wide range of use-cases, spanning industrial [1], medical [2], and fundamental physics research. While the term itself spans a wide range of what is considered to be "Ultra-Fast", ranging from nanosecond lasers down to attosecond pulses [3, 4]. The "sub-10-femtosecond" regime marks the transition to few-cycle pulses, where a single laser pulse contains only a handful of oscillations, enabling applications like strong-field ionization or attosecond pulse generation. This work utilizes those pulses for plasma diagnostics, where the pulses provide an incredibly fine temporal resolution for advanced plasma imaging techniques. Since solid-state laser-plasmas have many applications, such as material processing [5], fundamental physics research for examining extreme states of matter [6], analysis of wall materials in magnetic-confinement fusion reactors [7, 8], or damage-threshold studies [9], it is of general interest to describe the interaction between a laser and the solid, as well as the life cycle of the plasma, as accurately as possible.

While emission-based techniques repurposed for plasma diagnostics, such as laser induced breakdown spectroscopy [10] and laser induced ablation quadrupole mass spectroscopy [11], or dedicated mass and ion diagnostics, like time of flight mass spectroscopy [12] and Thomson parabola spectroscopy [13], can give quite reliable temperature, density, and/or composition readings, those techniques work at best on nanosecond scales. Rayleigh scattering [14] can also be used for broader density measurements at down to picosecond resolution.

Currently the only reliable techniques that reach femtosecond resolution are pump-probe experiments, where synchronized pump and probe pulses define the time resolution independent of detector speed. These include shadowgraphy [15, 16], absorption measurements [17, 18], reflection imaging [19, 20], phase-contrast imaging [21], and interferometric approaches producing either spectral images [22] or typical intensity images. However, capturing ultra-short laser-induced plasmas

on optically dense surfaces like metals [23] presents significant challenges. These methods struggle due to the similar reflectivity of both the plasma and the metal surfaces, making it difficult to discern plasma parameters from reflectivity alone, or are unable to resolve the earliest stages of plasma development since they cannot capture these ultra-fast dynamics.

In this work, the pump-probe approach will be used to create phase images with $\sim 15\,\mu m$ spatial, 30 fs temporal, and down to 0.1 rad phase resolution. Those plasma images make it possible to display the plasma's spatial evolution, while comparing them with hydro-fluid, plasma-gradient ray-tracing, and optical diffraction simulations.

Since plasma mirror research requires precise knowledge of plasma gradient parameters on solids [24–26], transmissive methods like shadowgraphy [27] or transmissive interferometry [28] are often not ideal due to the thickness and nature of the target. Frequency-domain interferometers solve those problems by having the advantage of high phase resolution since they can be used reflectively [22, 29–31], but are also highly dependent on low noise floors and scattered light from the pump pulse.

This work presents reflective spatial phase imaging as a solution by directly evaluating the optical path length within the plasma from the fringes, while also simplifying the underlying theoretical requirements since the phase deformation is measured directly. To this end, a full theoretical description of laser reflection imaged with a Mach-Zehnder interferometer is compared to the experimental data. Specifically, many rather unknown and often neglected effects of light reflection on metal are analyzed (chapter 2). Since the effects of the plasma have to be compared to a known quantity, metals are used as a reference (sections 2.3 and 2.4). To correctly describe these reflection effects on metals, the phase shifts upon reflection and the resulting Goos-Hänchen (GH) [32] and Imbert–Fedorov (IF) [33] shifts are presented (section 2.8).

Since reflection on plasma is mainly discussed theoretically for either plasma mirror applications for High Harmonic Generation (HHG) [34] or steep plasma gradients, where surface-like properties and direct reflection at the critical density can be assumed [35], this work develops a model for plasma reflection on expanding plasma gradients. To evaluate this model under realistic conditions, the plasma parameters are simulated using the Multi-fs [36] hydrodynamic plasma code (section 4.1). There, plasma is ignited similar to the experiment by an ultra-short-pulse laser with a few-cycle FWHM $< 8\,fs$ and a high intensity $I > 4 \times 10^{17}\,Wcm^{-2}$.

To evaluate the effect of an expanded plasma, a ray-tracing algorithm is presented, showcasing the behavior of a ray passing through an electron density gra-

dient (section 4.2.4). The relevant refractive index distribution in the plasma and their subsequent effect on the ray are determined from the Multi-fs parameters in combination with FLYCHK [37]. With those results, the effects of plasma reflection are compared to metal reflection, showcasing similarities and deviations in the behavior. This is used to create a simplified model allowing evaluation of the scale at which the phase shifts and GH-like shifts occur in relevant plasma (section 4.3).

In addition, the full Mach-Zehnder setup is simulated and evaluated. To this end, the imaging properties of the optical system are analyzed, especially focusing on the effects of imaging defects on phase images (section 4.4). While standard diffraction theory has many predictions and concepts about aberrations in the intensity profile, the literature provides no general concepts on the expected phase aberrations. Thus, a simplified description for the given plasma shape is presented, allowing interpretation of the effects of the numerical aperture (NA) on deformed wavefronts.

Finally, various crucial setup subtleties and evaluation details are explained here (section 3.4), displaying the accuracy of the system, while also showing important caveats which may produce wrong images, without an obvious cause. Here, on one hand, setup mistakes that previous experiments may not have considered are presented. While they are inconspicuous individually, they can create contradictory results between measurements without a clear reason (section 3.4.4). On the other hand, evaluation limitations are discussed, showing the range of plasma conditions and the relevant parameters that can be clearly evaluated using this process (section 4.5).

The experimental phase images are finally compared with a whole simulation of the system, plasma development, light propagation, and diffraction (chapter 5). This demonstrates the effectiveness of the presented experimental setup and identifies its most important physical parameters, as well as the unique regime in which it can provide exceptional experimental data.

Chapter 2

Theoretical Basics

The following chapter covers the theoretical fundamentals of high-energy ultra-short laser pulses and their interaction with matter, as well as the motion of electrons in metals and gases. Subsequently, the side effects of these combinations and measurement techniques for visualizing and analyzing these effects are explained in more detail.

2.1 Laser Pulses

A high-intensity titanium-sapphire (Ti:Sa) solid-state-laser is used in the experiment which is pumped by a frequency-doubled neodymium-doped yttrium aluminum garnet (ND:YAG) laser. The Ti:Sa laser radiates in an infrared to red spectrum, while being compressed to a pulse duration of less than 10 fs. This process is elucidated theoretically in the following.

2.1.1 Wave Propagation

Electromagnetic waves consist of coupled electric and magnetic fields. These are described according to Maxwell's equations section 2.2 by the wave equation

$$\left(\nabla^2 - \frac{1}{c^2}\frac{\partial^2}{\partial t^2}\right)\vec{E}(\vec{r},t) = \frac{1}{\varepsilon_0 c^2}\frac{\partial^2}{\partial t^2}\vec{P} \tag{2.1}$$

in vacuum. Here $\vec{E}(\vec{r},t)$ describes the direction of the electric field, c the speed of light, ϵ_0 the permittivity of free space, and $\vec{P}$ the polarization.

In homogeneous mediums without transitions to other media, it is solved by

$$\vec{E}(\vec{r},t) = \vec{E}_0(x,y,t) \cdot \exp\left[-i\left(t\cdot\omega - z\cdot k + \phi\right)\right] \tag{2.2}$$

with the amplitude of the electric field $\vec{E}_0(x, y, t)$ spanning in the x-y-plane, the angular frequency ω, the wavenumber k, the direction of propagation z and the phase at the origin ϕ. For this work the complex definition is more convenient than the "real" description

$$\vec{E}(\vec{r}, t) = \vec{E}_0(x, y, t) \cdot \sin(t \cdot \omega - z \cdot k + \phi)$$

wherefore for all future formulations, where it is not explicitly stated, a complex expression shall be assumed. A single photon possesses the energy

$$E = h\nu = \frac{hc}{\lambda} \tag{2.3}$$

with the Plank constant h and the wavelength of the photon λ as postulated by Einstein. If the photon interacts with some kind of medium, the refraction index

$$n = n_0 + i\beta \tag{2.4}$$

gives information about direction of propagation and absorption. In this case n_0 is the real part of the refraction index, while β is the imaginary part, also known as the extinction coefficient. Its derivation will be shown in section 2.3. When moving through a medium the wave number becomes $k = \frac{2\pi}{\lambda} \cdot n$. This leads to a new solution of the wave function eq. (2.2)

$$\vec{E}(\vec{r}, t) = \vec{E}_0(x, y, t) \cdot \exp\left[-z \cdot \beta \cdot \frac{2\pi}{\lambda} - i\left(t \cdot \omega - z \cdot \frac{2\pi}{\lambda} \cdot n_0 + \phi\right)\right] \tag{2.5}$$

which becomes more clear in the real expression

$$\vec{E}(\vec{r}, t) = \vec{E}_0(x, y, t) \cdot \exp\left(-z \cdot \beta \cdot \frac{2\pi}{\lambda}\right) \cdot \sin\left(t \cdot \omega - z \cdot \frac{2\pi}{\lambda} \cdot n_0 + \phi\right)$$

where the extinction coefficient of the medium decreases the electric field exponentially while the real part of the refractive index changes the speed of the wave, leading to the refraction.

2.1.2 Gaussian Pulses

The most important aspect of lasers is the coherence of the emitted light. To adequately describe the behavior of a laser pulse, it is advantageous to separate between the temporal and spatial aspects. The following sections will be heavily

dependent on variations of Gaussian profiles, wherefore it shall be first shortly introduced here as

$$A(x) = A_0 \cdot \exp\left[-\frac{1}{2}\left(\frac{x - x_0}{\xi}\right)^2\right] \tag{2.6}$$

with the amplitude A_0, mean x_0, and the Gaussian width ξ. An alternative form to express the Gaussian width is the full width at half maximum (FWHM)

$$\Delta x = 2\sqrt{2\ln(2)} \cdot \xi. \tag{2.7}$$

which is also visualized in fig. 2.2 a). The names of the variables will change given by the context of the upcoming equations.

2.1.3 Temporal Pulse Shape

This section now describes only the temporal properties, while eliminating the spatial component of the wave.

In the experimental setup the envelope $E_0(t)$ travels in time as a Gaussian wave packet

$$E_0(t) = E_{\max} \cdot \exp\left[-\frac{1}{2}\left(\frac{t}{\xi_t}\right)^2\right] \tag{2.8}$$

with the Gaussian width ξ_t and the amplitude $E_{\max}$ (see fig. 2.1). Since real world devices usually measure the intensity

$$I = \frac{1}{2} c \varepsilon E_0^2 \tag{2.9}$$

of the pulse the FWHM is defined in the intensity domain, not the electric field domain, as

$$\Delta\tau = 2\sqrt{2\ln(2)} \cdot \xi_t. \tag{2.10}$$

can be determined. A Fourier transformation yields the spectrum of said pulse

$$E_0(\omega) = E_{\max} \cdot \frac{\xi_t}{\sqrt{2}} \cdot \exp\left[-\frac{1}{2}\left(\omega\xi_t\right)^2\right]. \tag{2.11}$$

where it is apparent, that a Gaussian width in ω-space

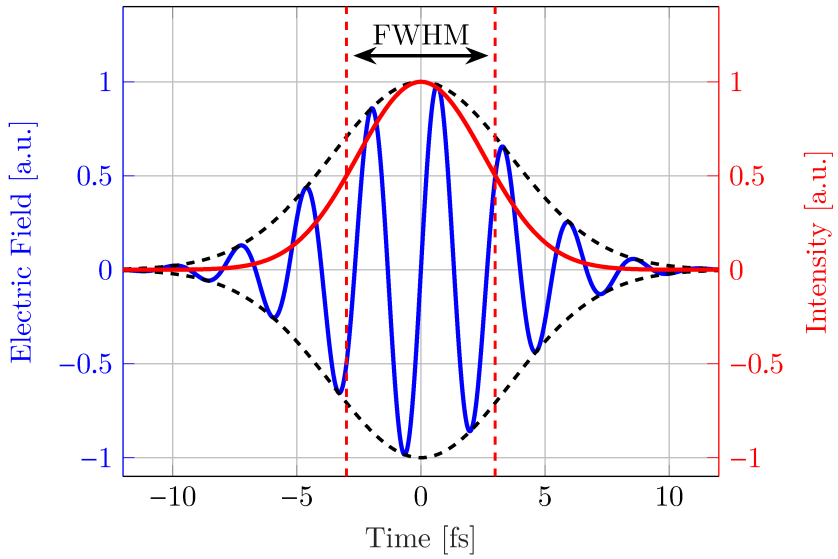


Figure 2.1: Oscillation of the electric field within the Gaussian envelope. The blue graph represents the oscillation of the electric field. It is enveloped by the black dotted curve following the Gaussian (see fig. 2.2 a), eq. (2.8)). The red curve represents the corresponding intensity distribution $I \sim E^2$, which has the marked FWHM [38].

$$\xi_\omega = \frac{1}{2\xi_t} \tag{2.12}$$

is required to describe the pulse equally (2.8) in a Gaussian manner. This gives the spectral width

$$\Delta\omega = 2\sqrt{2\ln(2)} \cdot \xi_\omega \tag{2.13}$$

which then implies the Fourier-limit, which follows from both of those widths

$$\Delta\tau\Delta\omega \geq 4\ln 2. \tag{2.14}$$

for the shortest possible duration of a pulse. [1]

[1] Simply combining (2.10) and (2.13) would yield an equal sign for (2.14), which would actually be incorrect. Technically, the spatial width is complex in nature, containing imaginary parts with information about the phase difference of the different colors. Therefore, the real parts yield only the given inequality.

2.1.4 Spatial Energy Distribution

Just like the temporal distribution, the spatial energy distribution of the laser pulse used can also be approximated by a Gaussian curve (see fig. 2.2 a)). In the later described experiment, the pulse shows radial symmetry and has the same FWHM in both dimensions of the wavefront. Due to the $I \sim E^2$ (eq. (2.9)) dependence E is measured indirectly via the intensity. Therefore, the E-field amplitude

$$E(x) = E_0 \cdot \exp\left(-\frac{1}{2}\left(\frac{x - x_0}{\xi_E}\right)^2\right) \tag{2.15}$$

can be described similarly by a Gaussian, with the gaussian width ξ_E around the center x_0. The FWHM of the electric field E and the intensity I can be calculated using ξ_E with

$$\Delta x_E = 2\sqrt{2\ln 2} \cdot \xi_E \text{ and } \Delta x_I = \sqrt{2\ln 2} \cdot \xi_E \tag{2.16}$$

When a beam is focused, the spatial width changes depending on the position z. The minimal achievable beam width at the focus $w_0(z = 0)$ (see fig. 2.2) follows from the focusing optics and can be calculated using the focal length f, the wavelength λ_0 and the initial Gaussian width of the incoming beam ξ_E. The area with the diameter of

$$w_0 \geq \frac{1}{\pi} \cdot \frac{\lambda_0 f}{\xi_E} \tag{2.17}$$

contains 86,5% of the energy of the beam. 99,9% of the energy is contained inside $2w_0$. The Rayleigh length

$$z_R = \frac{\pi w_0^2}{\lambda}. \tag{2.18}$$

specifies the distance at which the beamwidth rises to $w(z_R) = \sqrt{2}w_0$ and therefore the beam cross section doubles. The parameter $b = 2z_R$ from $-z_R < z < z_R$ is considered as the length of the focus. At a distance z away from the focus, the beam width can be calculated according to

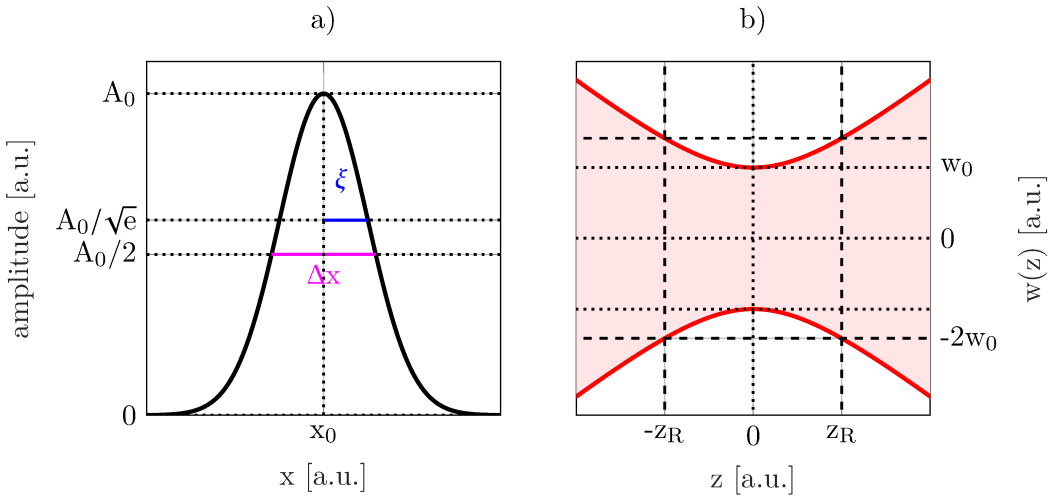


Figure 2.2: a) Gaussian curve according to (2.6) with amplitude A_0, FWHM Δx, Gaussian width ξ and mean x_0. b) Envelope of a focused Gaussian pulse. The beam waist w_0, the confocal parameter b, the aperture angle Θ and the radius of the wave fronts $R(z)$. [40]

$$w(z) = w_0 \sqrt{1 + \left(\frac{\lambda z}{\pi w_0^2}\right)^2} \tag{2.19}$$

where $w(z = 0) = w_0$. For long distances $z \gg z_R$ the width $w(z)$ increases almost linearly, so the apex angle $\Theta/2$ towards the z-axis with the origin at $z(w_0)$ can be calculated. The divergence angle

$$\Theta_{\text{div}} = \Theta/2 = \lim_{z \gg z_r} \frac{w(z)}{z} = \frac{\lambda}{\pi w_0} \tag{2.20}$$

is used to define the beam quality factor M^2, with $\Theta_{\text{div}} w_0 = M^2 \frac{\lambda}{\pi}$. In an experimental environment the beam profile varies depending on high transversal modes, amplitude disruptions and phase disruptions. Therefore, the focus w_0 for true Gaussian profiles becomes larger and/or the divergence angle Θ_{div} increases by M^2. In the case of a Gaussian pulse (TEM_{00}), $M^2 = 1$ [39].

2.1.5 Pulse Intensity

The intensity a single pulse can deploy depends on the pulse length $\Delta\tau = \xi_t \sqrt{2 \ln 2}$ (FWHM see fig. 2.1).The intensity distribution in time and space can be described

by a radial distribution with

$$I(r,t) = I_0 \cdot \exp\left\{-2\left[\left(\frac{r}{w(z)}\right)^2 + \left(\frac{t-t_0}{\xi_t}\right)^2\right]\right\} \tag{2.21}$$

of which the amplitude of the intensity is

$$I_0 = \sqrt{\frac{8}{\pi^3}} \cdot \frac{E_{\text{pulse}}}{w(z)^2 \xi_t} = 4 \cdot \sqrt{\frac{\ln 2}{\pi^3}} \cdot \frac{E_{\text{pulse}}}{w(z)^2 \Delta\tau}. \tag{2.22}$$

with the total pulse energy E_{pulse} (2.24). In experimental physics the average temporal intensity within $1/e^2$ of the Gaussian width is often more suitable to use, which is described by

$$I_e = 0.259 \cdot I_0. \tag{2.23}$$

The total energy of the pulse is

$$E_{\text{pulse}} = \sqrt{\left(\frac{\pi}{2}\right)^3} \cdot \xi_t \cdot \omega^2 \cdot I_0 = \int_{-\infty}^{\infty} P_{\text{pulse}}(t)\mathrm{d}t \tag{2.24}$$

which follows from integrating over the power of the pulse

$$P_{\text{pulse}}(t) = \frac{\pi}{2} w^2 \cdot I_z(t) = \int_0^{\infty} 2\pi r \cdot I_z(t) \exp\left[-2\left(\frac{r}{\omega}\right)^2\right] \mathrm{d}r. \tag{2.25}$$

$I_z(t)$ is the temporal part of $I(r,t)$ (eq. (2.22)) along the direction of propagation.

2.1.6 Dispersion Coefficients

When a wave travels through matter, it is inevitable that the pulse shape will change in the time domain due to the frequency dependence of the refraction index n of the material. Therefore, the speed of light varies frequency dependent, which changes the spectral phase, i.e., the relative position of the waves of different colors. The mathematical description results from the Taylor expansion of the spectral phase

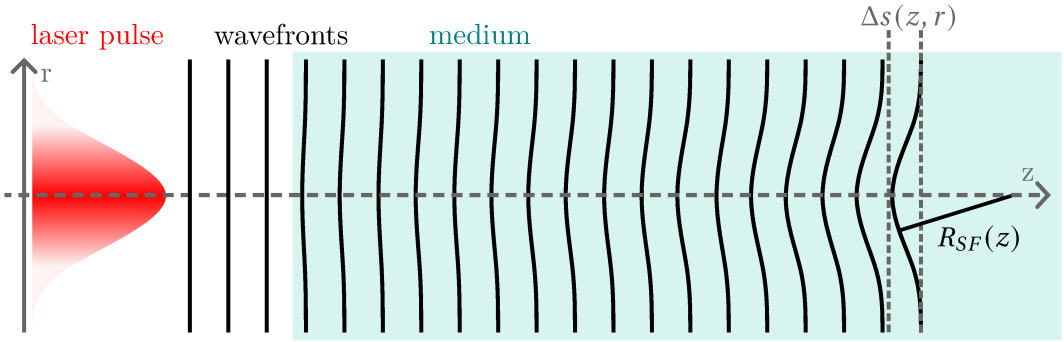


Figure 2.3: Wavefronts propagating in z direction through a medium. The mediums refractive index changes locally due to the intensity distribution of the pulse. This leads to a distortion of the wavefront with the corresponding radius R_{SF}. [40]

$$\phi(\omega) = \sum_{i=0}^{\infty} \frac{(\omega - \omega_0)^i}{i!} \cdot \left[\frac{\partial^i}{\partial \omega^i} \phi(\omega) \right]_{\omega=\omega_0} \tag{2.26}$$

from which one can obtain the dispersion coefficients

$$D_i = \left[\frac{\partial^i}{\partial \omega^i} \phi(\omega) \right]_{\omega=\omega_0} = x \cdot \left[\frac{\partial^i k}{\partial \omega^i} \right]_{\omega=\omega_0} = \frac{x}{c} \cdot \left[\frac{\partial^i}{\partial \omega^i} (\omega \cdot n(\omega)) \right]_{\omega=\omega_0} \tag{2.27}$$

as described in [40]. D_0 defines the carrier envelope phase of the wave, D_1 shifts the pulse in time (the envelope of the pulse). D_2 corresponds to the broadening of the pulse while moving through matter. D_3 and higher order terms describe asymmetric deformations like pre- and post-pulses. The different coefficients can be calculated by measuring the spectral phase and taking its respective derivatives for different materials. For example, both air and glass have a positive D_2 where one millimeter of propagation through glass corresponds to approximately one meter of propagation through air. In the later described experiment, the measurement of the laser properties happens at a different location than the experiment. Therefore after analyzing the pulse shape, glass plates are placed in the path, to compensate for the difference of travel through matter and the corresponding change of the dispersion.

2.1.7 Self-Focusing and Self-Phase Modulation

Self-phase modulation and self-focusing (SF) are non-linear effects of light-matter interaction. Both occur due to the fact that at high intensities the real part of the refractive index (n_0, from eq. (2.57)) of a medium changes depending on the intensity

$$\Re(n) = n_0 + \Delta n(I) = n_0 + n_2 \cdot I + \dots . \tag{2.28}$$

Self-focusing is a spatial effect. Therefore, the radial (r) phase dependency of the wave

$$\Delta\phi(r) = z \cdot \frac{\omega}{c} \cdot n_2 \cdot I(r) \tag{2.29}$$

in the direction of propagation z depends on the radial intensity of the pulse $I(r) = I_0 \cdot e^{-2\left(\frac{r}{w}\right)^2}$. From this follows a radial deformation of the wavefront which is described by

$$\Delta s(z, r) = z \cdot \left(1 + \frac{n_2}{n_0} \cdot I(r)\right)^{-1} \approx z \cdot \left(1 - \frac{n_2}{n_0} \cdot I(r)\right). \tag{2.30}$$

In fig. 2.3 the local change in the direction of propagation can be seen. The new wavefront can be assigned to the radius

$$R_{\mathrm{SF}}(z) \approx \frac{n_0}{n_2} \cdot \frac{w^2}{4zI_0}. \tag{2.31}$$

For small z the diffraction radius is

$$R_{\mathrm{SF,small}}(z) \approx z \cdot \left(\frac{\pi w_0^2}{(\lambda_0/n_0)z}\right)^2. \tag{2.32}$$

If $R_{\mathrm{SF}} \leq R_{\mathrm{SF,small}}$ then if the power

$$P \approx \frac{I_0}{2\pi w_0^2} \geq P_{\mathrm{crit}} = \frac{\alpha \cdot \lambda^2}{8\pi n_0 n_2} \tag{2.33}$$

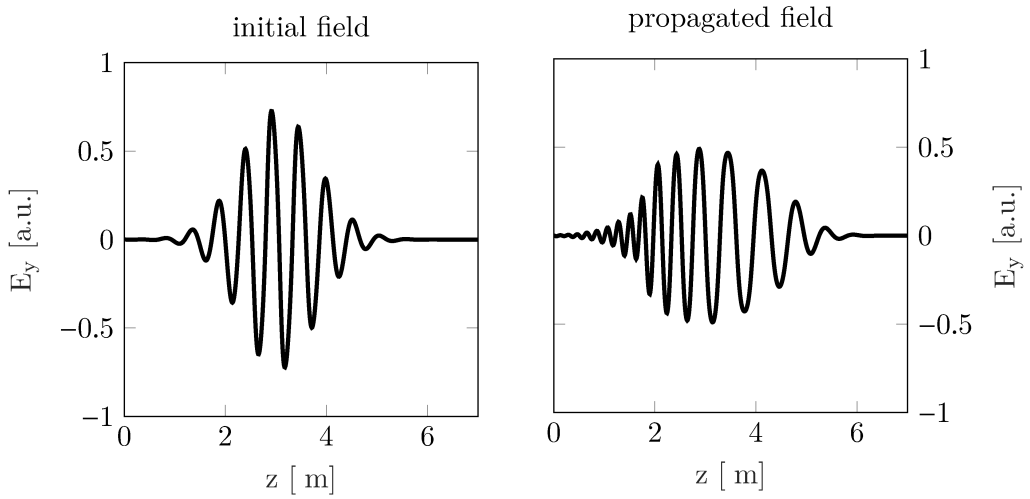


Figure 2.4: The phases at the center of the wave, where the intensity is highest, are slowed due to the increasing refractive index of the medium. [40]

exceeds the critical power P_{crit} (α is empirical) self-focusing will occur inside the medium, which may ignite plasma. Therefore, particular caution has to be given.

Self-phase modulation on the other hand is a temporal effect. Due to the fact that the temporal intensity of the pulse follows a gaussian profile (fig. 2.1)

$$I(t) = I_0 \cdot e^{-2\left(\frac{t}{xi_t}\right)^2} \tag{2.34}$$

the rise in intensity with time heightens the refractive index for the intense part of the pulse. This leads to a phase shift

$$\Delta\phi(t) = z \cdot \frac{\omega}{c} \cdot n_2 \cdot I(t) \tag{2.35}$$

which stretches the early part of the pulse and tightens the back (fig. 2.4). The deformation of the pulse lets new frequencies occur and changes the spectral envelope $\widetilde{E}(\omega)$ and thus the temporal envelope $\widetilde{E}(t)$.

2.2 Maxwell Equations

There are different ways to write the Maxwell equations which will later be referenced in the Drude model section 2.3. Therefore, they are gathered here together. Often the differential form of the Maxwell Equations are used

$$\vec{\nabla} \cdot \vec{E} = \frac{\rho}{\varepsilon_0}, \tag{2.36}$$

$$\vec{\nabla} \cdot \vec{B} = 0, \tag{2.37}$$

$$\vec{\nabla} \times \vec{E} = -\frac{\partial \vec{B}}{\partial t}, \tag{2.38}$$

$$\vec{\nabla} \times \vec{B} = \mu_0 \vec{j} + \mu_0 \varepsilon_0 \frac{\partial \vec{E}}{\partial t}, \tag{2.39}$$

where $\vec{E}$ is the electric field, $\vec{B}$ the magnetic field, ρ the electric charge density, $\vec{j}$ the electric current density, ε_0 the vacuum permittivity, and μ_0 the vacuum permeability.

Sometimes he equations expressed in the Lorenz gauge can be more useful. In the homogeneous case they are:

$$\vec{B} = \vec{\nabla} \times \vec{A} \tag{2.40}$$

$$\vec{E} = -\vec{\nabla}\varphi - \frac{\partial \vec{A}}{\partial t} \tag{2.41}$$

$$\vec{\nabla} \cdot \vec{A} = -\frac{1}{c^2} \frac{\partial \varphi}{\partial t} \tag{2.42}$$

where $\vec{A}$ is the magnetic vector potential and φ the electric scalar potential, and c is the speed of light in vacuum. These potentials are introduced because $\vec{B}$ is always divergence-free, which allows it to be written as the curl of a vector field, $\vec{B} = \vec{\nabla} \times \vec{A}$. Using this in the Maxwell-Faraday equation (2.38) shows that $\vec{E} + \partial \vec{A}/\partial t$ is curl-free, so it can be written as the gradient of a scalar potential φ, giving the expression for $\vec{E}$ above. Since $\vec{A}$ and φ are not uniquely determined by $\vec{E}$ and $\vec{B}$ alone, an additional constraint is imposed to fix them and to decouple the resulting equations for φ and $\vec{A}$.

The inhomogeneous case is:

$$\left(-\nabla^2 + \frac{1}{c^2}\frac{\partial^2}{\partial t^2}\right)\varphi = \frac{\rho}{\varepsilon_0} \tag{2.43}$$

$$\left(-\nabla^2 + \frac{1}{c^2}\frac{\partial^2}{\partial t^2}\right)\vec{A} = \mu_0\vec{j} \tag{2.44}$$

where ∇^2 denotes the Laplace operator, applied here to the potentials φ and $\vec{A}$. The Laplace operator is defined as the divergence of the gradient, $\nabla^2 f = \vec{\nabla}\cdot(\vec{\nabla}f)$, which in Cartesian coordinates corresponds to the sum of second partial derivatives with respect to each spatial coordinate, $\nabla^2 f = \partial^2 f/\partial x^2 + \partial^2 f/\partial y^2 + \partial^2 f/\partial z^2$. For this to hold, Lorenz invariance

$$\vec{\nabla}\cdot\vec{A} + \frac{1}{c^2}\frac{\partial\varphi}{\partial t} = 0 \tag{2.45}$$

has to be fulfilled.

The solutions for the potential and vectorfield are:

$$\varphi(\vec{r},t) = \frac{1}{4\pi\varepsilon_0}\int\frac{\rho}{R}dV \tag{2.46}$$

$$\vec{A}(\vec{r},t) = \frac{\mu_0}{4\pi}\int\frac{\vec{j}}{R}dV \tag{2.47}$$

where $\vec{r}$ is the observation point, $R = |\vec{r} - \vec{r}\,'|$ the distance between the source point $\vec{r}\,'$ and the observation point, and the integration is carried out over the source volume V.

2.3 The Drude-Model

To correctly describe reflection on metals and plasma in section 2.7, it is first necessary to understand how free electrons respond to an electromagnetic wave and how they are connected to the refractive index eq. (2.4). The Drude model provides a simple yet reliable description of this behavior, treating the conduction electrons as a free electron gas subject to collisions, and yields accurate predictions for the optical response of metals and plasmas under well-defined assumptions. In particular, it allows additionally to observe the effects of temperature and collision frequency on the refractive index (see appendix A). This chapter follows [41], with adaptations for the specific application of this work.

The following basic assumptions are made: metallic conductivity is treated

within kinetic gas theory, i.e., the metal is modeled as an electron gas. Since metals are overall neutral, a two-component description is required, introducing ions that compensate the electron charge. These ions are assumed immobile, either because they are much heavier than the electrons (as in a plasma) or because they are bound within the lattice (as in a metal).

The rigorous treatment of electron and ion behavior is given by the quantum theory of solids. Here, however, the conduction-band electrons are simplified to a freely moving electron gas.

Each atomic species a has nuclear charge $q_i = eZ_a$, where Z_a is the atomic number, surrounded by electrons of total charge $q_e = -eZ_a$. Of these, Z electrons per atom are assumed free, while the remaining $Z_c = Z_a - Z$ are called core electrons[2] and are treated as fixed in space. The electron gas therefore has number density $n = Z\rho/m_i$, with mass density ρ and ion mass m_i.

2.3.1 DC Model

To describe the concept of conductivity through an electron gas, a few adjustments are necessary. First, there is Ohm's law

$$\vec{E} = \rho\vec{j}, \tag{2.48}$$

describing electrical direct current conductivity. Here, the current must be proportional to the electric field with the resistivity ρ.

This requires the electric current $\vec{j} = -ne\vec{v}_{\text{avg}}$. The average electron velocity v_{avg} is calculated from the force of the electric field $\vec{F} = -e\vec{E}$ and the average time between collisions τ. Assuming that the electron velocity is randomly distributed after each collision, we obtain

$$\vec{v}_{\text{avg}} = -e\vec{E}\frac{\tau}{m} \tag{2.49}$$

and therefore the current is $\vec{j} = \frac{ne^2\tau}{m} \cdot \vec{E}$. For consistency purposes, the conductivity $\sigma = 1/\rho$ is also defined with

$$\sigma = \frac{ne^2\tau}{m}. \tag{2.50}$$

Now the conductivity has to be estimated by known quantities. τ is unknown and cannot be easily approximated. If the electrons velocity $\vec{v}_e(t) = \vec{p}_e(t)/m_e$ is represented by the momentum the current density breaks down to

[2] Formally $Z_a = Z_c + Z_{\text{valence}}$, with only a fraction of the valence electrons contributing to conduction. Here all "bound" valence electrons are grouped with the core electrons for simplicity.

$$\vec{j}(t) = -\frac{ne\vec{p}(t)}{m} \tag{2.51}$$

with the mass m of all free electrons and their overall momentum $\vec{p}(t)$. After the time step $\mathrm{d}t$ the momentum $\vec{p}(t+\mathrm{d}t)$ has the probability $\mathrm{d}t/\tau$ to change due to a collision. Non-colliding particles experience the force $\vec{F}$ of the electric field, as previously stated. Therefore, the average momentum after $\mathrm{d}t$ equals the probability of not colliding particles $1-\mathrm{d}t/\tau$ times their new momentum $\vec{p}(t)+\vec{F}(t)\mathrm{d}t$. This breaks down to

$$\vec{p}(t+\mathrm{d}t) = \left(1-\frac{\mathrm{d}t}{\tau}\right)\left(\vec{p}(t)+\vec{F}(t)\mathrm{d}t\right)$$

which can be simplified to $\vec{p}(t+\mathrm{d}t) = \vec{p}(t) + \left(\vec{F}(t) - \frac{\vec{p}(t)}{\tau}\right)\mathrm{d}t + O(\mathrm{d}t^2)$. Neglecting the $\mathrm{d}t^2$ terms one comes to $\vec{p}(t+\mathrm{d}t) - \vec{p}(t) = \left(\vec{F}(t) - \frac{\vec{p}(t)}{\tau}\right)\mathrm{d}t$ which leads to the derivative

$$\frac{\mathrm{d}\vec{p}}{\mathrm{d}t} = \vec{F}(t) - \frac{\vec{p}(t)}{\tau}. \tag{2.52}$$

Now it is seen, that an exponential damping term in the form of $\vec{p}(t) = \vec{F}(t)\cdot\left(\tau + c_1 e^{-t/\tau}\right)$ or $\vec{p}(t) = \vec{p}_0\cdot\left(1+c_2 e^{-t/\tau}\right)$ is needed with $c_1 < 0$, which is equivalent to Ohms law.

2.3.2 AC Model

For AC conductivity an electric oscillating field $\vec{E}(t) = \vec{E}_0 e^{-i\omega t}$ and an oscillating velocity of the electrons $\vec{p}(t) = \vec{p}_0 e^{-i\omega t}$ are assumed. With $F = -e\vec{E}(t)$ the solution for the equation of motion eq. (2.52) becomes of the form

$$-i\omega\vec{p}_0 = -e\vec{E}_0 - \frac{\vec{p}_0}{\tau}.$$

From which follows $\vec{p}_0 = \frac{-e\vec{E}_0}{1/\tau - i\omega}$. Under consideration of eq. (2.51) the current becomes

$$\vec{j}_0 = \frac{ne^2\vec{E}_0}{m\left(\frac{1}{\tau} - i\omega\right)}.$$

Now the conductivity $\sigma = \vec{j}_0/\vec{E}_0$ can be written as

$$\sigma(\omega) = \frac{ne^2\tau}{m\left(1-i\omega\tau\right)} = \frac{\sigma_0}{1-i\omega\tau}$$

where one can see that the conductivity depends on the frequency, which is indeed

the case. This formula is only valid if the wavelength is much larger than the free path length of the electrons, because a spatially uniform electric field was assumed, which only changes in time. If the electron collides faster than the electric field changes spatially, it always sees a uniform field. With wavelengths of above 100 nm (true for visible light) this always holds true.

From this the relative permittivity $\varepsilon_r(\omega)$ can be calculated by transforming the Maxwell equations. On one hand $\vec{\nabla} \times (\vec{\nabla} \times \vec{E}) = \vec{\nabla}(\vec{\nabla}\vec{E}) = -\vec{\nabla}^2\vec{E}$ where eq. (2.38) can be implemented for $\vec{\nabla} \times (\vec{\nabla} \times \vec{E}) = \vec{\nabla} \times \left(-\frac{\partial \vec{B}}{\partial t}\right)$ to obtain

$$-\vec{\nabla}^2\vec{E} = \vec{\nabla} \times \left(-\frac{\partial \vec{B}}{\partial t}\right).$$

Still the dominant electric and magnetic fields come from the electromagnetic wave and therefore have the form of $\vec{B}(t) = \vec{B}_0 e^{-i\omega t}$ to get $-\vec{\nabla}^2\vec{E} = i\omega \cdot \vec{\nabla} \times \vec{B}$.

With Maxwell's eq. (2.39)

$$-\vec{\nabla}^2\vec{E} = i\omega \left(\mu_0 \vec{j} + \mu_0 \varepsilon_0 \frac{\partial \vec{E}}{\partial t}\right)$$

the magnetic field can be eliminated. Again $\vec{E}(t) = \vec{E}_0 e^{-i\omega t}$ is oscillating in time, so $-\vec{\nabla}^2\vec{E} = i\omega(\mu_0\sigma(\omega) - i\mu_0\varepsilon_0\omega)\vec{E}$. Which can be written more elegant as

$$-\vec{\nabla}^2\vec{E} = \mu_0\varepsilon_0\omega^2\vec{E}\left(1 + \frac{i\sigma(\omega)}{\varepsilon_0\omega}\right) = \frac{\omega^2}{c^2}\varepsilon_r(\omega)\vec{E}$$

with $\varepsilon_r(\omega) = 1 + \frac{ine^2\tau}{\varepsilon_0 m\omega(1-i\omega\tau)}$ so that

$$\varepsilon_r(\omega) = 1 - \frac{\omega_p^2}{\omega^2 + i\frac{\omega}{\tau}} \tag{2.53}$$

with the plasma frequency

$$\omega_p^2 = \frac{ne^2}{\varepsilon_0 m_e}. \tag{2.54}$$

In the case of $\tau\omega \gg 1$ (if $\omega^2 \gg \omega/\tau$ or $\tau \gg \omega$) one can write $\varepsilon_r(\omega) = 1 - \frac{\omega_p^2}{\omega^2}$. If $\tau\omega$ are not much grater than one, $\varepsilon_r(\omega) = \varepsilon_1 + i\varepsilon_2$ with

$$\varepsilon_1(\omega) = 1 - \frac{\omega_p^2}{\omega^2 + \frac{1}{\tau}} \tag{2.55}$$

$$\varepsilon_2(\omega) = \frac{\omega_p^2}{\tau\omega\left(\omega^2 + \frac{1}{\tau^2}\right)} \tag{2.56}$$

which gives the absorption and reflectivity of a metal or plasma. The plasma oscillations of the electron gas follow from the equation of continuity $\vec{\nabla} \cdot \vec{j} = -\frac{\partial \vec{\rho}}{\partial t}$ on the left hand side and Gauss law $\vec{\nabla} \cdot \vec{E} = \frac{\rho}{\varepsilon_0}$ on the right hand side. Assuming oscillatory behavior for $\rho(t) = \rho_0 e^{-i\omega t}$ follows from the equation of continuity $\vec{\nabla} \cdot \vec{j} = i\omega\rho(\omega)$ and using $\vec{E} = \frac{\vec{j}}{\sigma}$ one gets from Gauss law $\frac{\vec{\nabla} \cdot \vec{j}}{\sigma} = \frac{\rho}{\varepsilon_0}$. Putting this together one gets $i\omega\rho(\omega) = \frac{\sigma\rho(\omega)}{\epsilon_0}$ which is only true if

$$1 + \frac{i\sigma(\omega)}{\epsilon_0\omega} = 0$$

which is the condition for wave propagation in plasma.

Additionally this theory allows to express the index of refraction as a property of the electron density by using

$$n = n_0 + i\beta = \sqrt{\varepsilon_r} \tag{2.57}$$

which can be decomposed into

$$n_0 = \sqrt{\frac{|\varepsilon_r| + \varepsilon_1}{2}} \tag{2.58}$$

$$\beta = \sqrt{\frac{|\varepsilon_r| - \varepsilon_1}{2}}. \tag{2.59}$$

This property will later be used to analyze electron density waves in metals.

2.3.3 Thermal Conductivity

It is assumed that for metals the thermal conductivity is mainly driven by the free electron gas. Thermal conduction by ions is neglected in this model. If an temperature T gradient is present the heat flux $\vec{q}$ can be described with the the thermal conductivity κ by

$$\vec{q} = -\kappa\vec{\nabla}T. \tag{2.60}$$

which is called Fouriers law. Lets assume a 1D case where a metal rod is split in two regions, one with low temperature T_1 and one with high temperature T_2. Let the middle position between the two temperatures be x, where half the electrons have T_1 and the other half have T_2. If an electron comes from the side with T_1, they had their last collision in the T_1 side at the position $x_1 = x - v_{x1}\tau$. The electron coming from the right side had their last collision at position $x_2 = x - v_{x2}\tau$. Therefore, the average energy of a single (!) electron at position x is $\epsilon(x) = \epsilon(T(x_1))/2 + \epsilon(T(x_2))/2$. The heat flux is thereby

$$q_x = \frac{n v_x}{2} \left[\epsilon(T(x - v_x\tau)) - \epsilon(T(x + v_x\tau))\right]$$

because $v_{x1} \approx -v_{x2}$ since v_2 comes from the opposite side. If $v_x\tau \to 0$, this can be written as a differential form

$$q = -n\tau v^2 \frac{\mathrm{d}\epsilon}{\mathrm{d}T}\frac{\mathrm{d}T}{\mathrm{d}x}.$$

To translate this model in 3D, v_x has to be replaced with the average velocity $\frac{v^2}{3}$ since $v^2 = \langle v_x^2\rangle + \langle v_y^2\rangle + \langle v_z^2\rangle$ and $\langle v_x^2\rangle = \langle v_y^2\rangle = \langle v_z^2\rangle$. Also the single electrons energy can be translated into the average electron energy with $n\frac{\mathrm{d}\epsilon}{\mathrm{d}T} = \frac{N}{V}\frac{\mathrm{d}\epsilon}{\mathrm{d}T} = \frac{1}{V}\frac{\mathrm{d}E}{\mathrm{d}T} = c_v$ which gives the specific heat (from the electrons). Therefore one can write

$$\vec{q} = -\frac{v^2\tau c_v}{3}\nabla T$$

which gives in consideration of eq. (2.60) the thermal conductivity

$$\kappa = \frac{v^2\tau c_v}{3}.$$

If one divides this by σ from the DC case eq. (2.50) and insert $mv^2 = 3k_BT$ one gets

$$\frac{\kappa}{\sigma T} = \frac{c_v k_B}{ne^2} \tag{2.61}$$

which is called the Wiedemann-Franz-Law. While $v\tau = l_{\text{free}}$ is roughly constant. Rosenberg [42], notes that the law is not valid for intermediate temperatures but holds true for low and high temperatures.

2.4 Phase Effects Introduction

The following chapters discuss several distinct mechanisms that can shift the phase of an electromagnetic wave upon reflection or propagation. Since these mechanisms

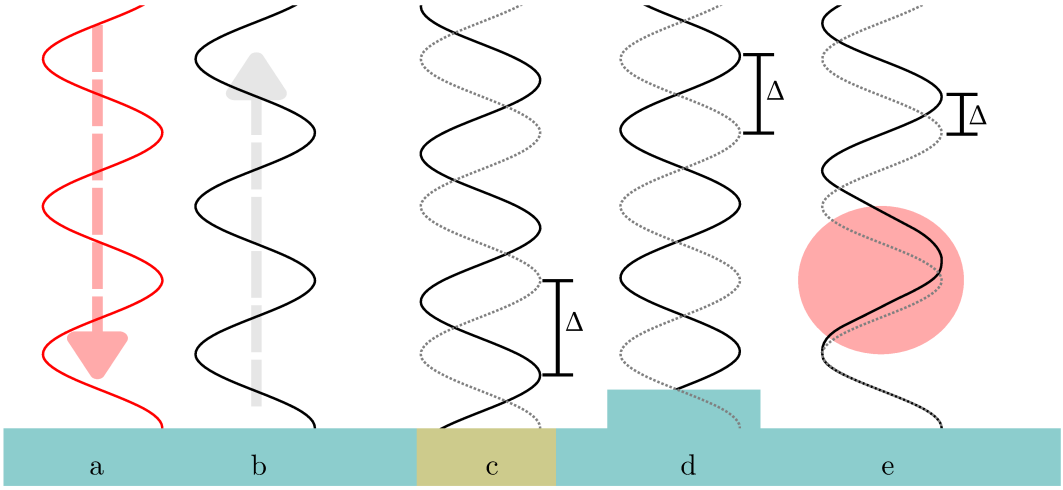


Figure 2.5: Different reasons for phase shift. a) incoming wave. b) reflected wave without phase shift. The reflected wave without phase shift is always represented as a dotted line behind the following waves. c) reflected wave with phase shift due to refractive index. d) reflected wave with phase shift due to height difference. e) phase shift due to propagation through plasma.

reappear in different contexts throughout this work, they are briefly previewed here so they can be recognized later. A detailed, quantitative summary follows once each has been derived (section 2.9).

Fig. 2.5 illustrates the three main mechanisms responsible for a phase shift between a reflected light pulse and an unshifted reference pulse. The incoming pulse (a) is supposed to be identical for all the reflected waves (b) to (e). (b) shows the simple reflected wave, where "nothing" happens. Wave (c) shows the phase shift arising from the material properties of the reflecting surface itself, which is derived in section 2.7. Wave (d) shows a phase shift caused by a physical difference in the path length to the point of reflection, relevant when the reflecting surface (e.g., a plasma density gradient) has no sharp, well-defined boundary. This is implicitly discussed in sections 2.6 and 4.2.4 but should be remembered throughout. Wave (e) shows the phase shift accumulated during propagation through a medium with an altered refractive index, such as a plasma, treated in section 2.5. Additionally, reflection can introduce a small lateral and angular displacement of the beam itself, the Goos-Hänchen and Imbert-Fedorov shifts, discussed in section 2.8.

The total phase shift observed between a probe pulse reflected from or propagated through a plasma and a reference pulse is the sum of the applicable contributions among (c)-(e), plus any lateral-shift-induced phase contribution. Notably, mechanism (c) is not unique to plasma, any reflection from a metallic surface also contributes a material-dependent phase shift that must be accounted for separately.

2.5 Plasma

While the Drude model treats metals as an electron gas moving through a fixed, immobile ion lattice, a plasma is a fully ionized gas in which both electrons and ions are free to move, with no underlying lattice structure. The mobility of the electrons can keep the plasma as well as the metal quasi-neutral on macroscopic scales while still allowing local charge imbalances and collective oscillations. However in a plasma one assumes a Maxwell-Boltzmann distribution for the velocity distribution (i.e., energy distribution k_bT), while metals would describe the electrons as a degenerate Fermi gas with $k_bT \ll E_F$ the Fermi energy, therefore their energy scale would not be thermal at all.

If matter is ionized but the electrons move freely while keeping the matter quasi-neutral overall, it is referred to as a plasma. The distance over which an electric field is shielded is the Debye length

$$\lambda_D = \sqrt{\frac{\varepsilon_0 k_B T}{e^2 n_e}}, \tag{2.62}$$

which depends on the electron density n_e and electron temperature T.

Electromagnetic waves with frequency ω_L below the plasma frequency ω_p (2.54) cannot propagate: in the collisionless limit ($\omega_L \tau \gg 1$), the Drude model gives $\varepsilon_r(\omega_L) = 1 - \omega_p^2/\omega_L^2$ (2.56), which is negative for $\omega_L < \omega_p$. The refractive index $n = n_0 + i\beta$ (2.57) is then purely imaginary, so the wavevector $k = \omega_L n/c_0$ is imaginary as well, and the field decays as $\vec{E}(z) \propto e^{-z/d_s}$ instead of propagating. The characteristic decay length

$$d_s = \frac{c_0}{\sqrt{\omega_p^2 - \omega_L^2}} \approx \frac{c_0}{\omega_p} \tag{2.63}$$

is the skin depth, where the amplitude is attenuated to $1/e$. At higher frequencies ($\omega_L > \omega_p$) the wave propagates. Since the electron density of a plasma typically decreases toward its edge, an electromagnetic wave can often propagate into the plasma initially but is absorbed or reflected before reaching the critical density where $\omega_L = \omega_p$.

$$n_c = \frac{m_e \varepsilon_0 \omega_L^2}{e^2} = \frac{4\pi^2 \varepsilon_0 m_e c_0^2}{e^2 \lambda_0^2} \tag{2.64}$$

which will be later discussed in more detail in section 4.2.4. Plasma with $n_e > n_c$ is referred to as supercritical or dense, while plasma with $n_e < n_c$ is referred to as subcritical or thin. It should be noted that $n_c(\lambda_0) \propto \frac{1}{\lambda^2}$ applies and therefore different

colors can be reflected at very different positions. λ_0 describes the wavelength in a vacuum, as it changes when the refractive index changes. The dispersion relation for electromagnetic waves in plasma is

$$\omega^2 = c_0^2 k^2 + \omega_p^2 \tag{2.65}$$

which leads to a phase velocity of

$$v_p = \frac{\omega}{k} = c_0 \cdot \sqrt{1 + \frac{\omega_p^2}{c_0^2 k^2}} \tag{2.66}$$

which is higher than c. Still the group velocity

$$v_g = \frac{\partial \omega}{\partial k} = \frac{k c_0^2}{\sqrt{k^2 c_0^2 + \omega^2}} \tag{2.67}$$

is lower than c. This means that a pulse of light travels still slower than the speed of light but the phase of the wave inside of the pulses envelope travel faster. Due to the dispersion miss-match there will be pulse broadening as explained in eq. (2.27). The refractive index of a collisionless plasma can then be described as

$$n_p = \frac{1}{\sqrt{1 + \frac{\omega_p^2}{c_0^2 k^2}}} = \frac{1}{\sqrt{1 + \frac{n_e}{n_c(\omega) - n_e}}}. \tag{2.68}$$

In case of $n_c > n_e$ the refractive index $1 > n_p > 0$. If light is behind the critical density $n_c < n_e$ the refractive index is completely imaginary with $\Im(n_p) < 0$. It has to be noted, that if $\frac{1}{\sqrt{1+x}} = \sqrt{1-x}$ is reshaped, the sign of the imaginary part is flipped. Therefore, the more general form which considers also collisions in the plasma has to be used for accurate results. It will be discussed in the next section.

2.5.1 Appleton-Hartree Equation

The Appleton-Hartree equation was originally developed for radio transmission purposes in the upper atmosphere, but it generally applies to cold plasma. For the complete formulation, a static magnetic field is present in the plasma, which does not occur in this work but has been included in the formula for the sake of completeness. Here the refractive index

$$n^2 = 1 - \frac{X}{1 - iZ - \frac{Y_T^2}{2(1-X-iZ)} \pm \sqrt{\frac{Y_T^4}{4(1-X-iZ)^2} + Y_L^2}} \tag{2.69}$$

with

$$X = \frac{\omega_p^2}{\omega^2}, \quad Y = \frac{\omega_G}{\omega}, \quad Y_L = \frac{\omega_G \cos\theta}{\omega}, \quad Y_T = \frac{\omega_G \sin\theta}{\omega}, \quad Z = \frac{\nu}{\omega}$$

where the Gyro Frequency $\omega_G = \frac{B_0 e}{m}$ and the electron collision frequency ν are introduced. Since the external $B_0 = 0$ for this work also $Y = Y_L = Y_T = 0$ and the formula breaks down to

$$n^2 = 1 - \frac{\omega_p^2}{\omega(\omega - i\nu)} \tag{2.70}$$

which is described in [43]. To approximate the collision frequency the electron-electron ν_{ee} and electron-ion ν_{ie} collisions have to be approximated using:

$$\nu_{ee} = \sqrt{\frac{2}{m_e(\pi k_B T_p)^3}} \cdot n_e \frac{e^4}{12\epsilon_0^2} \ln\Lambda \tag{2.71}$$

$$\nu_{ei} = \sqrt{\frac{2}{m_e(\pi k_B T_p)^3}} \cdot n_i \frac{Z^2 e^4}{12\epsilon_0^2} \ln\Lambda \tag{2.72}$$

$$\nu = \sqrt{\nu_{ei}^2 + \nu_{ee}^2}. \tag{2.73}$$

with the coulomb logarithm:

$$\ln\Lambda \approx \ln\left(1.5 \times 10^{13} \cdot \sqrt{\frac{T_p^3}{ne}}\right) \tag{2.74}$$

and the plasma temperature T_p in Kelvin [44]. For plasma in local thermal equilibrium (LTE) [45], the ionization states and respective electron and ion densities can be calculated from the temperature and number density n_i according to the Saha equation

$$\frac{n_{i+1} n_e}{n_i} = \frac{2}{\lambda_{\mathrm{th}}^3} \frac{g_{i+1}}{g_i} \exp\left[-\frac{\varepsilon_{i+1} - \varepsilon_i}{k_B T_p}\right] \tag{2.75}$$

with the degeneracy of state g_i, energy levels ε_i, and thermal de Broglie wavelength of an electron λ_{th}. It is solved according to Zaghloul [46], implemented by Riedlinger [47], or using the FLYCHK database [37]. For copper the real and imaginary part

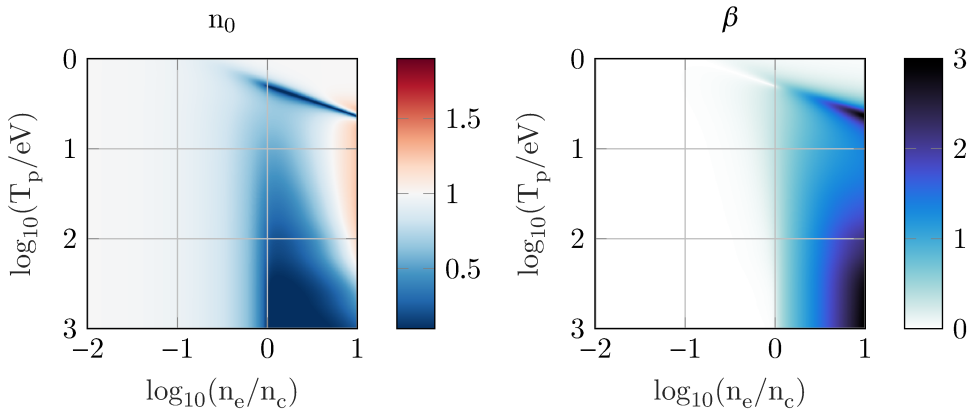


Figure 2.6: Real part n_0 and extinction coefficient β of the plasma's refractive index depending on plasma temperature T_p and electron density n_e.

of the refractive index are shown in fig. 2.6. It can be seen, that the plasma exhibits $n_0 < 1$ in the are in front of the critical density n_c, also the extinction coefficient β falls sharply behind the critical density, while staying $\beta \approx 0$ in the area in front. Some interesting features are the fact, that deep inside the plasma $n_e \approx 10 n_c$ the refractive index $n_0 > 1$ for temperatures $T_p = 10\,\mathrm{eV}$ to $100\,\mathrm{eV}$. This is however not of high importance for the further part of this work, since everything will happen in front of the critical density. Actually interesting however is n_0 at the critical density $n_e \approx n_c$ in the area $T_p = 2\,\mathrm{eV}$ to $10\,\mathrm{eV}$, where n_0 is significantly closer to 1 than for the other temperatures. This happens due to the solutions of the Saha equation for low temperature plasma, where the ionization potentials often exhibit complicated behavior. While this is also not of high relevance, since calculated plasma temperatures for this work will be $T_p > 10\,\mathrm{eV}$, consequences of this effect will later come up again in eq. (4.16) and the related chapter.

2.6 Refractive Index Gradients

To calculate the reflection of a laser pulse in plasma, one could argue that it can be modeled by refraction due to the refractive index gradient, since the electron density of the plasma does not have a sharp edge. Here the plasma density n_e is assumed to expand in the z direction. A good first assumption would be

$$n_e(z) = n_0 e^{-L \cdot z}. \tag{2.76}$$

Therefore, the refractive index is

$$n_p(z) = \frac{1}{\sqrt{1 + \frac{\omega_p^2}{c_0^2 k^2}}} = \frac{1}{\sqrt{1 + \frac{n_0 e^{-z/L}}{n_c(\omega) - n_0 e^{-z/L}}}}. \tag{2.77}$$

Considering the wave travels in the x-z plane and the gradient of the plasma is in z direction. The first order gradient

$$\nabla n(z) = \begin{pmatrix} 0, 0, \frac{n_0 e^{-z/L} \cdot \sqrt{\frac{n_c e^{z/L}}{-n_0 + n_c e^{z/L}}}}{2 n_c L} \end{pmatrix} \tag{2.78}$$

can be used for numerical solutions of a photon path through the plasma. This concept will be further expanded upon in later chapters, after the specialized ray tracing used in this work has been introduced.

2.7 Fresnel Description

To evaluate how light will reflect and refract on surfaces (i.e., mainly metals) the standard Fresnel description for complex refractive indexes is described in this section. Furthermore the adaptions necessary to calculate the effects of absorbing media are presented. One shall keep in mind, that the refractive index is always to be assumed complex, if not specifically stated otherwise.

This section uses the indexes i = incident, r = reflected, t = transmitted, p = p-polarized and s = s-polarized. When calculating the reflection and transmission of electric waves with surfaces usually the Fresnel equations for reflection

$$\hat{e}_{k,r} = \hat{e}_{k,i} - 2(\hat{e}_{k,i} \cdot \hat{n})\hat{n} \tag{2.79}$$

and transmission

$$\hat{e}_{k,t} = \frac{n_i}{n_t} \cdot \hat{e}_{k,i} + \left(\frac{n_i}{n_t} \hat{n} \cdot \hat{e}_{k,i} - \Re \left(\sqrt{1 - \frac{n_i}{n_t}(1 - \cos(\theta_i)^2)} \right) \right) \hat{n} \tag{2.80}$$

are used. Here $\hat{e}_k = \frac{\vec{k}}{\|\vec{k}\|}$ is the normalized wave propagation vector and $\hat{n}$ is the normal vector of the surface at which reflection occurs. For this description to work, the refractive indexes n_i (material on side of incidence) and n_t (material on side of diffraction) have to be real in this case, as well as the angle of incidence. The widely used formulation of

$$n_i \sin(\theta_i) = n_t \sin(\theta_t) \tag{2.81}$$

can be written as $\theta_t = \arcsin\left(\frac{n_i}{n_t}\sin(\theta_i)\right)$ which gives the angle of refraction. Here the complex refractive index can and has to be used for further implementation into eqs. (2.86) to (2.89). But since the angle is complex for complex refractive indexes it cannot be easily interpreted any more. Therefore, another approach has to be taken for metals and absorbing plasma. As a simple approximation when the incident medium is non absorbing (i.e., $\beta_i = 0$) one can use

$$\theta' = \arcsin\left(\frac{n_i}{n'}\sin(\theta_i)\right) \tag{2.82}$$

with

$$n' = \sqrt{\frac{a}{2}\left(1 \pm \sqrt{1 - \frac{4b}{a^2}}\right)} \tag{2.83}$$

where $a = n_t^2 - \beta_t^2 + \sin^2\theta_i$ and $b = (n_t^2 - \beta_t^2)\sin^2\theta_i - n_t^2\beta_t^2$ according to [48]. A better and more correct way however is to describe the direction of propagation by the Poynting vector (see section 2.7.2). To do this however the electric fields and their behavior upon reflection need to be fully described.

2.7.1 Electric Field Description

An electric field vector in 3D-space can be displayed as

$$\vec{E} = \begin{pmatrix} E_x e^{-i\phi_x} \\ E_y e^{-i\phi_y} \\ E_z e^{-i\phi_z} \end{pmatrix} \tag{2.84}$$

with the relative phase ϕ_α[3] of each component $\alpha \in [x, y, z]$. Usually a projection into the incident plane is chosen, where the electric field is split into $E_p = E_x$ and $E_s = E_y$. Since multiple interacting electric fields propagating in arbitrary 3D directions are evaluated here, it is more suitable to formalize everything for an arbitrary 3D vector to prevent unnecessary rotation/transformation steps.

If a wave interacts with a surface the p- and s-polarized parts of the electric

[3]Technically, the electric field would be expressed as $\vec{E} = \begin{pmatrix} \tilde{E}_x \\ \tilde{E}_y \\ \tilde{E}_z \end{pmatrix}$ with $\tilde{E}_\alpha = E_{0,\alpha} e^{-i(\omega t - \vec{k}\vec{r} + \phi_\alpha)}$.
When simulating/ray tracing the electric field, $\omega t \gg \phi_\alpha$ is usually the case. Attempting to determine the relative phase of two different rays with eq. (2.91) therefore often leads to the problem that arctan is defined for $[-\pi, \pi]$, while $\Delta\phi$ is usually much greater or lower, making analysis difficult or impossible. Therefore, it is useful to store only the phase jumps due to reflection or unusual polarization within the phase component of the electric field and to store the time t independently. This makes it easier to unfold the phase and then calculate the total phase $\phi_{\text{total},\alpha} = (\omega t - \vec{k}\vec{r} + \phi_\alpha)$ after all calculated reflections/transmissions.

field behave differently. Therefore, it is necessary to depict the incident wave as $\vec{E}_i = \vec{E}_{p,i} + \vec{E}_{s,i}$. The polarized fields have to be constructed by $\vec{E}_{s,i} = (\hat{s} \cdot \vec{E}_i)\hat{s}$ and $\vec{E}_{p,i} = (\hat{p}_i \cdot \vec{E}_i)\hat{p}_i$ but are only valid for one single interface interaction, since $\hat{s} = \hat{n} \times \hat{e}_{k,i}$ and $\hat{p}_i = \hat{s} \times \hat{e}_{k,i}$. For each following surface interaction they must be calculated again. One can see that $\hat{p}_i$ has an index indicating the direction, while $\hat{s} = \hat{s}_i = \hat{s}_r = \hat{s}_t$ does not need one, since the direction of the outgoing s-polarized field is the same as the incident field, while for the p-polarized field the direction changes depending on the direction of the wave vector.

Using this description the differences of the individual reflections can be combined again with

$$\vec{E}_r = r_p \vec{E}_{p,r} + r_s \vec{E}_{s,r}. \tag{2.85}$$

Since $\vec{E}_{s,i} = \vec{E}_{s,r}$ only the p-pol part has to be calculated by $\vec{E}_p, r = 2(\hat{n} \cdot \vec{E}_{p,i})\hat{n} - \vec{E}_{p,i}$. It is important to remember that the electric field is complex (eq. (2.84)). The scalar product for complex numbers is defined as $\vec{a} \cdot \vec{b} = \sum_i \overline{a_i}\, b_i$ in this case, so that the phase of the complex part is never flipped. The reflection coefficients have to be calculated with

$$r_p = \frac{\frac{n_t}{\mu_t}\cos(\theta_i) - \frac{n_i}{\mu_i}\cos(\theta_t)}{\frac{n_t}{\mu_t}\cos(\theta_i) + \frac{n_i}{\mu_i}\cos(\theta_t)} \tag{2.86}$$

and

$$r_s = \frac{\frac{n_i}{\mu_i}\cos(\theta_i) - \frac{n_t}{\mu_t}\cos(\theta_t)}{\frac{n_i}{\mu_i}\cos(\theta_i) + \frac{n_t}{\mu_t}\cos(\theta_t)}. \tag{2.87}$$

The transmission coefficients would be

$$t_p = \frac{2\frac{n_i}{\mu_i}\cos\theta_i}{\frac{n_t}{\mu_t}\cos\theta_i + \frac{n_i}{\mu_i}\cos\theta_t}, \tag{2.88}$$

and

$$t_s = \frac{2\frac{n_i}{\mu_i}\cos\theta_i}{\frac{n_i}{\mu_i}\cos\theta_i + \frac{n_t}{\mu_t}\cos\theta_t}. \tag{2.89}$$

all with the magnetic permeability of each respective material μ_i and μ_t. Those coefficients are used to calculate the reflectivity as $R_p = r_p^2$ and $R_i = r_i^2$[4]. There also holds conversation of energy with $T_p = 1 - R_p$ and $T_s = 1 - R_s$.

[4]It has to be noted, that the signs of the coefficients are flipped in some literature since usually only the square $R_p = r_p^2$ and $R_i = r_i^2$ are evaluated

In addition to its new direction the new strength of the reflected electric field can be calculated by

$$E_\alpha = \vec{E}_r \cdot \hat{e}_\alpha \tag{2.90}$$

for each respective dimension $\alpha \in [x, y, z]$. Additionally the wave also starts at a different phase, which can be calculated with

$$\phi_\alpha = \arctan\left(\frac{\Im(\vec{E}_r \cdot \hat{e}_\alpha)}{\Re(\vec{E}_r \cdot \hat{e}_\alpha)}\right) \tag{2.91}$$

also for each dimension. This property can be used to construct the electric field according to eq. (2.84) which can show a phase shift in each component $\Delta\phi_\alpha$ if different fields are compared to each other. Also the effective polarization of the electric field can be evaluated in direction of the propagation $\hat{e}_k$ of the wave. Therefore, the plane in which the electric field oscillates is spanned with $\hat{e}_u$ and $\hat{e}_v$, which fulfill $\hat{e}_u \times \hat{e}_v = \hat{e}_k$ and $\hat{e}_u \cdot \hat{e}_v = 0$, wherefore

$$\Delta\phi = \arctan\left(\frac{\Im(\vec{E}_r \cdot \hat{e}_u)}{\Re(\vec{E}_r \cdot \hat{e}_u)}\right) - \arctan\left(\frac{\Im(\vec{E}_r \cdot \hat{e}_v)}{\Re(\vec{E}_r \cdot \hat{e}_v)}\right) \tag{2.92}$$

which becomes $\Delta\phi = 0$ for linear polarization, $\Delta\phi = \pm\frac{\pi}{2}$ for circular polarization or elliptical polarization for anything else.

2.7.2 Absorbing Media

To construct the Poynting vector when entering absorbing media, both $\vec{k}_t$ and $\vec{E}_t$ have to be deconstructed in s and p polarized parts, such that

$$\vec{E}_t = E_{s,t}\hat{e}_{s,t} + E_{p,t}\hat{e}_{p,t} \tag{2.93}$$

While $E_{s,t} = t_s E_{s,i}$ and $E_{p,t} = t_p E_{p,i}$ are easily calculated with the transmission coefficients from (2.88) and (2.89), and $\hat{e}_{s,t} = \hat{e}_{s,i}$, the p-polarized unit vector needs a bit more construction. The surface normal $\hat{n}$ has to point in the direction of the incident medium (i.e., opposite to k_i). One starts with the p-polarized part of $\vec{k}$ which is

$$\vec{k}_\parallel = \vec{k}_i - (\vec{k}_i \cdot \hat{n})\hat{n} \tag{2.94}$$

which can be used to construct the complex value

$$k_{t,n} = \sqrt{k_0^2 n_t^2 - k_\parallel^2} \tag{2.95}$$

with $k_0 = \frac{2\pi}{\lambda}$ being the $\vec{k}$ length in vacuum. Then construct

$$\vec{\tilde{k}}_t = \vec{k}_{\parallel} + k_{t,n}\hat{n} \tag{2.96}$$

which can then finally be used to construct the p-polarized unit vector

$$\hat{e}_{p,t} = \frac{\hat{e}_{s,t} \times \vec{\tilde{k}}_t}{||\hat{e}_{s,t} \times \vec{\tilde{k}}_t||}. \tag{2.97}$$

Note, that this unit vector is complex, Thus the transmitted electric field is constructed, which can then be used to construct the transmitted magnetic field with

$$\vec{H}_t = \frac{1}{\mu_0 \mu_r \omega} \vec{\tilde{k}}_t \times \vec{E}_t \tag{2.98}$$

which can then be used to construct the Poynting vector

$$\vec{S}_t = \frac{1}{2}\Re(\vec{E}_t \times \vec{H}_t^*) \tag{2.99}$$

with the complex conjugate of the magnetic field. This accurately describes the direction of propagation in an absorbing medium.

2.7.3 Lenses

Lenses are used to focus and image light fields and are one of the fundamental concepts of optical systems. However, since some very important properties of lenses and their aberrations are discussed in later chapters, it is necessary to define some of the basics here or expand on them if necessary.

2.7.3.1 Thin Lenses

For a thin lens (thickness negligible compared to curvature radii and system distances), refraction is approximated as occurring in a single plane, so the lens is fully characterized by its aperture and focal length f. Parallel incident rays are focused at distance f; conversely, a point source at f produces a collimated output beam. The sign of f distinguishes converging ($f > 0$) from diverging ($f < 0$) lenses, the latter producing a virtual focal point on the incident side.

For an object at distance z_1 from a thin lens, the image distance z_2 follows from the thin-lens equation

$$\frac{1}{f} = \frac{1}{z_1} + \frac{1}{z_2}, \tag{2.100}$$

valid for paraxial rays. Negative z_2 denotes a virtual image on the incident side. The magnification is $M = -z_2/z_1$, the minus sign indicating inversion of real images.

2.7.3.2 Quadratic Phase Transformation of the Electric Field

In wave optics, this property of a thin lens is described by its effect on the complex electric field. Assuming an arbitrary electric field $\vec{E}_{\text{in}}(x, y)$ propagating along z with the lens in x, y.

A thin lens modifies this field by imposing a spatially varying phase shift while leaving the amplitude unchanged (neglecting absorption). The output field immediately after the lens is given by

$$\vec{E}_{\text{out}}(x, y) = \vec{E}_{\text{in}}(x, y) \cdot \exp\left(-i\frac{k(x^2 + y^2)}{2f}\right). \tag{2.101}$$

This expression is known as the quadratic phase function of a thin lens and will later be used for diffraction calculations (see section 4.4).

Physically, the quadratic phase term converts a planar incident wavefront into a spherical wavefront that converges to the focal point at a distance f.

2.7.3.3 Aperture and Numerical Aperture

In any real optical system, the physical size of the lens limits the angular range in which light can pass through the lens. This cutting of light is described by the aperture a (diameter of the lens), which is often modeled by a transfer function $g(x, y)$, which can be a sharp rectangular function

$$g(x, y) = \begin{cases} 1, & r < a \\ 0, & r \geq a \end{cases}, \qquad r = \sqrt{x^2 + y^2} \tag{2.102}$$

or sometimes, depending on the application, a smoother super-Gaussian function

$$g_{\text{smooth}}(x, y) = \exp\left[-\left(\frac{r^2}{2a^2}\right)^N\right] \tag{2.103}$$

with a suitably high number $N \in \mathbb{N}$. The latter effectively generates a rectangular function with slightly smoother edges, which facilitates numerical modeling, since sharp edges generate artifacts in the Fourier domain.

A particularly important parameter for the aperture is NA, defined as

$$\text{NA} = n \sin(\theta) \tag{2.104}$$

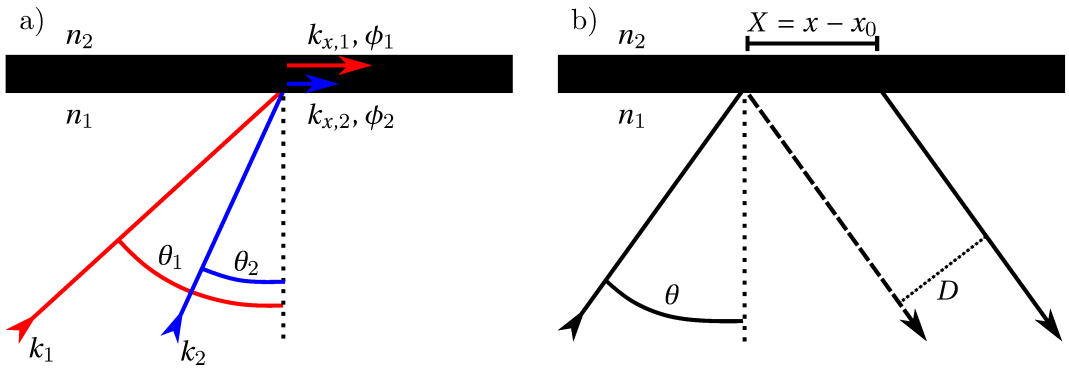


Figure 2.7: Total reflection at an interface with refractive index n_2 can cause a lateral displacement D resulting in an offset of the reflected beam. a) sketches the conceptual elementary waves with different incident angles, overlapping and creating different standing waves on the surface (k_x, i), with different phase shifts ϕ_i. Whereby it follows that in b) the reflected beam does not come from the initial position (as would be according to Fresnel optics), but starts at an offset X, leading to the displacement D.

where n is the refractive index of the medium between the object and the lens and θ is the maximum half-angle of the rays entering the lens. In combination with eq. (2.100), this effectively results in

$$\mathrm{NA} = n \cdot \sin\left[\arctan\left(\frac{a}{2z_1}\right)\right] \approx n \cdot \frac{a}{2z_1} \tag{2.105}$$

for most real-world applications in which a lens is used to produce an image of an object.

2.8 Goos-Hänchen-Shift

In 1947 Goos and Hänchen showed that after total reflection or reflection on a metallic surface a lateral shift of the reflected beam can occur which translates to a transverse displacement [32]. While a shift in the plane of incidence is denoted as the Goos-Hänchen (GH) shift a shift perpendicular to this plane is called the Imbert-Fedorov (IF) shift [33, 49]. Also an angular shift in both directions can occur [50] (i.e., $\theta_{\mathrm{in}} \neq \theta_{\mathrm{out}}$, however, this shift is extremely small and not important for any known real world use case). Since those shifts are usually in the range of a few wavelengths they can potentially greatly disrupt phase images if they are not correctly discussed and considered for the given geometry.

At the moment of writing it seems as if there is no consensus on the correct theoretical description. While for total reflection experimental data exists, it does

not seem so for reflection on metals. Also the different models predict widely different shifts, sometimes even in opposite directions. Therefore, the most promising concepts for a first-order approximation are presented and their results compared.

2.8.1 Artmanns Description - Steady Phase

This chapter evolves around the first description made by Artmann in 1948 [51]. Here an electromagnetic wave is considered as the superposition of many elemental waves with plane wavefronts traveling in different directions. These elemental waves reflect with their different angles at the surface and each can experience a different phase shift as described in (2.91) as long as the reflective index is either complex (metal) or the angle for total reflection is exceeded.

The incoming wave has the initial wavelength λ_1 and wave vector $k_1 = \frac{2\pi}{\lambda_1}$ which has an angle to the surface of θ_1. The surface is assumed to be flat in the x-direction and the surface normal points in the y-direction (see fig. 2.7 a)). Then the electric field of each elemental wave that travels along the direction of the surface can be denoted with the wave number

$$k_x = k \cdot \sin(\theta) = \frac{2\pi}{\lambda} \cdot \sin(\theta) \tag{2.106}$$

and since every elemental wave has a different angle θ, there will be a superposition of each of those surface waves. For simplicity it will be assumed only two elemental waves exist. A surface wave can then be described as

$$E = e^{i(k_x x + \phi(\theta))} \tag{2.107}$$

wherefore the first wave becomes

$$E_1 = e^{i(k_{x,1} x + \phi_1)},$$

but since the other wave has a different angle, it has a slightly different wave number $k_x(\theta_2) = k_{x,1} + \Delta k_x$ and since the phase depends on the angle of incidence also a different phase $\phi(\theta_2) = \phi_1 + \Delta\phi$. Thus,

$$E_2 = e^{i[(k_{x,1}+\Delta k_x)x + \phi_1 + \Delta\phi]}.$$

This combined wave of

$$E_1 + E_2 = e^{i(k_{x,1} x + \phi_1)} \cdot \left[1 + e^{i(\Delta k_x x + \Delta\phi)}\right]$$

shows that there is a beat with a periodicity of

$$\Delta k_x x + \Delta\phi = 2\pi n,\ n \in \mathbb{N}.$$

Without the phase shift the periodicity would have been

$$\Delta k_x x_0 = 2\pi n,\ n \in \mathbb{N}$$

which is just the well known case for geometrical optics. Therefore, the difference between those beats is

$$X = x - x_0 = -\frac{\Delta\phi}{\Delta k_x}$$

and can be compressed for $\Delta \to 0$ to the differential equation

$$X = x - x_0 = -\frac{\mathrm{d}\phi}{\mathrm{d}k_x}. \tag{2.108}$$

While this approach would yield a standing wave at the surface, considering infinitely many elemental waves will reduce the periodicity down to only one single maximum. Since Goos and Hänchen described the shift as pictured in fig. 2.7 b), the formula has to be modified to

$$D = -\cos(\theta_i) \cdot \frac{\mathrm{d}\phi}{\mathrm{d}k_x}$$

which can be rewritten to

$$D = -\frac{\lambda_1}{2\pi} \cdot \frac{\mathrm{d}\phi}{\mathrm{d}\theta_i}. \tag{2.109}$$

While Artmann used

$$\phi = -2\arctan\left[\frac{\sqrt{\sin(\theta_i)^2 - (n_2/n_1)^2}}{\cos(\theta_1)}\right] \tag{2.110}$$

to calculate the phase at total reflection, this approach is not suitable to calculate the phase for metallic reflections, since the complex refractive index is not considered correctly and the formula from (2.91) has to be taken instead. This can then be used to calculate the GH shift numerically with (2.109). Since the phase changes differently for s- and p-polarization, the shift is also different for s- and p-polarization and has to be calculated separately. It is possible to find an analytic solution for the steady phase approach which condenses to

$$D_s = \frac{\lambda}{\pi\sqrt{n_1^2 \sin^2(\theta_i) - n_2^2}}, \tag{2.111}$$

$$D_p = \frac{D_s}{\sin^2(\theta_i) \cdot \left[\left(\frac{n_1}{n_2}\right)^2 + 1\right] - 1} \tag{2.112}$$

which is a slightly different notation than Artmann's, but works with metals and dielectrics as long as the phase is steady and has no jumps. It has to be noted, that this approach collapses near the Brewster angle and does not yield correct results when the reflectivity approaches zero.

2.8.2 Complex Shifts

While the above approximation is just of first order, additionally to the spatial shift of the point of reflection, there is also a very small shift in the angle of reflection. The angular GH shift Θ_{GH} slightly adjusts the angle of reflection with $\theta_i = \theta_r + \Theta_{\mathrm{GH}}$. This shift occurs in the plane of reflection that would be spanned by the Fresnel description. Similarly there is an angular IF shift Θ_{IF} which tilts the direction of the reflected beam away from the plane of reflection. Therefore, the plane of reflection cannot be described in 2 dimensions any more. Described by Aiello [50] GH and IF shifts can be calculated from a complex shift with

$$\begin{aligned} \Delta_{i_t} &= \frac{\lambda}{2\pi}\Im(D_{i_t}) \\ \Theta_{i_t} &= -\frac{\theta_0^2}{2}\Re(D_{i_t}) \end{aligned} \tag{2.113}$$

where i denotes either p or s-polarization and t donates GH or IF. $\theta_0 = \frac{\lambda}{\pi w_0}$ describes the angular spread of a Gaussian beam with the Gaussian width w_0. The coefficient D_i is either

$$D_{i_{\mathrm{GH}}} = \frac{\partial \ln r_i}{\partial \theta} \tag{2.114}$$

for the GH shifts or

$$D_{i_{\mathrm{IF}}} = 2i\frac{r_p + r_s}{r_i}\cot(\theta) \tag{2.115}$$

for the IF shifts.

2.9 Phase Effects Summary

Having derived each mechanism from fig. 2.5 individually, this section collects the results and illustrates their combined effect using the reflection coefficients and shift formulas obtained above.

Material-induced phase shift (c): If light is reflected almost perpendicular, the difference between p- and s-polarized light is always $\Delta\phi = \phi_s - \phi_p = -\pi$ (as can be verified from eqs. (2.86) and (2.87)). This follows directly from the geometry of the situation. Suppose one moves with diagonally polarized light oscillating from the top right to the bottom left. Now one reflects off a flat mirror that is almost perfectly perpendicular (not exactly perpendicular, since in that case there would be no p-polarized component). Viewed from the original perspective, the reflected beam would still oscillate from the top right to the bottom left. However, since the direction has reversed as it is reflected toward the observer, the beam now oscillates from the top left to the bottom right from the beam's perspective. The beam remains linearly polarized throughout. This π-flip is a sign convention inherent to the Fresnel formalism and does not correspond to an actual delay in time or space, i.e., no dispersion is introduced.

Additionally, if the extinction coefficient of the reflecting material is nonzero ($\beta > 0$), the phase shift is offset from these values, $\phi_s \neq 0$ and $\phi_p \neq \pi$. This offset also varies with the angle of incidence, allowing $\Delta\phi$ to take on other values and thereby produce elliptical or circular polarization states. This effect also underlies the Goos-Hänchen and Imbert-Fedorov shifts discussed later.

Path-length-induced phase shift (d): As is discussed quantitatively in section 2.6, this contribution arises whenever the effective point of reflection is physically displaced, as is generically the case for a plasma density gradient, where no single reflection point can be uniquely defined (section 4.2.4). Any physically shorter path (in time or space) relative to the reference beam produces a corresponding phase shift.

Propagation-induced phase shift (e): This comes from the change in refractive index along the propagation path which shifts the accumulated phase. In typical solids or fluids, the reduced phase velocity produces a phase lag, i.e., light travels slower. In a plasma, the phase velocity exceeds $c_0 < c_{\text{plasma}}$ (2.66), producing a phase lead instead.

Beam-displacement phase shift: Beyond the effects above, reflection itself can laterally and angularly displace the beam (Goos-Hänchen and Imbert-Fedorov shifts,

section 2.8), which introduces an additional, geometry-dependent phase contribution when comparing beams across an extended interaction region. Shifts according to both theoretical frameworks (section 2.8.1 and section 2.8.2) are presented for silver mirrors with external (incident in vacuum, reflecting on silver, fig. 2.8) and internal (incident from Fused Silica, reflecting on vacuum, fig. 2.9) reflection. It is shown, that those shifts can potentially be quite high ($D \sim 1\,\mu\text{m}$) but will be negligible for the given angles and materials, where they occur only in the range of $D \sim 10\,\text{nm}$.

The total phase shift between a probe pulse reflecting from or propagating through a plasma and a reference pulse is therefore the sum of all applicable contributions above. It shall be mentioned, that contribution (c) is not unique to plasma diagnostics. Any reflection from a metallic surface also introduces a material-dependent phase shift that must be regarded separately from the plasma's contribution. The total quantitative effects will be seen after the simulation chapter 4.

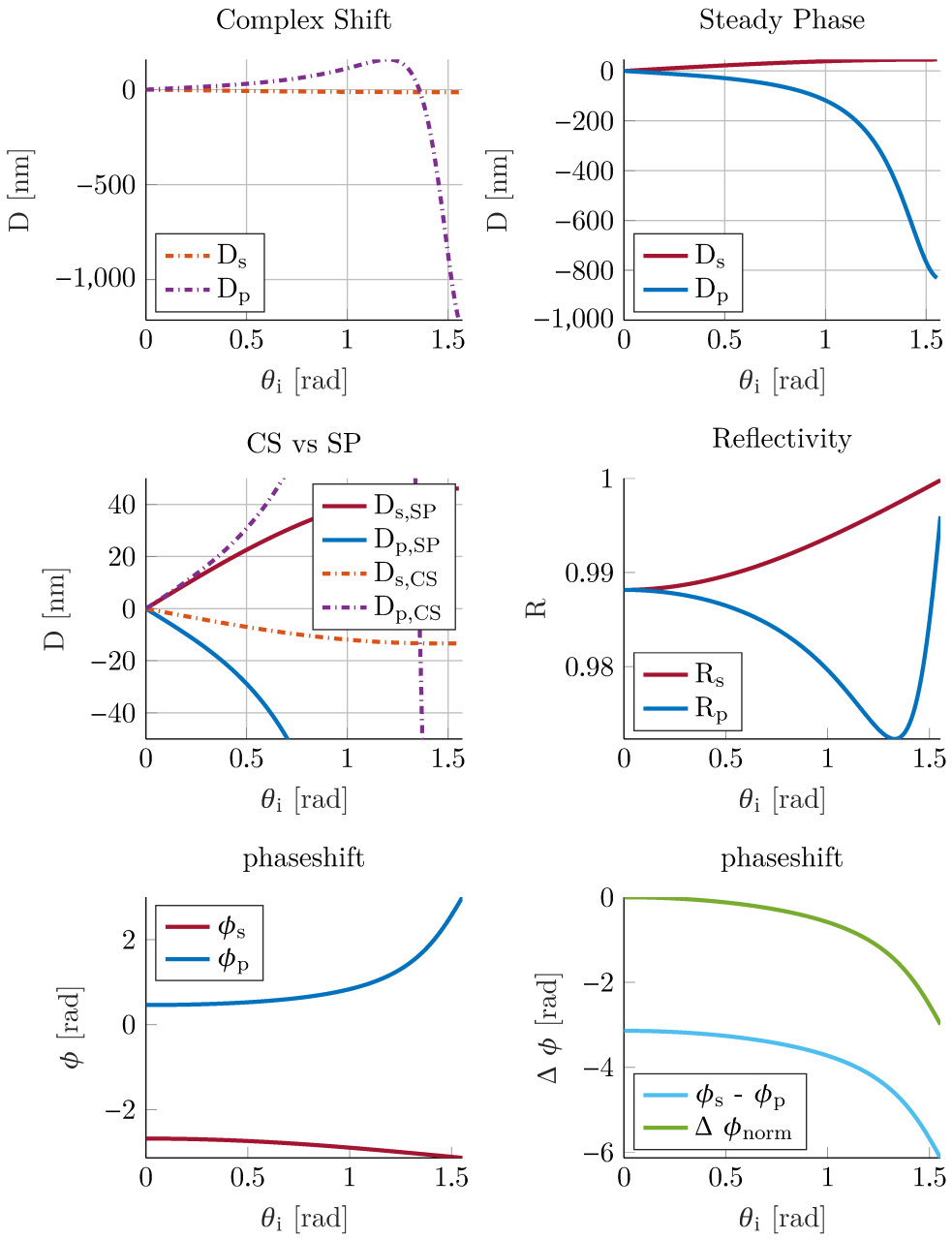


Figure 2.8: Goos-Hänchen Shift of a helium-neon laser incident in vacuum, reflecting on a silver mirror.

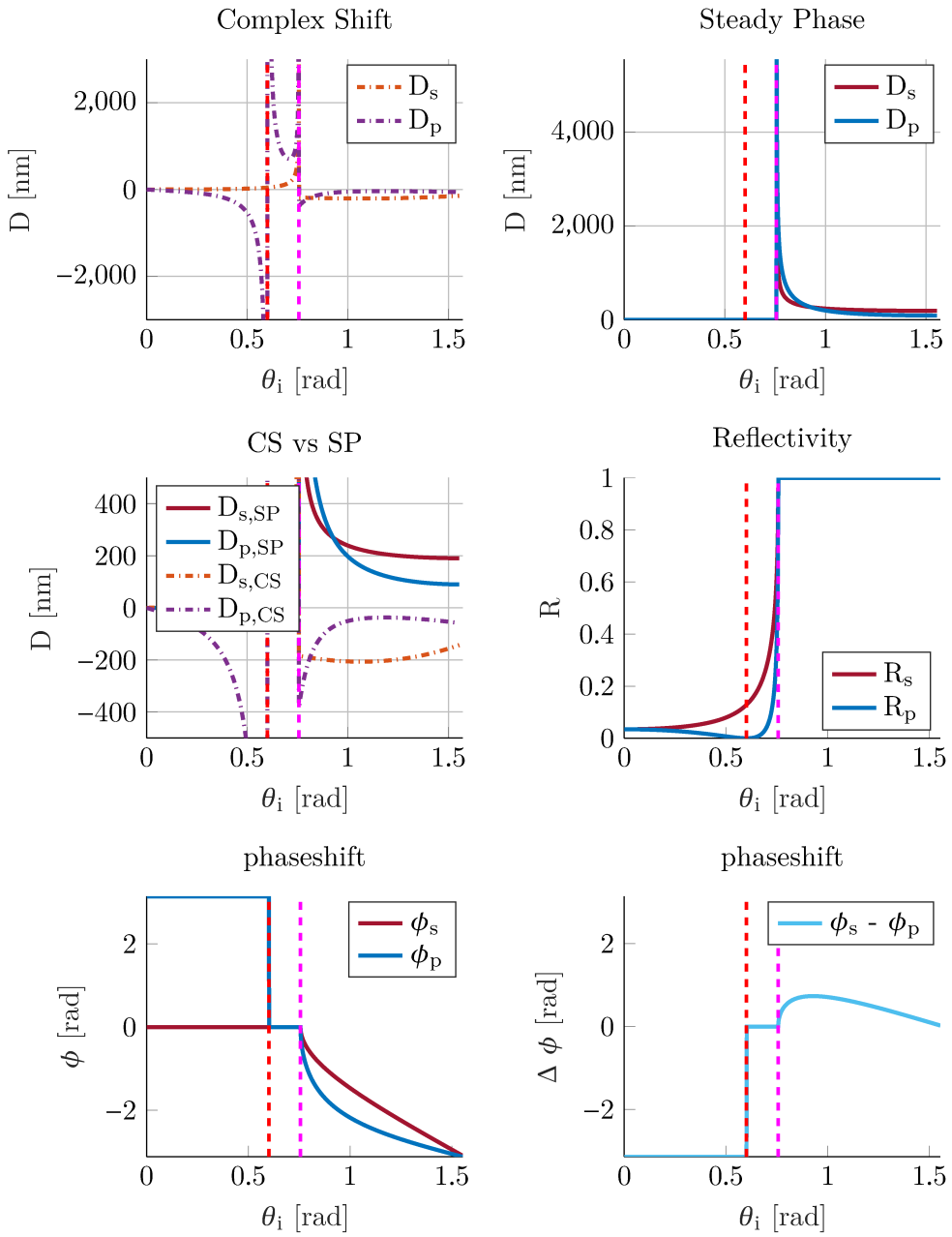


Figure 2.9: Goos-Hänchen Shift at internal reflection of a helium-neon laser inside Fused Silica on Vacuum. The orange dotted line denotes the Brewster angle, the pink line shows the critical angle.

2.10 Phase Images

The term "phase image" has many meanings, ranging from contrast-enhanced edge detection images to spectral phase images. In this work, a phase image is an image that shows the deformation of the wavefront of a laser pulse. The algorithm to produce those images out of an interference image is an alteration on [52, 53].

2.10.1 Algorithm

An interference image contains all information of an extended light beam's spatial phase distribution, if the reference beam's phase is known. However, extracting this information from an image requires a numerical algorithm which at the same time smooths the noisy data. The algorithm can work in 2D or 1D respectively, either way by splitting the interference image into lineouts perpendicular to the fringes or doing all the transformations in 2D. While the algorithm is performed in 2D for the evaluations in this work (since it is computationally faster), this chapter explains it in the more descriptive 1D case. Every step can be followed in fig. 2.10.

At first the lineouts of the raw interference image (fig. 2.10 "raw data/reference") can be described by

$$I(z) = I_0(z) + m(z) \cdot \cos(\varphi(z)) + \psi(z). \tag{2.116}$$

with a background offset $I_0(z)$, information inside the interference fringes $m(z)\cos(\varphi(z))$, and high frequency noise $\psi(z)$. The intensity profile is transformed using a Fast Fourier Transformation (FFT) (respectively 2DFFT, fig. 2.10 "acFFT data/reference") to obtain the desired frequency spectrum:

$$\mathfrak{I}(\nu) = \mathfrak{I}_0(\nu) + \mathfrak{G}(\nu) + \mathfrak{G}^*(\nu) + \Psi(\nu). \tag{2.117}$$

With $\mathfrak{I}_0(\nu)$ corresponding to the Fourier transform of $I_0(z)$, $\mathfrak{G}(\nu)$ and $\mathfrak{G}^*(\nu)$ describe the signal and its complex conjugate and the high-frequency noise $\psi(z)$ corresponds to $\Psi(\nu)$. In the frequency domain, all irrelevant information can now be removed (fig. 2.10 "filtered FFT") using a Super-Gaussian as the filter function

$$\mathfrak{F}(\nu) = \exp\left(-\left(\frac{(\nu-\nu_c)^2}{\sqrt{2\sigma^2}}\right)^n\right) \tag{2.118}$$

with ν_c as the average fringe frequency and σ as the bandwidth. $\mathfrak{F}(\nu)$ must be tuned to pass the full bandwidth of $\mathfrak{G}(\nu)$ without truncating relevant information. Depending on the noise level of the data this is sometimes more or less successful since diffraction rings of dust grains can sometimes be at the same frequency as the

fringes. Since the low frequencies are much more dominant in the frequency domain an additional filter function is implemented just to deal with them:

$$\mathfrak{F}_{\text{low}}(\nu) = 1 - \exp\left(-\left(\frac{\nu}{\sqrt{\sigma_{\text{low}}^2}}\right)^{2n}\right) \tag{2.119}$$

Also, it is very important, that the negative frequencies are also deleted. Doing so analytically extends the real value signal $I(z)$ into the complex plane (i.e., forms its analytic signal) after the Inverse Fast Fourier Transformation (iFFT) (fig. 2.10 "filtered data/reference") of the filtered signal

$$\text{iFFT}(\mathfrak{F}(\nu) \cdot \mathfrak{F}_{\text{low}}(\nu) \cdot \mathfrak{I}(\nu)) \approx \text{iFFT}(\mathfrak{G}(\nu)) = g(z) \tag{2.120}$$

which is required for the arctan-based phase extraction below.

The interference pattern is now complex and the absolute local phase (fig. 2.10 "simple phase" shows only $\mathfrak{R}(iFFT(\mathfrak{G}(\nu)))$) of the signal can be calculated as

$$\varphi_{\text{local}}(z) = \arctan\left(\frac{\mathfrak{I}(g(z))}{\mathfrak{R}(g(z))}\right) \tag{2.121}$$

which should then be unwrapped to the global phase (fig. 2.10 "stacked phase") since $-\pi < \varphi_{\text{local}}(z) < \pi$ depicting a sawtooth-like function if $g(z) \sim \cos(z)$. But technically the phase keeps rising after each interference fringe, which would set the boundaries to $-\pi < \varphi_{\text{local}}(z) < N \cdot 2\pi$ with N being the number of fringes in the image.

To analyze the phase shift induced by a deformation, like plasma, a reference image without the deformation must be recorded and treated with the same algorithm described above. Using this the final phase image (fig. 2.10 "phase image") can be calculated by

$$\Phi(z) = \varphi_{\text{deformed}}(z) - \varphi_{\text{reference}}(z). \tag{2.122}$$

giving only the change the plasma has introduced into the phase.

2.10.2 Interference and Forking Fringes

The interference images shown in fig. 2.10 are not real measurements. To simulate an interference pattern between two beams, the polarized electric fields $E_{j,i} = A_{j,i}\, e^{-i\varphi_{j,i}}$ are required, where $j \in \{1, 2\}$ labels the different beams and i denotes either s- or p-polarization (or x-/y-polarization) of those beams (i.e., beam 1, the information beam, has polarization s and p, and beam 2, the reference beam, also

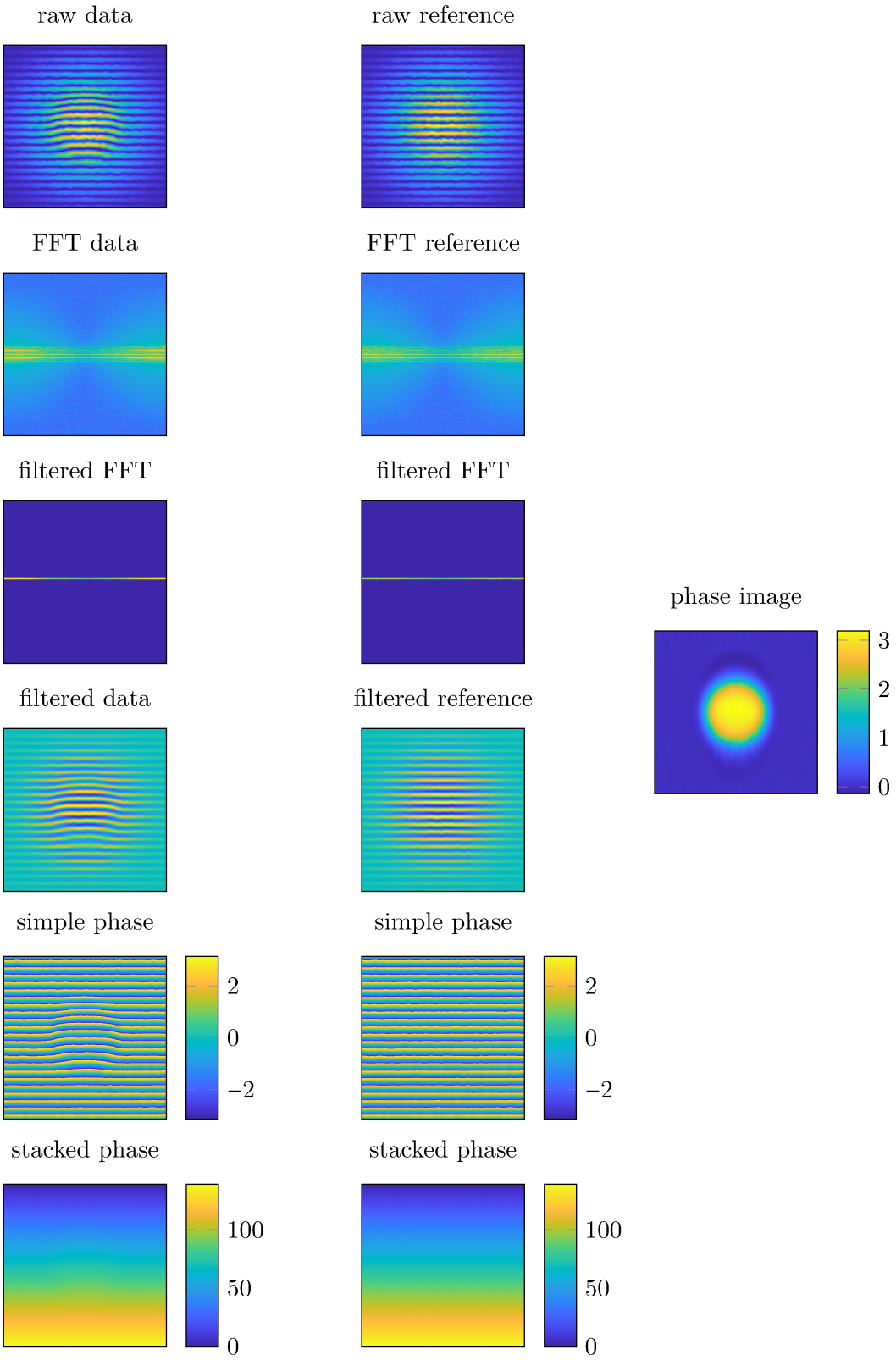


Figure 2.10: Exemplary reconstruction of a phase image from an interference image

has polarization s and p). Both the amplitude $A_{j,i}(\vec{r})$ and phase $\varphi_{j,i}(\vec{r})$ are in general functions of position.

It is assumed that the two beams have finite extent and homogeneous intensity, and overlap at an arbitrary angle. Their wavefront deformations are constant along their propagation direction. As an example, a 2D wavefront with a super-Gaussian deformation (fig. 2.11) is used, spanning the x, y plane with the shape

$$\varphi_{j,i}(x,y) = \varphi_{j,i,0} \cdot \exp\left\{-\left[\frac{(x-x_0)^2}{2\sigma_x^2} + \frac{(y-y_0)^2}{2\sigma_y^2}\right]^n\right\} \tag{2.123}$$

where the order n controls the steepness of the deformation and φ_0 its peak height. fig. 2.11 shows an example with $n = 10$. This deformation is here applied only to one of the two beams, the other one keeps flat wavefronts. The relative angle α between the two beams is introduced as an additional linear phase tilt on top of the wavefront deformation,

$$\varphi_{j,i}(x,y,\alpha_j) = \varphi_{j,i}(x,y) + \frac{2\pi}{\lambda}\, y \sin(\alpha_j), \tag{2.124}$$

with α_1, α_2 chosen such that $\alpha = \alpha_1 - \alpha_2$ is the angle between the two beams.

The resulting interference pattern on the CCD follows directly from the standard two-beam interference formula $I = |E_1 + E_2|^2$, applied separately to each polarization component (s and p beams do not interfere with each other and their intensities simply add):

$$I(x,y) = \sum_{i\in\{p,s\}} A_{1,i}^2(x,y) + A_{2,i}^2(x,y) + 2A_{1,i}(x,y)A_{2,i}(x,y) \cdot \ldots \\ \cdot \cos\big(\varphi_{1,i}(x,y) - \varphi_{2,i}(x,y,\alpha)\big), \tag{2.125}$$

where one beam is taken with a plane wavefront incident at angle α. The amplitude distributions $A_{j,i}(x,y)$ can be chosen freely to represent any spatial intensity profile.

Figure 2.11 illustrates this for deformed wavefronts and their corresponding interference patterns. The left column shows idealized deformed wavefronts: the upper with a Gaussian profile, the lower with a Super-Gaussian profile. Yellow regions (positive phase) indicate a forward-shifted wavefront that arrives earlier than the nominal plane wavefront.

The middle column shows the interference patterns resulting from these wavefronts combined with a plane reference wave incident at $\alpha = 10°$. Since the reference

beam originates from the top, forward-shifted wavefront regions displace the interference fringes upward, while negatively shifted regions displace them downward.

The right column shows the wavefronts reconstructed with the algorithm from section 2.10.1. The upper row, with a smooth deformation, is reconstructed accurately. The lower row shows stripe artifacts emerging from forking fringes near the bottom of the circular deformed region, caused by the sharp edge of the underlying Super-Gaussian profile.

This effect happens, if the slope of the wavefront has a bigger angle than the tilted wavefront of the reference beam, i.e., here the image is tilted in y direction, therefore if

$$\arctan\left(\frac{\lambda}{2\pi}\cdot\frac{\partial\varphi(x,y)}{\partial y}\right) > \alpha, \tag{2.126}$$

the total phase (deformation plus carrier tilt) is no longer monotonic in y, thus the local fringe frequency reverses sign, so the same fringe order is encountered twice. This creates an island in the interference pattern, which cannot be evaluated any more and creates the stripe in the reconstructed image.

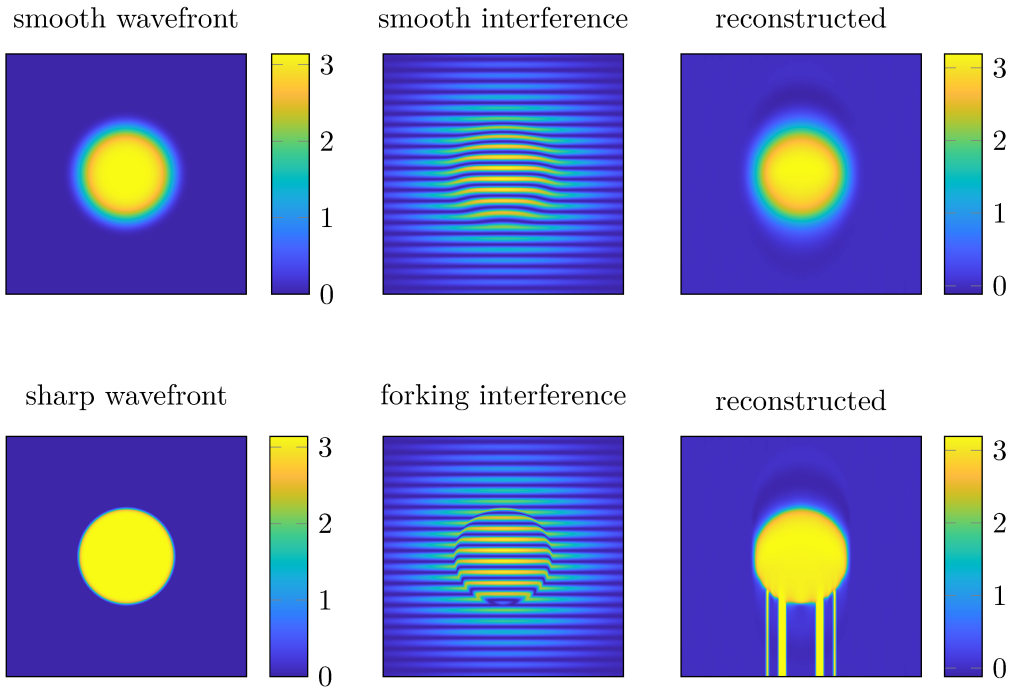


Figure 2.11: Left: Ideally deformed wavefronts. The upper one has a Gaussian shape, and the lower one a Super-Gaussian shape. Yellow areas depict a forward-shifted wavefront (arrives earlier), the color bar is scaled unit-less in [rad]. Middle: Interference pattern produced by those wavefronts at an 10° angle. The reference beam comes from the top. Forward-shifted wavefronts cause fringe distortion upwards, while a negative shift would shift fringes downwards. Right: Reconstructed wavefronts using the algorithm in section 2.10.1. The upper images display smooth deformations, while the bottom ones show how sharp wavefront edges create forking fringes, as seen at the circle's bottom. Reconstruction fails for the sharp edges but works for the smooth deformation.

Chapter 3

Experiment

In this chapter the experimental setup, as well as some collected data is presented. The experiment consists of two main components, the laser system and the pump-probe setup, which analyzes the plasma, ignited on the targets.

3.1 Laser System

The PHASER (Phase-stabilized Heine Laser) is the laser system of the Institute of Laser and Plasma-Physics (ILPP) of the research group of Prof. Dr. G. Pretzler. It is installed at the Heinrich Heine University in Düsseldorf.

The first component is a seed-oscillator, which generates the pulses. These pulses pass through a multi-pass amplifier, a hollow fibre and at the end a mirror compressor, which can lead to pulse lengths $\tau < 7\,\mathrm{fs}$. The precise mode of operation is explained on the following pages.

The pulses originate from the Ti:Sa oscillator (FEMTOSOURCE rainbow [54]). The Resonator is a Ti:Sa crystal, which is pumped by a frequency doubled ND:YAG laser with a power of 4.35 W. The resulting "spectral width" (total width, not gaussian width) of 340 nm allows bandwidth-limited pulses (eq. (2.14)) with a pulse duration down to 5 fs. Due to their repetition rate of 75 MHz the average pulse power is >400 mW. After the cavity of the laser, two glass wedges are used to stabilize the Carrier Envelope Phase (CEP) by a downstream CEP module [55] with a so-called feed-forward scheme. This early CEP stabilization is necessary if the amplified pulse is also supposed to be CEP-stabilized.

After the oscillator, the pulses are chirped (section 2.1.6) to a pulse length of $\tau = 10 - 20\,\mathrm{ps}$ by a glass stretcher consisting of two prisms. This reduces the intensity of each pulse enough to prevent damage to the amplifier components. After the amplifier unit the pulse is then compressed back to its shortest pulse

length, given by the Fourier limit. This process is called chirped-pulse amplification (CPA) [56]. After the stretcher, the pulse enters the multi-pass amplifier [57]. The Ti:Sa crystal is traversed ten times by the pulse while being pumped by an neodymium-doped yttrium lithium fluoride (ND:YLF) laser (wavelengths 527 nm and 1053 nm; pulse length of 15 ns) with 34.5 W at a 1 kHz repetition rate. The first four passes of the seed laser through the amplifier crystal have the original frequency of 75 kHz. Before the fifth pass a Pockels-cell is used to cut the frequency down to 1044 Hz. These pulses pass a Acousto-Optic Programmable Dispersive Filter (AOPDF) (Type: Dazzler, [58]) made of a paratellurite crystal. A piezo-element excites phonones to compensate for dispersion ($D_2 - D_4$, eq. (2.27)), optimize the spectrum to prevent gain narrowing and may also induce pre-pulses if necessary. After the Dazzler, the pulse passes through the amplifier crystal four more times, before being expanded and collimated. The expanded pulse is focused into the Ti:Sa crystal two more times to obtain a better spatial profile. After these ten passes, the laser is expanded to its final width to avoid self focusing and other nonlinear effects that could damage the optics. When spontaneous emission in the amplifier crystal occurs, it produces a continuous wave laser underlying the laser pulses. This lasers amplified spontaneous emission (ASE) was measured using an Sequoia (see appendix B) [59] to be less than nine orders of magnitude of the laser pulses, thus inside one Pockels cell pass, the ASE only contains less then 1% of the lasers energy.

The subsequent grating compressor compresses the pulse length down again to compensate for the chirp induced before the amplification process, as mentioned previously. The grating compressor adjusts the pulses dispersion for the hollow fiber and lowers the pulse length to around 20 fs.

To achieve the final spectrum a hollow fiber is filled with neon [60]. Inside the 1.5 m fiber spectral broadening due to self-phase-modulation is induced. The incoming pulse energy and D_i have to be selected carefully as the parameters of the final pulse are highly dependent on them as the ionization processes are highly non linear. For all measurements presented in this work a pressure of $p = 1$ bar was used yielding a spectral width $\Delta\lambda > 200$ nm.The small radius of the hollow fibre of about 150 µm has the advantage of being an additional spatial filter which leads to a very clean Gaussian profile.

After the fiber the mechanical parts for pulse selection are mounted. Those are a chopper wheel, that reduces the frequency of the laser to 100 Hz and a Shutter which allows to select single pulses. A combination of glass plates and wedges with anti reflection coatings adds the necessary amount of D_2 so the compressor mirrors are able to compress the pulse to an effective pulse length of $\tau \approx 6.1\,\text{fs} \pm 0.3\,\text{fs}$ at a Fourier-limit of $\tau \approx 5$ fs (the Fourier-limit can not be reached due to a not completely

compensated spectral phase profile). The final energy inside the chamber will be up to 60% of the energy behind the fibre. Therefore the laser pulses at the experiment have a single pulse energy of $\sim 0.5\,\mathrm{mJ}$.

3.2 Beam Profile

The beam profile inside the chamber is analyzed with a 10x microscope objective and a charge-coupled device (CCD) camera. The imaging optics have been calibrated with a micrometer plate to 13.4 µm/px. In fig. 3.1 images of the beam in the focal plane are presented. For the perfect case a Gaussian width of $w_0 = 2.39\,\mu\mathrm{m}$ can be measured across both dimensions. The most astigmatic focus that measurements have been made with has the two semi axis of the ellipsoid at Gaussian widths of $w_{0a} = 2.46\,\mu\mathrm{m}$ and $w_{ba} = 1.99\,\mu\mathrm{m}$.

3.3 Targets

The experimental setup demands targets with highly precise surface properties, characterized by surface roughness of less than 10 nm to ensure a detailed phase resolution. These targets were selected based on their different material properties, mainly their conductivity, to investigate their effect on the development of the phase images.

3.3.1 Fused Silica Target Coated with Gold

The base material used was Fused Silica (FS), a form of silicon dioxide SiO_2, which was sputtered with a 60 nm thick gold coating. The accuracy of the sputtering machine is estimated to produce targets with up to 50% thicker layers than programmed. This thickness was chosen, since it can be assumed that more than 7 atomic layers exhibit the solid-state properties of a material. Also it is thin enough that possible 2D electron movements in the material may be measurable. According to Multi-fs, plasma in the first 1 ps penetrates the target in the order of magnitude of $\sim 100\,\mathrm{nm}$, and plasma $t > 1\,\mathrm{ps}$ does reach a depth $> 1\,\mu\mathrm{m}$. Therefore it can be assumed that in the first 1 ps the plasma contains predominantly gold ions.

The gold coating enhances the reflectivity and conductivity of the fused silica substrate, making it suitable for high accuracy optical experiments.

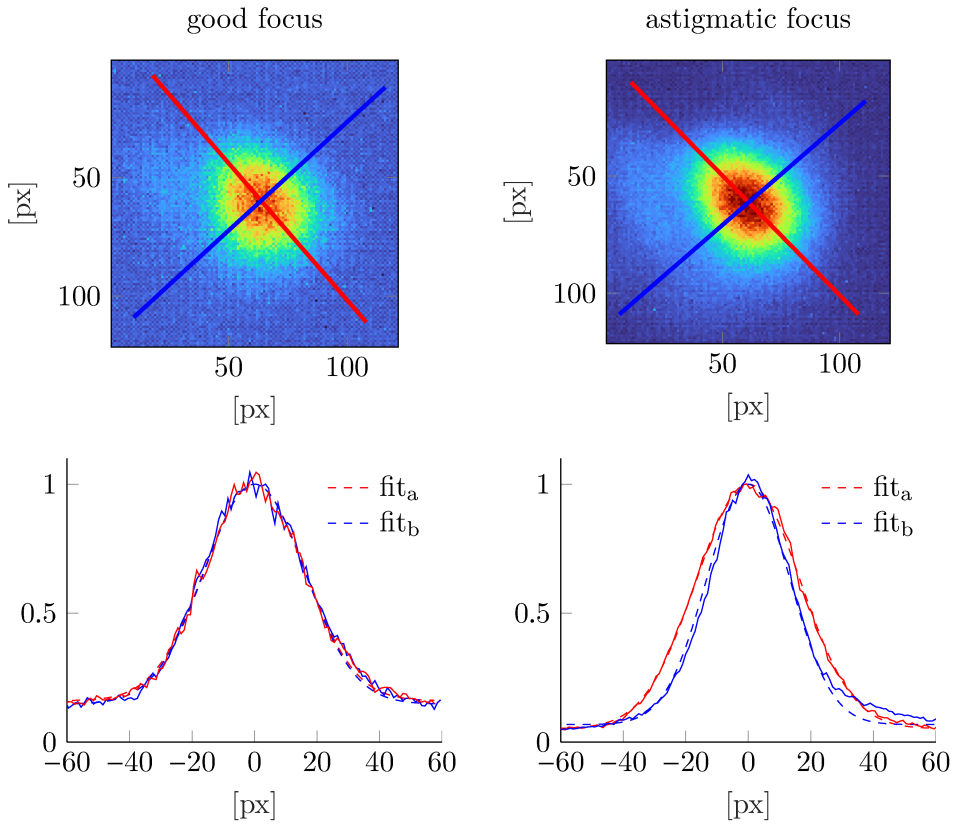


Figure 3.1: Beam profile in the focal plane. Left top: a perfectly adjusted Gaussian focus. Left bottom: the respective lineouts of the semi-major and minor axis of the ellipsoid with their Gaussian fits. The Gaussian width are equal $w_{0a} = w_{0b} = 32\,\text{px} = 2.39\,\mu\text{m}$. Top right: focus with a slight astigmatism. Right bottom: the respective lineouts of the semi-major and minor axis of the ellipsoid with their Gaussian fits. The Gaussian widths are $w_{0a} = 33\,\text{px} = 2.46\,\mu\text{m}$ and $w_{ba} = 26.6\,\text{px} = 1.99\,\mu\text{m}$.

Density	$2.2\,\mathrm{g/cm^3}$
Resistivity	$\approx 1 \times 10^{18}\,\Omega\,\mathrm{m}$
Thermal Conductivity	$1.38\,\mathrm{W/Km}$
Refractive Index	1.46
Reflectance	Less than 4%

Table 3.1: Material properties of Fused Silica at room temperature, λ = 800 nm, angle of incidence 15° [61]

Density	$19.32\,\mathrm{g/cm^3}$
Resistivity	$\approx 2.2 \times 10^{-8}\,\Omega\,\mathrm{m}$
Thermal Conductivity	$317\,\mathrm{W/Km}$
Refractive Index	0.13254 + i5.0418
Reflectance	Over 98%

Table 3.2: Material properties of gold coating at room temperature, λ = 800 nm, angle of incidence 15° [62]

3.3.2 Carbon Target

Glassy Carbon, a crystalline form of carbon, was chosen as the second target due to its unique combination of thermal, electrical, and optical properties. While it has a high electrical resistivity compared to gold and copper, it still has a sufficient reflectivity allowing adequate contrast of the interference fringes on the CCD. Additionally its naturally high surface flatness allows precise phase measurements over a big area.

Density	$1.42\,\mathrm{g/cm^3}$
Resistivity	$\approx 4.5 \times 10^{-3}\,\Omega\,\mathrm{m}$
Thermal Conductivity	$6.3\,\mathrm{W/Km}$
Refractive Index	≈2.8 + i1.6
Reflectance	≈ 30%

Table 3.3: Material Properties of Glassy Carbon at room temperature, λ = 800 nm, angle of incidence 15° [63]

3.3.3 Copper Target

Copper, as a mid Z metal with high conductivity, is available as a bulk target with high surface flatness. This offers the advantage that these measurements can be compared with those of the gold - Fused Silica (Au-FS) target, as surface effects due to possible currents flowing in the thin gold layer can now be investigated more accurately. A bulk gold target would be ideal for a better comparison with the

Au-FS target, but this was not feasible due to the surface flatness requirements in conjunction with the material costs.

Density	$8.935\,\mathrm{g/cm^3}$
Resistivity	$\approx 1.68 \times 10^{-8}\,\Omega\,\mathrm{m}$
Thermal Conductivity	401 W/Km
Refractive Index	0.25352 + i5.0131
Reflectance	Over 96%

Table 3.4: Material Properties of Glassy Carbon at room temperature, $\lambda = 800\,\mathrm{nm}$, angle of incidence 15° [64]

3.3.4 Surface Accuracy and Preparation

All targets were prepared with surface roughness less than 10 nm, ensuring near-perfect surfaces. This high precision minimizes scattering effects and ensures accurate experimental results. The surfaces were polished and verified using atomic force microscopy (AFM) and interferometric techniques. It should also be noted here that surfaces whose roughness exceeds these values are essentially unusable for the presented experiment, since the wavefront distortion of the reference beam would distort the interferometric image too much for it to be possible to analyze it.

3.4 Pump-Probe

The pump-probe experiment was performed in an octagonal vacuum chamber with a working area of approximately $1\,\mathrm{m}^2$. The beam path is sketched in fig. 3.2. The pump beam travels all the time in the plane parallel to the floor. A small portion of the laser was cut off from the edge of the beam ($M_{1,\mathrm{probe}}$) to be used as the probe beam and reflected upwards.

The pump beam was reflected twice by 90° before being focused onto the target with a parabola of 127 mm. The target could be moved freely through the focus, which enabled a so-called z-scan to be performed. The average intensity can be estimated by

$$I(z) = \frac{E_{\mathrm{pulse}}}{\pi \cdot w(z)^2 * \tau}. \tag{3.1}$$

With an pulse duration of $\tau 6\,\mathrm{fs}$, a pulse energy of $E_{\mathrm{pulse}} = 0.5\,\mathrm{mJ}$ and a Gaussian

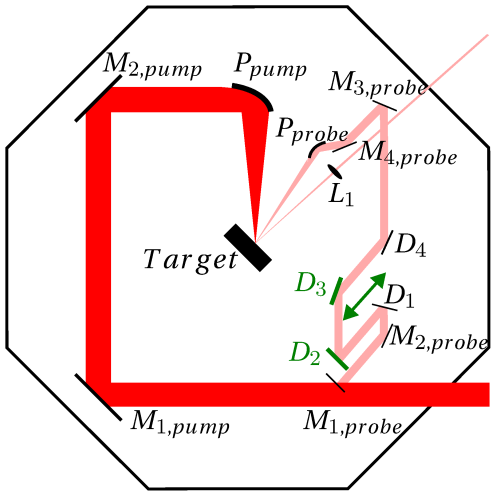


Figure 3.2: Mirror configuration inside the chamber. $M_{i,\text{pump}}$ reflect the pump beam until the pump-parabola P_{pump} focuses it into the target, while the mirrors $M_{i,\text{probe}}$ reflect the probe beam until it is focused by the probe parabola P_{probe} onto the target. The D_i mirrors are part of the delay stage, while the green ones are movable to enable different optical path lengths. After reflection on the target, the probe beam is collimated by the lens L_1.

width

$$w(z) = w_0 \cdot \sqrt{1 + \left(\frac{\lambda z}{\pi w_0^2}\right)^2} \tag{3.2}$$

calculated from the focal width $w_0 = 4\frac{f\lambda}{\pi D}$ with $\lambda = 790\,\text{nm}$, the focal length $f = 125\,\text{mm}$ and the beam width $D = 54\,\text{mm}$. This gives a first order approximation in table 3.5.

The probe beam then traveled parallel to the floor and is reflected downward into the delay stage. The mirrors marked in green could move up and down to adjust the time delay of the probe beam relative to the pump beam. The delay stage could move a total of 90 mm, where the timing overlap spanned 70 mm (i.e., the positions where the probe pulse hits the target after the pump pulse), resulting in a path length extension of 140 mm, which corresponds to 467 ps. After several reflections in the upper level, the laser was reflected downward at 23° to the normal of the floor.

The pulse was then focused to a point a few millimeters in front of the target by a 90° axis-shifted parabola with $f = 152.4\,\text{mm}$ and $D = 25.4\,\text{mm}$, resulting in an angle of incidence to the target normal of 23° (in the plane perpendicular to the pump-

z [µm]	$w(z)$ [µm]	I_0 $\left[\frac{\mathrm{W}}{\mathrm{cm}^2}\right]$	I_e $\left[\frac{\mathrm{W}}{\mathrm{cm}^2}\right]$	I_{FWHM} $\left[\frac{\mathrm{W}}{\mathrm{cm}^2}\right]$
0	2.37	1.65e18	4.26e17	9.63e17
20	3.18	9.13e17	2.37e17	5.34e17
40	4.86	3.91e17	1.01e17	2.29e17
60	6.79	2.00e17	5.19e16	1.17e17
80	8.81	1.19e17	3.08e16	6.96e16
100	10.9	7.82e16	2.03e16	4.57e16
120	13.0	5.51e16	1.43e16	3.22e16
140	15.1	4.08e16	1.06e16	2.39e16
160	17.1	3.15e16	8.15e15	1.84e16
180	19.3	2.50e16	6.46e15	1.46e16
200	21.4	2.03e16	5.25e15	1.19e16

Table 3.5: Distance from focus z, Gaussian width of focus $w(z)$, and intensities I_0, I_e, and I_{FWHM}.

beam plane). The spot size on target was chosen large enough to fully illuminate the plasma with additional surrounding area available as a reference region. While a spot size of approximately 200 µm ($\sim 2 \times d_{\mathrm{plasma}}$) would in principle suffice, a spot larger than 600 µm was used instead to minimize the intensity gradient across the illuminated area caused by clipping of the beam profile. Since the interference intensity scales with E^2, such a gradient makes one side of the spot noticeably darker than the other. Since the CCD's fixed dynamic range must then accommodate both extremes simultaneously, the bright side tends to saturation before the fringes on the dark side reach sufficient exposure. A larger illumination profile keeps the intensity more uniform across the region of interest, so that fringe contrast is well resolved everywhere without saturating any part of the image.

Both probe beam and pump beam were overlapped on the target, with the target in the focal plane of the pump beam. If plasma is ignited before the probe beam arrives, it carries the corresponding information in its deformed wavefronts. After the probe beam had interacted with the plasma, dispersion of the probe pulse was no longer a concern, wherefore it could be collimated by an $f = 150\,\mathrm{mm}$, $d = 25.4\,\mathrm{mm}$ lens and left the vacuum chamber through a glass window.

In air, the pulse passed a polarization filter to minimize scattered light from the pump beam.

3.4.1 Interferometer Alignment

The beam was then focused into a Mach-Zehnder-type interferometer (fig. 3.3) by an $f = 300\,\mathrm{mm}$, $d = 25.4\,\mathrm{mm}$ lens, where it was first split by a beam splitter. In

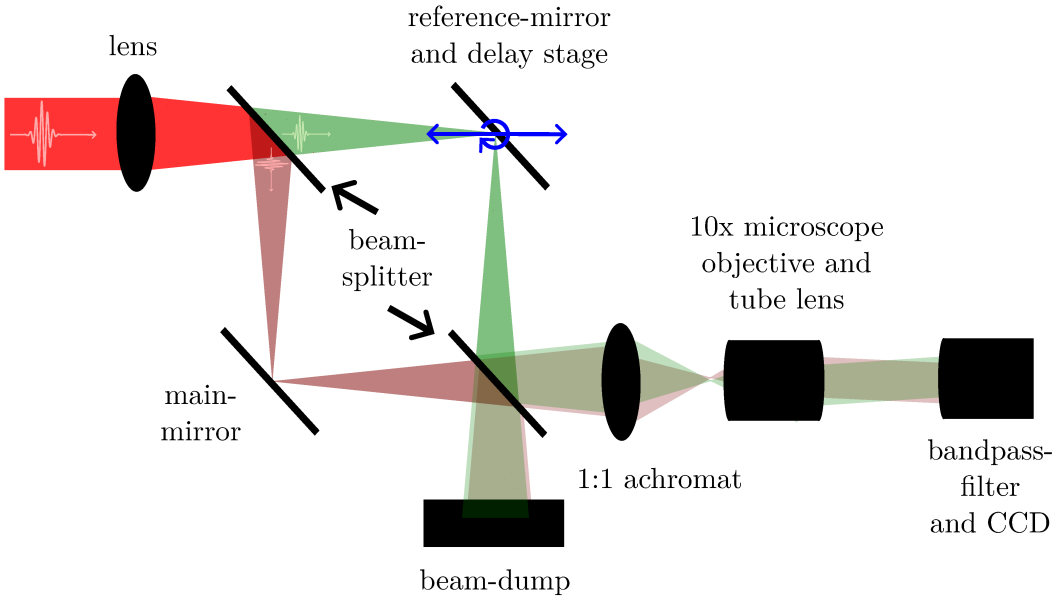


Figure 3.3: Mach Zehnder Interferometer. Not to scale. Dark red represents the main beam path with the information of the plasma. Dark green represents the reference beam path which transports the plane wavefronts. The achromat has a 1:1 ratio, for display purposes the imaging distances are distorted.

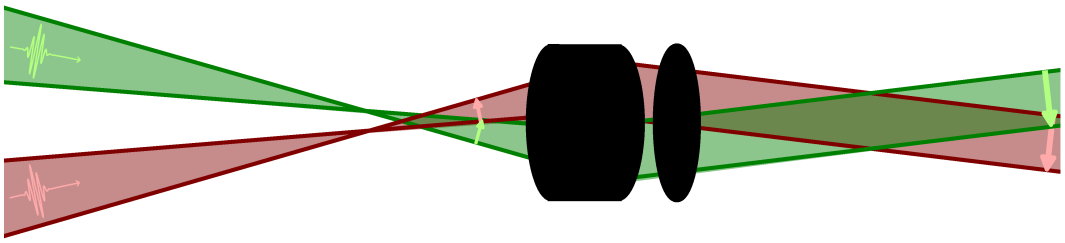


Figure 3.4: Simplified top down view of the beam path through microscope objective and tube lens, after the 1:1 achromatic lens. Angles and widths not to scale. The lens system is considered as one part for simplification. The reference beam in green comes from the left and crosses the main beam (red) which contains the information which will later be analyzed. The images of the target and plasma (green and red arrow) are located shortly after the focal point of the probe beam. After the imaging optics the beam direction is flipped and strongly magnified. If the wavefronts inside the main image are deformed, they will be tilted towards the reference image if they have dents to the back (come later) or away from the reference image if they have dents to the front (come earlier).

the main arm, the target where the plasma is ignited was imaged onto the main mirror. The position of the mirror in the reference arm was adjusted for temporal overlap and for optimized fringe spacing. Having a sharp image of the plasma on the main mirror had the advantage that the fringe density could be adjusted by tilting the mirror without losing focus on the CCD later in the imaging apparatus. However the position of the temporal overlap would also change then, which leads to an alternating adjustment process. After the mirrors, the beams were recombined by a second beam splitter. The overlapped images were spatially offset from one another, so that the deformed wavefronts of the main beam interfered with the plane wavefronts from the undisturbed "side" of the reference beam image (fig. 3.5).

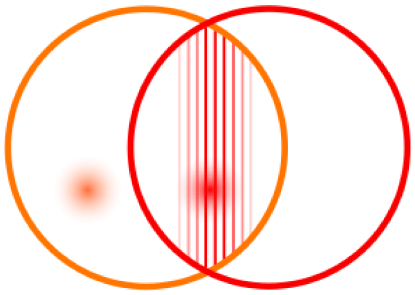


Figure 3.5: The main probe pulse (red) and the reference pulse (orange) are overlapped, so that the undistorted area of the reference pulse can interfere with the distorted area of the main pulse.

Since the sharp image of the plasma was located on the mirror, and therefore diverging behind the interferometer, a further imaging apparatus was needed to project the mirror plane (i.e., the plane of the plasma image) onto the CCD. As a magnified image was desired, a short working distance for the microscope objective was required. Since the objective could not be placed close enough to the mirror directly, a 1:1 achromatic lens ($f = 50\,\mathrm{mm}$, $d = 25.4\,\mathrm{mm}$) first projected the image to a more accessible plane behind the interferometer. From there, an infinity-corrected 10x microscope objective with a working distance of $d_w = 16\,\mathrm{mm}$ and a numerical aperture of 0.3, together with an $f = 20\,\mathrm{cm}$, $d = 25.4\,\mathrm{mm}$ tube lens, imaged the plasma onto the CCD. Additionally, a 790 nm bandpass filter with a FWHM of 10 nm was mounted in front of the CCD to stretch the pulse length to at least 92 fs by exploiting the Fourier limit (2.14), and to block stray light.

3.4.2 Resolution

The theoretical NA of the imaging apparatus, assuming perfect alignment of the probe beam, is limited by the following elements:

- the first lens ($f = 150\,\mathrm{mm}$, collimating the beam from the target at $z_1 = 150\,\mathrm{mm}$) has NA = 0.0847
- the second lens ($f = 300\,\mathrm{mm}$, focusing the collimated beam onto the interferometer mirror) has NA = 0.0423

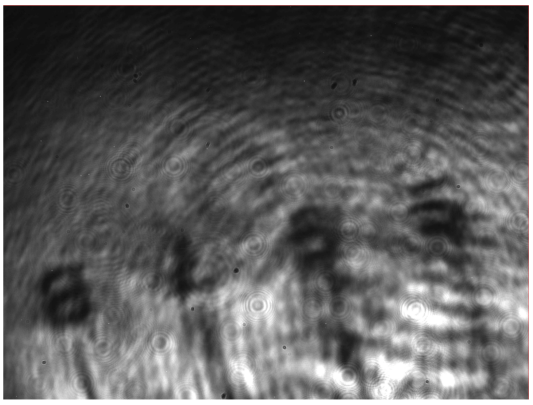


Figure 3.6: Calibration of imaging apparatus with micrometer-plate. The thin 10 µm lines are not clearly visible.

- the 1:1 achromat has an illuminated radius $r = 4.23\,\text{mm}$, well within its aperture radius of 12.7 mm, so it does not further limit the NA
- the microscope objective is rated NA = 0.3 and the tube lens has NA = 0.0635, neither of which is limiting

The system is therefore limited by the second lens, giving an overall theoretical NA ≤ 0.0423, corresponding to an optimal resolution of $a_{\text{res}} = 11.5\,\mu\text{m}$.

Fig. 3.6 shows a calibration image of a micrometer plate with thick lines every 100 µm and thin lines every 10 µm. The thick lines and accompanying numbers are resolved, while the thin lines cannot be resolved, consistent with their 10 µm spacing lying below the theoretical resolution limit of $a_{\text{res}} = 11.5\,\mu\text{m}$.

3.4.3 Fringe-Direction Discussion

At the CCD the reference beam comes from the right. Therefore, the following correlation holds: If the wavefronts are distorted to the front then the interference fringes are shifted to the right. If the wavefronts are delayed, the interference fringes are shifted to the left.

The first experiments conducted on the Au-FS target produced fringe shifts to the right, indicating wavefronts that are distorted forward, either accelerated in the plasma or reflected earlier than the reference, as shown in fig. 3.7. This figure presents a top-down view of the interference plane at the CCD camera. The wavefronts of the main arm in the interferometer are pictured in red, while the plane wavefronts of the reference arm are colored in green. The dashed line marks the location of the CCD camera, i.e. the image plane, and the teal dots show the location of the interference fringes. In a) two identical plane wave fronts overlap,

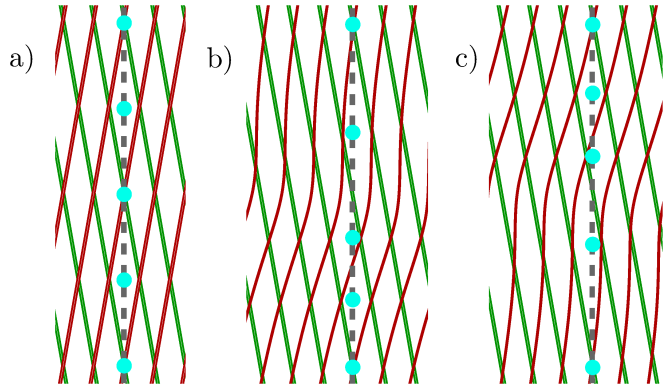


Figure 3.7: Top down view of the simplified wavefronts of the reference beam (green) and the main beam (red) propagating to the right towards the CCD (dashed grey) from fig 3.4. a) plane wavefronts. Evenly spaced interference fringes (teal, lines on CCD perpendicular to the screen). b) wavefronts of main beam distorted to the front. Interference fringes shift to the bottom. c) Wavefronts distorted to the back. Interference fringes shift to the top.

producing an evenly spaced interference pattern. In b) the red wave fronts are distorted to the front, thereby shifting the fringes toward the bottom, i.e. the right. In c) the wavefronts are shifted towards the back, aka are coming later in time, which shifts the fringes towards the top, i.e. the left. At this point shall be noted, that the plasma in all upcoming phase images distorts the wavefronts to the front, i.e. the distortion arrives earlier. If there seem to be inconsistencies with the signs, those would result from the use of different algorithms. All interference images show the same direction of distortion.

3.4.4 Complications and Things to Consider

To create the desired accuracy in space, time and phase, while also being able to adjust the relevant parameters accordingly, this type of interferometer is very fragile and the current setup needs much maintenance. Thereby some of the not so obvious complications shall be explained in this chapter.

One crucial complication that could seem obvious in hindsight, but may not be as obvious for a first time builder of this setup. It is possible to create the effect of measuring both positive and negative phase shifts for the same plasma at different days (i.e., executions of the experiment).

The first step in setting up the interferometer is to image the plasma, i.e., the target surface, onto the CCD, thereby directly imaging the wavefront distortion occurring at the position of the plasma onto the camera. Doing so would give the most accurate result. If one would assume that a slight variation from this

imaging plane would only cause the wavefront deformation to decrease, until the wave would be flat again at $\Phi = 0$, one would be wrong. In fact it is possible to flip the distortion of the wavefront from front to back, if the imaging plane is set up wrongly enough. Thus the fringes in the interference image would shift from one side to the other, i.e. if the correct setup would shift them to the left, a wrong setup may shift them to the right, not only giving the wrong strength of the shift but even a wrong sign as seen in fig. 3.9. How this may happen is lined out in fig. 3.8. If looking at the upper image, and one imagines a plasma bubble (red bubble on gold target) distorting the wavefront (black lines) to the front. Then a imaging plane (teal dashed line) in front of the target (c) sees the wavefronts distorted to the front. But since wavefronts always propagate perpendicular to its surface if we take the image behind the target (a), the wavefronts appear to be distorted to the back. And at position (b) a weird state of neither bend forward nor backwards exists, which is also distinct in the interference image since we see the fringes fork there (fig. 3.9 middle image). Thereby all those interference images in fig. 3.9 can be simply created by sliding one lens back and forth, thereby moving the imaging plane. Now one could hope that moving the imaging plane forward and optimizing for the highest fringe distortion would ensure the correct measurements. But unfortunately the plasma does not necessarily has to create a bubble. It is also technically possible that it creates a hole, which would distort the wavefronts to the back. And unfortunately as seen in fig. 3.8 in the lower sketch, this would create exactly the same pattern, with backwards distorted wavefronts when the imaging plane is moved back, forward distorted wavefronts when the lens is moved forwards and forking fringes in the middle. Thereby it is not possible to tell with certainty if the plasma is actually distorting the wave to the front or to the back, just be looking at the interference images. A feasible solution to solve this problem is to create a sharp image of a surface on the CCD while blocking the reference arm in the interferometer and taking a picture of the target. Using a micrometer plate allowed to firstly solve the problem of identifying the imaging plane, but also calibrates the spatial resolution ($1\,\mu m \approx 10\,px$) (fig. 3.6).

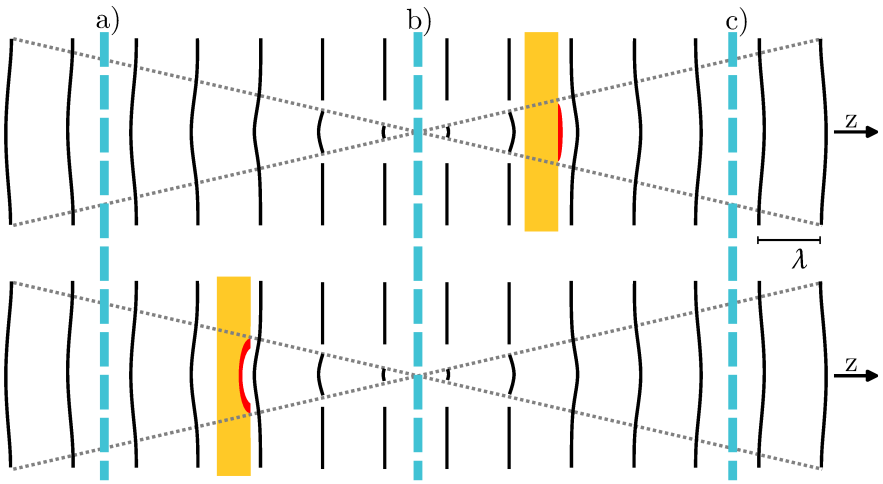


Figure 3.8: Propagation of plane wavefronts upon reflection (black) in the area around a plasma. Direction of propagation along z-axis. Top: Reflection upon expanded plasma (red) and plane solid (gold) deforming the wavefronts to the front. Image plane at position a): Wavefronts seem to be distorted to the back; c): they seem distorted to the front. Bottom: Indented plasma distorts wavefronts to the back. Image plane at position a:) Wavefronts seem deformed towards the back; c): Wavefronts seem distorted to the front. Interference patterns of image plane at a), b) and c) are shown in fig. 3.9. Coherence of reflected light decreases with distance to actual target.

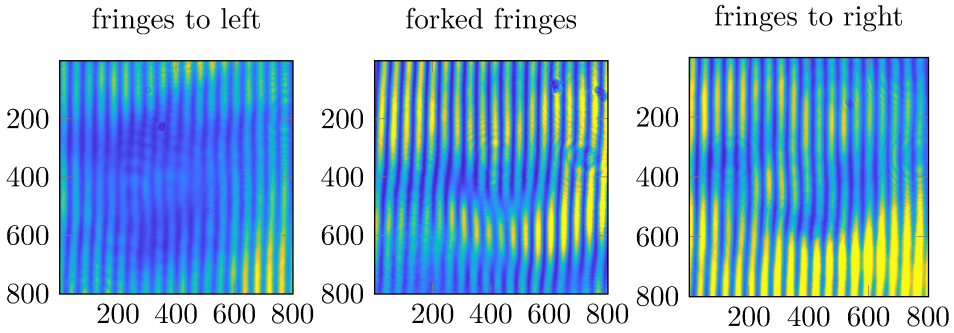


Figure 3.9: Interference fringes measured at comparable plasma. Position of first lens in fig. 3.3 was changed resulting in different image positions on the z-axis. Left: Fringes tilt to the left, therefore, the wavefronts lag behind. Image taken at a position at the left side in fig. 3.8. Middle: forking fringes. Image taken at a position similar to the middle of fig. 3.8 where neither forward nor backwards tilted wavefronts exists. Right: fringes to the right. The wavefronts are distorted to the front. Image taken at a position at the right side of fig. 3.8. From only the interference fringes it can't be told, if the plasma was a hole or a bubble.

3.5 Craters

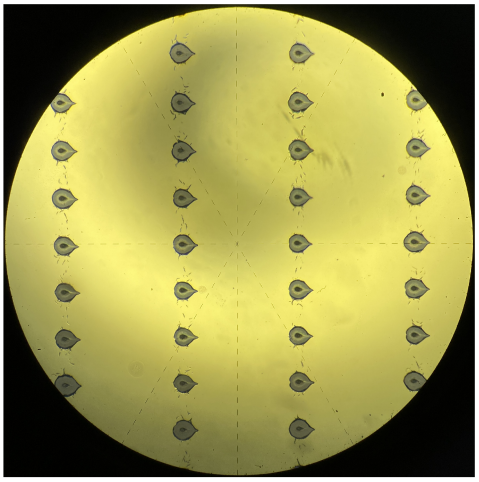


Figure 3.10: Craters on Au-FS target.

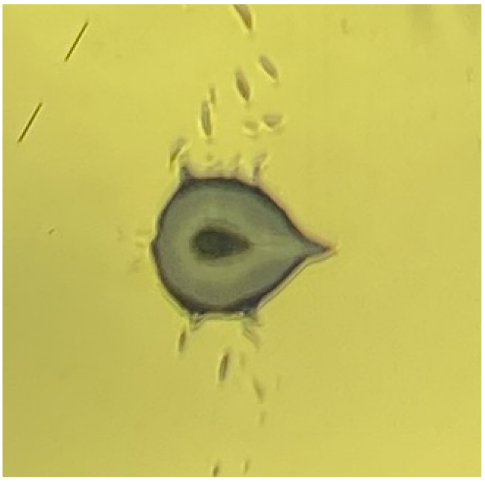


Figure 3.11: Closeup of Au-FS Crater

Post-experimental analysis of the targets shows the formation of craters which will be shortly analyzed in this chapter. Fig. 3.10 depicts the craters on the Au-FS target, with the 500 µm horizontal and 300 µm vertical spacing between each shot, which were the same parameters for all targets. Fig. 3.11 shows a close-up of such a single crater. This teardrop-shape contains two regions of interest. Firstly, the crater itself is the smaller and darker dot in the middle, whose diameter is shown in 3.6. There the maximum diameter is given in x- and y-direction. Secondly, the "corona" around the crater is the brighter area around it, which does not have the same significant depth of a few micrometers as the crater, instead just consists of surface perturbations in the nanometer regime. This corona exists in this work only for the Au-FS and Cu target, but not for the evaluated carbon measurement. Other measurements on carbon targets (see fig. C.1) did also have a similar corona around the crater, hence the missing corona is not a special property of carbon. It rather seems like a day dependent laser property, like for example a particularly big ASE with a different divergence. For the Au-FS and Cu-targets the diameters are measured to the tip of the "nose" pointing towards the right/top (see fig. 3.11/ fig. 3.14). In the Au-FS case it is also worth noting, that inside the corona, the 60 nm gold layer is completely evaporated and only the Fused Silica substrate below is visible. Thus the reflectivity in this area is highly reduced. Also only the crater itself extends deep inside the Fused Silica bulk.

Analyzing the corona with AFM, fig. 3.12 shows that its depth is not significantly lower than that of the surrounding, unperturbed surface. The shallower

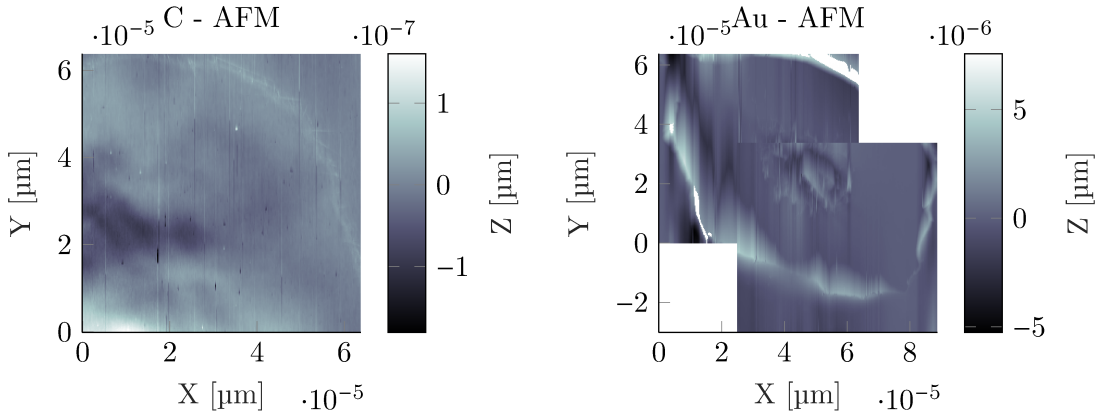


Figure 3.12: AFM image of corona around carbon (not used for phase measurement) and Au-FS craters. Au image stitched from two images and rotated −135°.

depths of the crater itself cannot be analyzed correctly, since they exceed the maximum detectable depth of the used microscope. Noted shall be that the outer edge of the Au-FS corona is clearly raised. This appears by a very small amount at some Carbon targets (given that the corona is present), but there it is only a thin line is visible compared to the relatively big amount at the Au-FS target. It is assumed that this is due to the fact that the "Au-foil" curves upwards at the edge.

Target	Crater		Corona	
	$\varnothing_X$ [µm]	$\varnothing_Y$ [µm]	$\varnothing_X$ [µm]	$\varnothing_Y$ [µm]
Cu	15	17	45	85
C	14	20	-	-
Au on FS	20	28	77	100

Table 3.6: Crater and Corona diameters for Cu, C and Au-FS

To give a better understanding about the depth of the central craters, z-scans were performed under a confocal microscope. The Leica SP8 [65] was provided by the Center for Advanced Imaging (CAi) at the HHU and operated with help of Dr. Sebastian H"ansch. The images were captured with a central wavelength of the laser at $\lambda = 488\,\text{nm}$, a resolution of $704\,\text{px} \times 704\,\text{px}$ with $\Delta x = \Delta y = 0.206\,\mu\text{m/px}$ and a z-resolution of $\Delta z = 0.1001\,\mu\text{m/px}$ with about 200 steps, depending on the crater depth.

Figure 3.13 shows in the top row two example images of craters from the Copper target, one with the target at the highest z position and one at the lowest z position. Taking all the pictures in between those two gives a 3D matrix with the reflected intensities of each x-y image depending on the z position of the target. The bottom

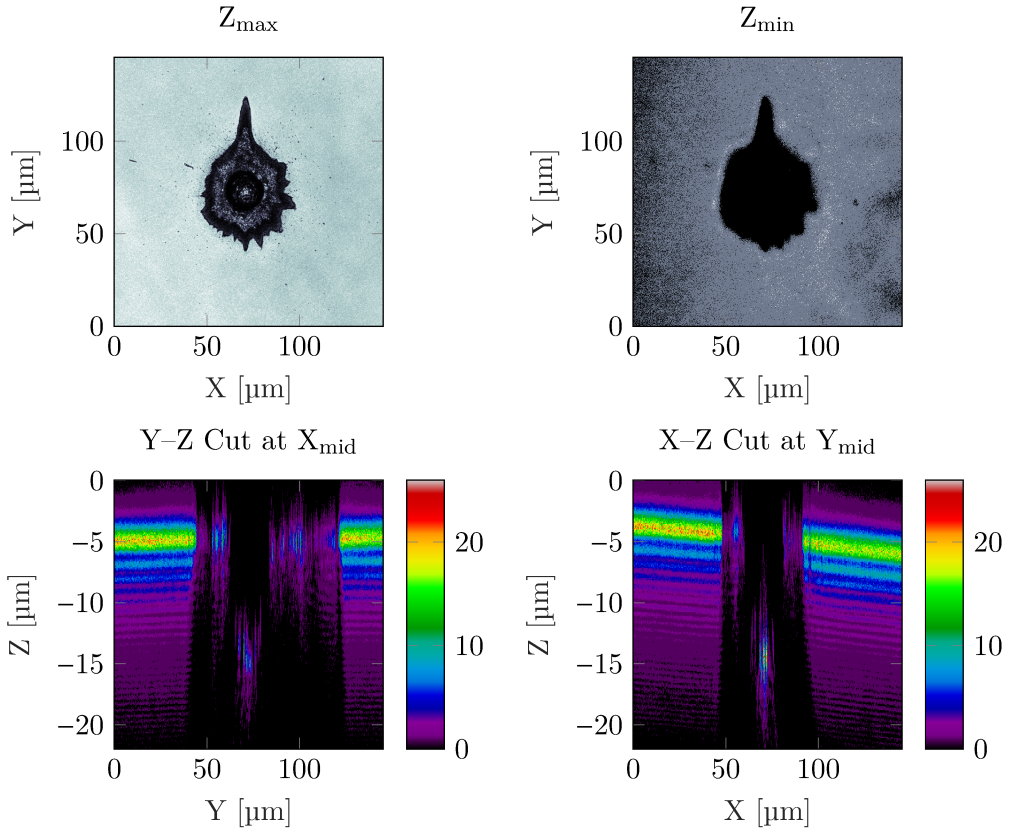


Figure 3.13: Top row: Highest and lowest false-color image of Cu-Crater from Z-stack. Bottom Row: Cutouts from Z-stack along X and Y axis through the middle of the respective other. Intensities also in false colors, with a different palette for optimized visibility of characteristics.

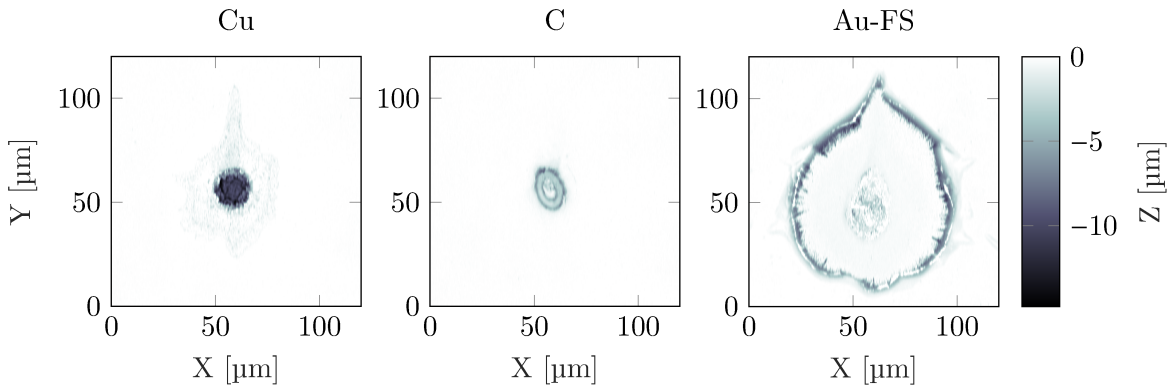


Figure 3.14: Surface plots of all craters of the used materials.

row shows two cutouts from this z-stack one along the center of the x-axis and one along the center of the y-axis. In the Y-Z cut the plain surface around the crater reflects optimal at about $Z \approx -5\,\mu m$. It can also be seen, that the surface is also slightly tilted. Inside the crater the strongest reflection can be seen at about $Z \approx -15\,\mu m$, which suggests a crater depth of around $d \approx 10\,\mu m$. The x-z cut shows a similar pattern, and it is even more prevalent, that the surface was tilted during measurement.

To better analyze such a stack, "surface" plots are created (see fig. 3.14) by taking the position of highest reflection along the z-axis for each X-Y point. Those images have again to be taken with caution, since this position of highest reflection does not have to be necessarily at the position, where the crater depth is reached, but can also occur at a position, where the curved crater walls create an unpredictable caustic effect (similar to the reflections inside a coffee cup). Nevertheless, those images still can give additional information, especially about the corona.

While the crater depth of the copper target seems to measure about $d_{Cu} \approx 12\,\mu m$, the carbon crater depth reaches about $d_C \approx 5\,\mu m$. The crater inside the fused silica substrate on the other hand does not seem to get measured correctly, which aligns with the expectation that the very low reflectivity of fused silica will result in the worst performance. The flat surface of the corona on the other hand seems to be consistent with the previous observations of the AFM (fig. 3.12).

Chapter 4

Simulation

In order to estimate the physical parameters and gain a more comprehensive understanding of the effects that cannot be measured directly, various simulations were carried out with the aim of fully predicting the experimental results, given by the setup outlined in the previous chapter.

To this end, the Multi-fs code [66] first simulates the predicted plasma shape and expansion. Then, a special ray tracing algorithm calculates the effect of the plasma bubbles on an incident electric field, how they are reflected, and what effects this has on the phase of the field (i.e., the wavefront deformation). In addition, ray tracing is used to predict error bars due to laser instabilities. The modified wavefronts are then passed through the imaging device, which is simulated according to Rayleigh-Sommerfeld diffraction theory. These results can then be compared later with the actual experimental results, while at the same time evaluating the effectiveness of the experimental setup for this and other similar studies.

4.1 Multi-fs

The Multi-fs code [66] simulates the 1D-hydrodynamic expansion of a plasma after energy has been injected by an ultra-short laser pulse, accounting for material-specific parameters such as ionization state, energy potentials, thermal flux, radiation, and the equation of state (EOS). While many hydrodynamic codes exist to simulate the expansion, cooling, and shock-wave transmission of a laser-heated plasma, most are designed for laser-plasma interaction times in the nanosecond range, assuming quasi-continuous energy deposition. Multi-fs instead resolves the plasma parameters during and immediately after an ultrashort-pulse interaction, which is essential here some of the electron-ion equilibration and hydrodynamic response timescales relevant to this work occur on the same order as the pulse du-

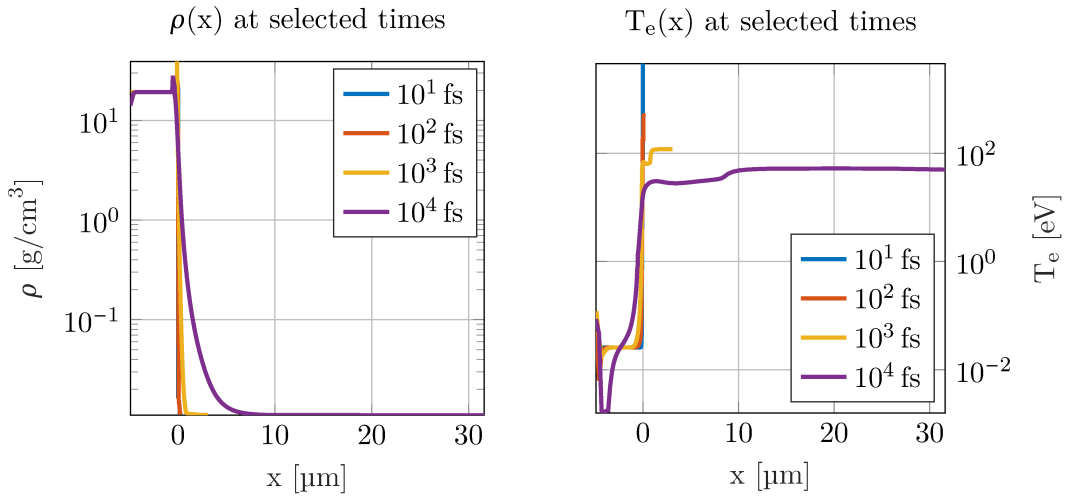


Figure 4.1: Density lineouts and electron temperature lineouts from Multi-fs-simulation of expanding Au laser-plasma from a solid state target (left side at $x < 0$)at different time points.

ration itself. A ns-code usually assumes full LTE or fixed absorption profiles, which do not hold true on low fs time scales. (See appendix E for further information about the implementation.)

For all simulations presented here, the Drude-Sommerfeld model [67] is used to describe the optical response of the plasma, with a p-polarized pulse incident at $\alpha_i = 45°$. A mathematically Gaussian pulse shape has the characteristic of never reaching true zero, which leads to annoying artifacts in a numerical simulation. Therefore the pulse envelope is modeled by $P_0 \cdot \sin(t/\mathcal{T})^2$ (with $P(t < 0) = 0$ and $P(t > 2\mathcal{T}) = 0$), where $\mathcal{T} \approx 2.5\tau$ matches the Gaussian width ($\tau = \mathrm{FWHM}/(2\sqrt{\ln 2})$). A 7 fs FWHM Gaussian therefore corresponds to $\mathcal{T} = 10\,\mathrm{fs}$ for the $\sin^2$ pulse, with an equal peak intensity $P_0 \approx 8.6 \times 10^{17}\,\mathrm{W/cm^2}$.

The ionization states are calculated using a Saha solver similar to that of Zaghloul [46], implemented by Riedlinger [47] and the FLYCHK code [37], depending on applicability. Opacity maps are difficult to compute at high densities, where bound-bound and bound-free transition frequencies (i.e., the relevant Einstein coefficients) must be resolved individually [68–72], while low-density plasma is instead dominated by free-free and scattering interactions. Those are used to calculate how the plasma absorbs and emits radiation as a function of frequency, and are required to solve the radiative transport equations inside the plasma. A fully first-principles calculation is therefore not currently feasible. Nevertheless, an approximation is made, as experimental data for absorption spectra in solids [73] are available, which are dominated by bound-bound interactions. Therefore, the temperature-

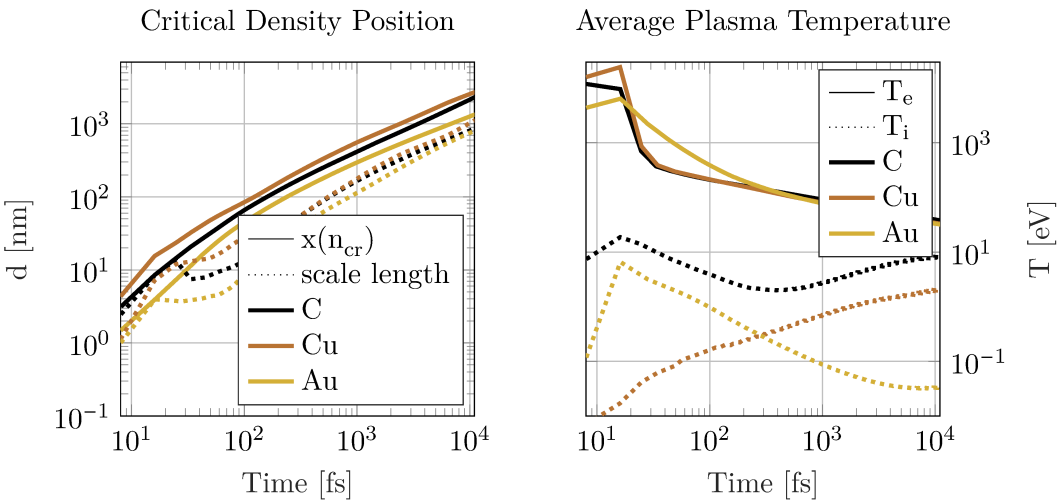


Figure 4.2: Position of critical density and scale length of the plasma and average temperature in front of the critical density

and density-dependent Rosseland-opacity

$$\kappa_k^R = \frac{\int_{\nu_{k-1}}^{\nu_k} \frac{\partial I^P}{\partial T} \mathrm{d}\nu}{\int_{\nu_{k-1}}^{\nu_k} \frac{\partial I^P}{\kappa \partial T} \mathrm{d}\nu} \tag{4.1}$$

which governs diffusive radiative heat transport where the plasma is optically thick, and the Planck-opacity

$$\kappa_k^P = \frac{\int_{\nu_{k-1}}^{\nu_k} \kappa I^P \mathrm{d}\nu}{\int_{\nu_{k-1}}^{\nu_k} I^P \mathrm{d}\nu}, \tag{4.2}$$

which governs the emission/absorption in optically thin regions, are calculated. Here k denotes the group for each frequency spectrum from ν_{k-1} to ν_k, where the Planck spectrum

$$I^P = \frac{\nu^3}{e^{\nu/T} - 1} \tag{4.3}$$

and its temperature derivative

$$\frac{\partial I^P}{\partial T} = \frac{e^{\nu/T} \cdot \nu^4}{(e^{\nu/T} - 1)^2 \cdot T^2} \tag{4.4}$$

are evaluated. Constants are neglected as they reduce to 1 since both κ^R and κ^P are normalized.

The simulations are analyzed for carbon (parameters for glassy-carbon parameters, see table 3.3 [63]), copper, and gold as targets. Examples of lineouts from a simulation with the gold target are shown in fig. 4.1, with the laser incident on the

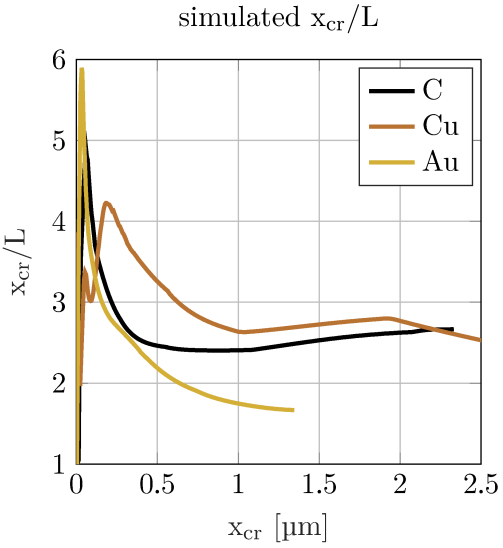


Figure 4.3: Ratio between critical density position x_{cr} and scale length L, reaching an approximately constant value of about 2.5 for carbon and copper, while constantly decreasing for gold.

solid target ($x \leq 0$) from the right. The plasma density displays an almost exponential profile (in the area of relevant density) with the scale length increasing in time, and a short bump of increased density visible below $x < 0$ shows a shock wave propagating into the solid. Very important for this work is the fact, that the entire expanded plasma has roughly the same temperature at each position in front of the critical density, with $T_e(x > x_{cr}, t)$ only depending on the time (fig. 4.1, right), at least within the same order of magnitude. Since this is the area, in which a beam of light would be reflected, locally uniform temperature is a reasonable assumption.

Using this data, the movement of the critical-density position and the evolution of the plasma scale length are analyzed (fig. 4.2, left). Near the critical density, the electron density profile is well approximated by an exponential decay,

$$n_e(x) \approx n_{cr} \cdot e^{-(x-x_{cr})/L}, \tag{4.5}$$

where x_{cr} is the position of the critical density n_{cr} ($\lambda = 800\,\mathrm{nm}$) and L is the scale length, i.e., the distance over which the density falls to $1/e$ of n_{cr}. Both the position of the critical density x_{cr} and the scale length L grow over similar orders of magnitude, from $\approx 1\,\mathrm{nm}$ to $10\,\mathrm{nm}$ at $t = 10\,\mathrm{fs}$ to $\approx 1\,\mu\mathrm{m}$ to $10\,\mu\mathrm{m}$ at $t = 10\,\mathrm{ps}$, increasing roughly linearly. As can be seen in fig. 4.3 the scale length remains a small factor larger than the critical density position throughout, as would be expected for exponential decay.

The simulation is also used to approximate the plasma shape, i.e., the position of the critical density, in time and space. Therefore, it is assumed that the intensity profile of the laser pulse at the focus is Gaussian, with a width ofh $\sigma_{\text{pulse}} = 2.37\,\mu\text{m}$ and peak intensity $I_0 \approx 8.6{\times}10^{17}\,\text{W/cm}^2$. Fig. 4.4 shows the superimposed intensity and plasma profiles, along with the plasma height and width at different intensities. The simulation is performed in 1D, thus the lateral expansion due to the intensity gradient is neglected. For plasma sizes below the plasma width, this approximation is plausible, towards the end of the simulation, when $x_{\text{cr}} \approx \sigma_{\text{plasma}}/2$ this assumption starts to fall apart. It can be seen that a difference between 100% and 40% laser-solid energy-coupling creates a ratio in plasma height of $\frac{1.76\,\mu\text{m}}{2.36\,\mu\text{m}} = 75\%$ after 11 ps. The plasma width, given here by the fit of a Super-Gaussian

$$G(x) = Ae^{-\left(\frac{x^2}{2\sigma^2}\right)^p} + B \tag{4.6}$$

onto the plasma shape has for the relevant intensities a width of $\sigma_{\text{plasma}} \approx 3.8\,\mu\text{m}$ with the order $p \approx 1.36$ for all fits. Different shapes (Gaussian, half-sphere) have been evaluated but were significantly outperformed by the Super-Gaussian wherefore the slight inconvenience of an additional parameter is accepted.

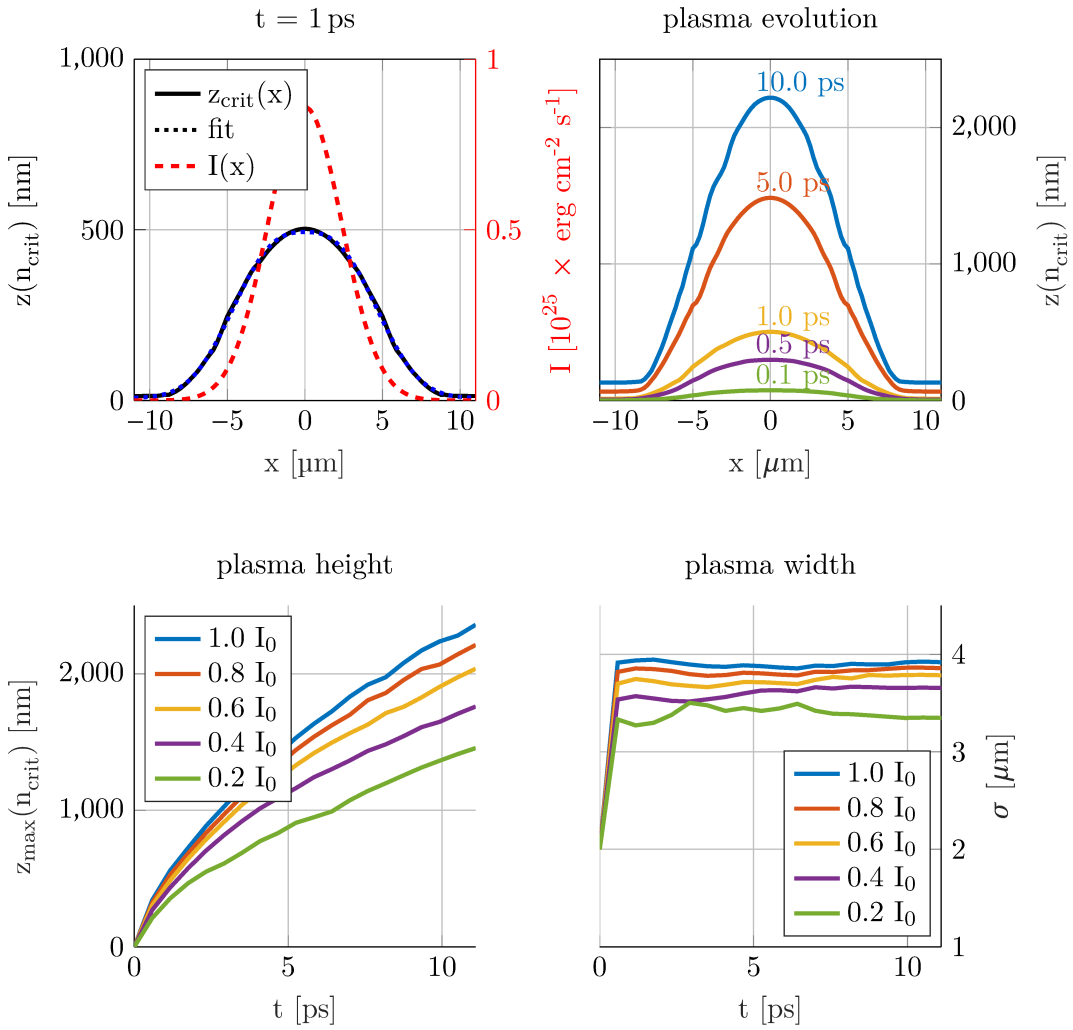


Figure 4.4: 2D-plasma-shape of copper plasma simulated with 1D-Multi-fs expansion with pulse intensity $I_0 = 8.6 \times 10^{17}$ W/cm^2.

4.2 Phase-Correct Ray Tracing Algorithm

This section presents a comprehensive approach to the phase-correct ray tracing algorithm written for this work, enabling the accurate determination of phase and polarization changes in a laser beam undergoing multiple reflections. While a single reflection is straightforward to compute, sequential reflections in a three-dimensional space however are quite hard to calculate, especially on skewed or non-planar surfaces. The reflected beam can easily become elliptically polarized and propagate along non-trivial axes. The algorithm described here overcomes these challenges, offering precise calculations of both spatial and temporal errors (due to errors in pulse travel distance), phase effects (due to material and plasma properties), as well as the resulting polarization properties.

4.2.1 Ray and Surface Definitions

A starting ray is characterized by its position $\vec{r_P}$, electric field $\vec{E}$ (complex, containing phase according to eq. (2.84)), direction vector $\vec{e}_k$, wavelength λ, and intensity I[1]. For simulations involving complex beams, rays can be sampled from the spatial and temporal distribution as needed.

Surfaces are described by their normal vector $\vec{n}$, position $\vec{r_S}$, and material properties, including density ρ, magnetic permeability μ, and wavelength-dependent complex refractive index $n = n_0 + ik$. For curved surfaces, such as parabolic reflectors, the normal vector $\vec{n}$ is computed individually for each incident ray to maintain the accuracy of the ray sampling rate. This is necessary to ensure the correct phase/polarization response of each ray reflected on a complex shape.

4.2.2 Reflection Calculation

The algorithm relies on the Fresnel equations (section 2.7) to calculate the properties of reflected rays. The reflected electric field $\vec{E}_r$ is derived from the incident field components $\vec{E}_{p,i}$ and $\vec{E}_{s,i}$, and the reflection coefficients r_p and r_s are computed for p- and s-polarized light, respectively.

After determining the direction and electric field components of the reflected ray, the temporal and spatial properties of the beam are updated. Changes in the phase and amplitude of the electric field are also taken into account. After

[1] In the code, a "ray" is named "photon". This is not understood as a real photon with quantum mechanical properties, but rather as a struct that contains information about a beam with fixed extension. Therefore, the term "intensity" is used here to represent the change in intensity of a group of photons in this beam, for example by reflection or transmission.

reflection, the beam propagates through vacuum or any material, with its time[2], space ($\vec{r}_p, \vec{e}_k$), and phase being updated accordingly.

The accuracy of the simulation was verified by comparison with real experiments. For this purpose, reflections at different configurations of silver mirrors were analyzed. Linearly polarized light with a polarization angle of 45° to the ground was reflected at a silver mirror and its polarization was then analyzed. Figure 4.5 shows a sketch of the configurations with the final $\Delta\phi = \varphi_p - \varphi_s$, where fig. 4.6 shows the identical configuration in the simulation.

The first configuration shows how the direction of linear polarization changes from 45° to −45° upon almost perpendicular reflection, due to the fact that the p-polarized light has to have a phase shift of $\varphi_p - \varphi_s = \pi$ just because of geometrical considerations. This can also be seen in the theory in fig. 2.8. The next test shows how the light is almost perfectly circularly polarized just upon one reflection at an angle of $\alpha_1 \approx 77.4°$, where $\varphi_p - \varphi_s = \frac{\pi}{2}$. The circularity of the polarized light can be analyzed by a lambda-quarter-plate. This only works well, because the reflectivity of s- and p-polarized light (s-pol/p-pol) is almost exactly identical for silver. The ratio of s- to p-pol can be varied by rotating the initial polarizer by the required angle. The next two test involve adding a second mirror, again at the same angle α_1 which is supposed to shift the phase further for $\Delta\phi = \frac{\pi}{2}$ and thereby changing the circular polarization back to linear polarization. The total phase shift of $\Delta\phi = \pi$ thereby flips the direction of the polarization from 45° to −45°.

It shall be noted that there are no geometrical effects present which flip the phase positive or negative, depending on if the reflection is left or right hand, as long as the polarization is always perceived from the rays direction of travel. This means 20° right and 20° left does yield the identical final polarization as 20° right and 20° right.

4.2.3 Error Analysis

Since temporal resolution is one of the most important features of this work, every aspect that could affect it needs to be considered. In particular, spatial jitter of the beam can also introduce a temporal jitter between pump and probe pulses. This arises because a small angular jitter, present before the probe beamis clipped, passes differently through the pump and probe arms. Since each arm contains a distinct sequence of periscope reflections, sometimes not 90° angles and off-axis parabolas, the same initial perturbation produces a different change in path length (i.e., a different arrival time) in each arm. Even tho it is not assumed, that the mirrors in

[2]time cannot simply be expressed by phase, since a pulse can change its CEP due to phase shifts upon reflection, while its position in time stays unaffected.

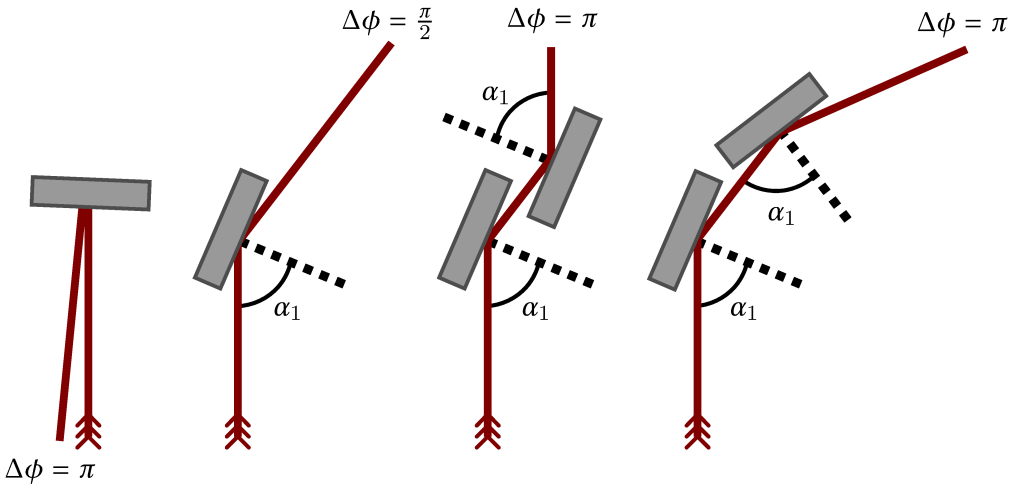


Figure 4.5: Sketch of experiment of HeNe reflection on silver mirrors. Initial laser is linearly polarized with $E_p = E_s$ and $\Delta\phi = \varphi_p - \varphi_s = 0$ initially. α_1 depicts the angle where the relative phase shift between p and s-polarized light is $\Delta\phi = \frac{\pi}{2}$.

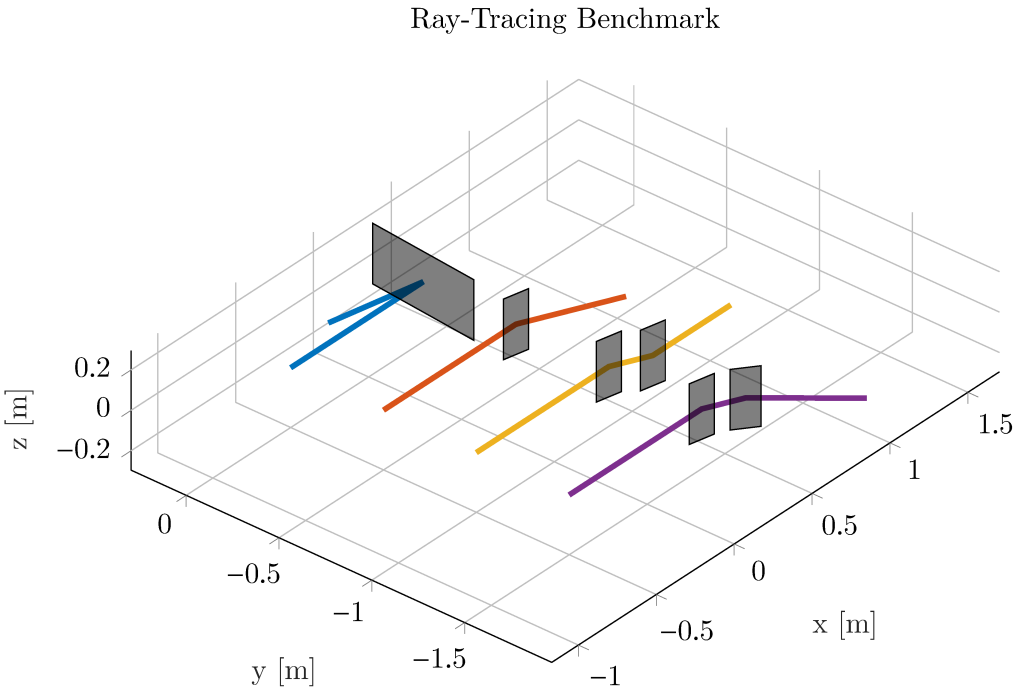


Figure 4.6: Benchmark 1: Ray-Tracing of experiment as displayed in fig. 4.5

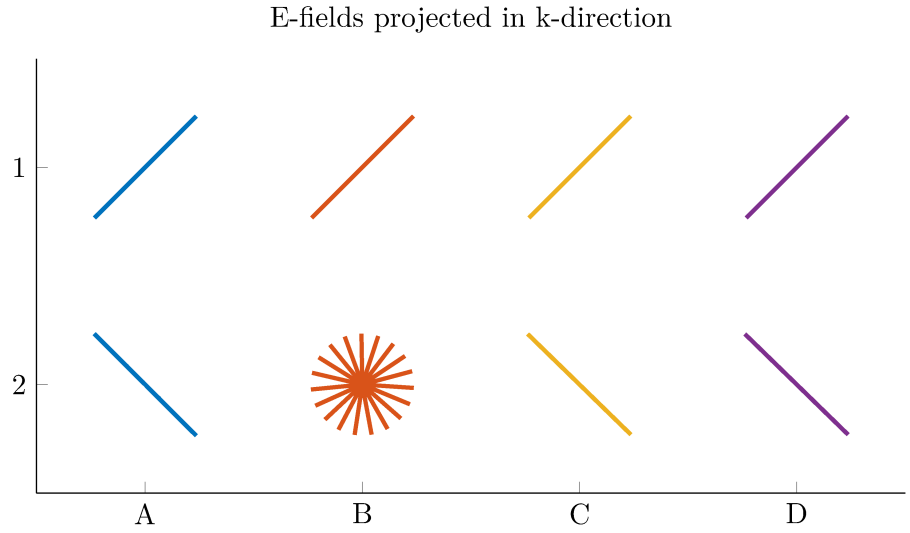


Figure 4.7: Benchmark 2: Electric fields direction of oscillation as seen from the direction of propagation (k-vector) relative to the ground. Upper row shows incoming electric field, which is identical for each beam in fig. 4.6. The bottom row shows the outgoing electric field. It can be seen that beam A, C, and D have rotated the polarization by 90°, while B has circularly polarized light.

both arms itself are jittering, due to the non orthogonal reflections, the resulting path length difference cannot be estimated by a simple geometric projection of the input jitter.

Therefore, the algorithm was used to calculate the mirror positions of the experimental chamber, and then the beam parameters (vectors $\vec{r}_{\text{input}}$ and $\vec{k}_{\text{input}}$) were varied to reproduce the spatial jitter visible in the experimental data. In this way, the temporal delay between two rays (i.e., beams) taking different paths can be easily calculated, which can be used to correct the absolute time of a pump-probe image according to its spatial position.

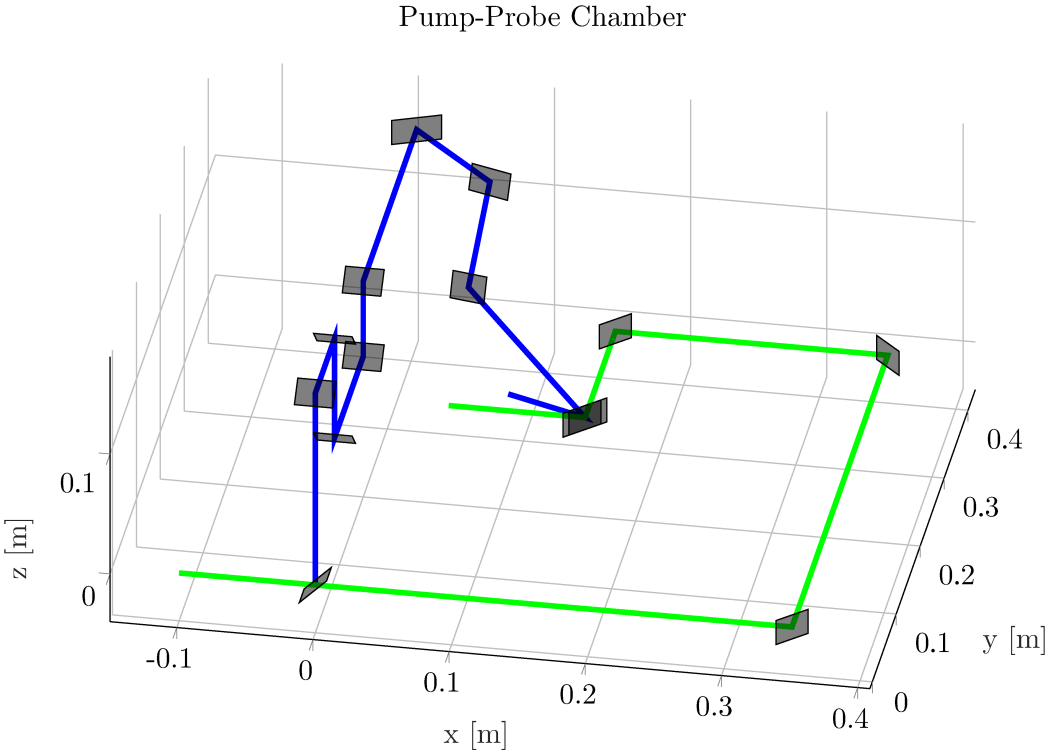


Figure 4.8: Raytracing of pump and probe beam in the vacuum chamber. The green pump beam is reflected by 2 mirrors and one parabola before intersecting with the blue probe beam on the target. The probe beam takes a different path (blue path, 8 flat mirrors, and a parabolic mirror at the end) where a delay stage is present (mirror 3, 4, 5 and 6 of the blue ray path) and is also focused by a parabola onto the target.

4.2.4 Ray Tracing in Electron Density Distributions

As established in section 2.6, the refractive index of a plasma depends on its electron density distribution. For any freely expanding plasma, this density profile decays approximately exponentially into free space, producing a corresponding gradient in the refractive index.

When a ray propagates through a medium with a locally varying refractive index, this gradient curves its path, like the mechanism responsible for the bending of radio waves in the earth's upper atmosphere. Since a plasma density gradient produces an analogous refractive-index gradient, a similar curving effect occurs for a light ray propagating through the plasma.

While a laser-solid plasma typically expands into a bubble-like shape, this section instead assumes an infinitely wide 1D gradient, comparable to a plasma mirror, where the transverse extent of the plasma is much larger than the depth of the plasma. This assumption is reasonable for sufficiently small and dense plasmas, and allows the effects of the gradient itself to be understood and quantified in isolation, without the added complexity of the plasma's transverse geometry.

As already established, since $n < 1$ for plasma, propagation inside will create a shift in the CEP of a pulse. Also the ray will follow a curved path through the plasma, creating a GH-shift like effect. The refractive index distribution is, as seen in eq. (2.70), a function of the electron density and the collision frequency, the latter is also dependent on the plasma temperature. The final goal will be to create a quantitative value/function which allows to calculate the perceived phase shift of a reflection on plasma, $\Delta\phi_{\text{plasma}} \sim s(T, L, \alpha)$ depending on the plasma temperature T, scale length L and angle of incidence α.

4.2.4.1 Plasma Modeling

To model the density and temperature profile multiple approaches can be taken. Most simply the distribution given by a simulation (like the Multi-fs simulation in section 4.1 in combination with FLYCHK [37]) can be used. A posteriori analysis shows that the temperature profile is not critical, since the average temperature can be assumed to be constant in front of the critical density. The electron density on the other hand can simply be assumed to follow an exponential decay. This is a reasonable approximation applicable for most plasma parameters.

Since this work already uses the fluid-simulation to determine the position of the critical density, and it is known, that light is not able to enter behind the critical density the relevant density gradient is expressed as

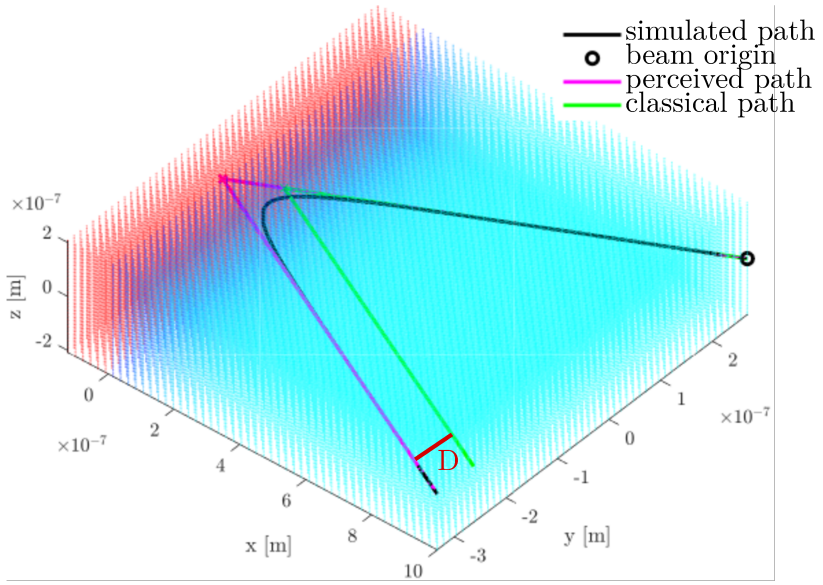


Figure 4.9: Ray tracing of a ray through a 1D plasma gradient. The scale length of the plasma $L_0 = 10 \times 10^{-8}$ m, at angle of incidence $\alpha = 15°$, towards the critical density (red area, $x < 0$). The gradient in blue denotes the electron density, with a deeper blue signifying higher density. The black line shows the simulated beam path. The magenta line displays the perceived beam path, as if it was reflected on a surface and did not curve. This point of reflection would be inside the critical density. The green line shows the path as if the beam would reflect at a surface located at the critical density, also neglecting curvature. The displacement D (see section 2.8) between the classical and the simulated path would be defined as positive in this example.

$$n_e(x) = n_{e,0} \exp\left(-\frac{x}{L}\right) \tag{4.7}$$

with the scale length L and the critical density $n_e(x = 0) = n_{e,0} = n_c$ at $x = 0$. Thereby, all optical length variations can be calculated relative to the position of the critical density position. If the position of critical density is not known, the approach in appendix G can be used.

Technically a small plasma bubble would be better approximated using

$$n_e(\vec{r}) = n_{e,0} e^{-|\vec{r}|/L}, \tag{4.8}$$

but since the scale length of the plasma is usually small compared to the size, the 1D approximation is better suited to give a clearer overview and general description of the phase shift behavior with temperature and scale length.

4.2.4.2 Ray Tracing Algorithm

Here, two different ray tracing algorithms for refractive index distributions are implemented. The first follows the idea of Montagnino [74], utilizing a Taylor-series expansion. This algorithm is faster, but will not converge correctly for low electron temperatures due to worse susceptibility to fast changes in the curvature of the ray. To update the positions $\vec{r}$ and direction $\vec{v}$ of the light

$$\vec{r}_{i+1} = \vec{r}_i + \vec{v}_i \mathrm{d}r + \vec{K}\frac{\mathrm{d}r^2}{2} + \vec{L}\frac{\mathrm{d}r^3}{6} \tag{4.9}$$

$$\vec{v}_{i+1} = \vec{v}_i + \vec{K}\mathrm{d}r + \vec{L}\frac{\mathrm{d}r^2}{2} \tag{4.10}$$

with

$$\vec{K} = \frac{1}{n}\left[\nabla n - \vec{v}(\vec{v}\cdot\nabla n)\right]$$

$$\vec{L} = \frac{1}{n}\left(\vec{v}\cdot\nabla(\nabla n) - 2\vec{K}(\vec{v}\cdot\nabla n) - \vec{v}\left[\vec{K}\cdot\nabla n + \vec{v}\cdot\vec{v}\cdot\nabla(\nabla n)\right]\right)$$

is used. To keep the code versatile the gradients of the refractive index are calculated numerically. The first order gradient is approximated using a symmetrical differential

$$\nabla n(\vec{r}) = \begin{pmatrix} \frac{n(\vec{r}+\vec{\Delta}x)-n(\vec{r}-\vec{\Delta}x)}{2\Delta x} \\ \frac{n(\vec{r}+\vec{\Delta}y)-n(\vec{r}-\vec{\Delta}y)}{2\Delta y} \\ \frac{n(\vec{r}+\vec{\Delta}z)-n(\vec{r}-\vec{\Delta}z)}{2\Delta z} \end{pmatrix}$$

where $\vec{\Delta}x = \begin{pmatrix} \mathrm{d}r \\ 0 \\ 0 \end{pmatrix}$, respectively $\vec{\Delta}y = \begin{pmatrix} 0 \\ \mathrm{d}r \\ 0 \end{pmatrix}$ and $\vec{\Delta}z = \begin{pmatrix} 0 \\ 0 \\ \mathrm{d}r \end{pmatrix}$, whereas $\Delta x = \Delta y = \Delta z = \mathrm{d}r$.
The second order gradient is also approximated symmetrically

$$\begin{aligned}\nabla(\nabla n(\vec{r})) = &\frac{n(\vec{r}+\vec{\Delta}x) - 2n(\vec{r}) + n(\vec{r}-\vec{\Delta}x)}{\Delta x^2} \\ &+ \frac{n(\vec{r}+\vec{\Delta}y) - 2n(\vec{r}) + n(\vec{r}-\vec{\Delta}y)}{\Delta y^2} \\ &+ \frac{n(\vec{r}+\vec{\Delta}z) - 2n(\vec{r}) + n(\vec{r}-\vec{\Delta}z)}{\Delta z^2}\end{aligned}$$

which provides accurate results if $\mathrm{d}r$ is chosen sufficiently small. In the presented cases $\mathrm{d}r < \lambda/10$ which leads to reasonably close results. To calculate the refrac-

tive index (2.70) is used. For a plasma large compared to the wavelength a 1D exponential approximation for the density gradient can be made.

The second implementation is a Runge-Kutta algorithm according to Sharma [75], which can be used to solve the problem for lower temperatures, for which a higher computational time is tolerated. Here the positions $\vec{r}$ and normalized direction $\vec{e}_k$ of the beam are updated with

$$\vec{r}_{i+1} = \vec{r}_i + \mathrm{d}t \left(\vec{e}_{k,i} + \frac{A + 2B}{6} \right) \tag{4.11}$$

$$\vec{e}_{k,i+1} = \vec{e}_{k,i} + \frac{A + 4B + C}{6} \tag{4.12}$$

using

$$\begin{aligned} A &= \mathrm{d}t \cdot D(\vec{r}_i) \\ B &= \mathrm{d}t \cdot D\left(\vec{r}_i + \frac{\mathrm{d}t \vec{e}_{k,i}}{2} + \frac{\mathrm{d}t A}{8} \right) \\ C &= \mathrm{d}t \cdot D\left(\vec{r}_i + \mathrm{d}t \vec{e}_{k,i} + \frac{\mathrm{d}t B}{2} \right) \end{aligned}$$

using the function

$$D(\vec{r}) = n(\vec{r}) \cdot \nabla n(\vec{r}) = \begin{pmatrix} \frac{n(\vec{r}+\vec{\Delta}x)^2 - n(\vec{r}-\vec{\Delta}x)^2}{4\Delta x} \\ \frac{n(\vec{r}+\vec{\Delta}y)^2 - n(\vec{r}-\vec{\Delta}y)^2}{4\Delta y} \\ \frac{n(\vec{r}+\vec{\Delta}z)^2 - n(\vec{r}-\vec{\Delta}z)^2}{4\Delta z} \end{pmatrix}.$$

Since this approach is wavelength independent, it is important to ensure that $\vec{e}_k(0)$ is normalized. The ray equation $\mathrm{d}\vec{r}/\mathrm{d}s(n\mathrm{d}\vec{r}/\mathrm{d}s) = \nabla n$ with the arc length s being integrated using t instead of the true arc length, needs $\vec{e}_k = n\mathrm{d}\vec{r}/\mathrm{d}s$. Thus the velocity vector carries the local refractive index. This is achieved with $||\vec{e}_k(0)|| = n(\vec{r}(0))$.

Using this approach, it is possible to calculate the difference in optical path length a photon experiences, depending on whether it reflects at the critical density with perfect vacuum in front or it travels through the plasma gradient. It can be

calculated as $d_{\text{optical}} = \int_0^{r_{\max}} n(r)\mathrm{d}r$, or numerically as

$$d_{\text{optical}} \approx \sum_{i=0}^{i_{\max}} |r_{i+1} - r_i| \cdot n(r_i). \tag{4.13}$$

Since the refractive index is calculated using (2.70) with the respective collision frequencies (2.73) that follow from the electron density, the state of ionization can be calculated using the FLYCHK code [37] and/or the Saha solver implementation by Riedlinger according to Zaghloul [46]. Therefore, the temperature and the amount of electrons are always coupled. Thus the electron density and ion density can be calculated using

$$n_e = Z(T) \cdot n_i = Z(T) \cdot \rho \tag{4.14}$$

with the temperature T dependent ionization level $Z(T)$ and the number density of the material ρ.

Figure 4.9 displays a laser beam traveling through a 1D density gradient. Using this the optical path difference (OPD) is

$$\Delta d = d_{\text{optical}} - d_{\text{straight}} \tag{4.15}$$

with $d_{\text{straight}} = |r_{0,x}/v_{0,x}| \cdot ||v_0|| + |r_{\text{end},x}/v_{\text{end},x}| \cdot ||v_{\text{end}}||$ being the distance of a beam traveling through vacuum and directly reflecting at a surface at position $x = 0$. It can be seen that the final spatial position of the actual ray path and a beam reflected at the critical density (in this case at $x = 0$) may differ significantly. But for small scale lengths the difference of the final position (mainly the Δy) can be neglected, so only the difference in optical path length would be of importance.

Figure 4.10 shows the path taken by a beam when it propagates perpendicular to the critical density through an exponential plasma density gradient (i.e., parallel to the gradient). This simple simulation requires no ray tracing and shows how the refractive index changes depending on the distance to the plasma. The parameters used here are a temperature of $T = 1\,\text{keV}$ for a Cu plasma with the scale length of the gradient $L = 1\,\mu\text{m}$. Due to the change of the refractive index, a beam traveling through the plasma takes a much shorter optical path, therefore gains a phase of about $\Delta\phi \approx -4.8\,\text{rad}$ relative to a beam traveling through vacuum until reaching the position of critical density (the negative sign implicates that the phase of the beam in plasma moved faster).

In fig. 4.11 the OPD between a beam traveling through plasma with n_c at $x = 0$ and a beam traveling through vacuum, both with an angle of incidence $\alpha = 23°$ and

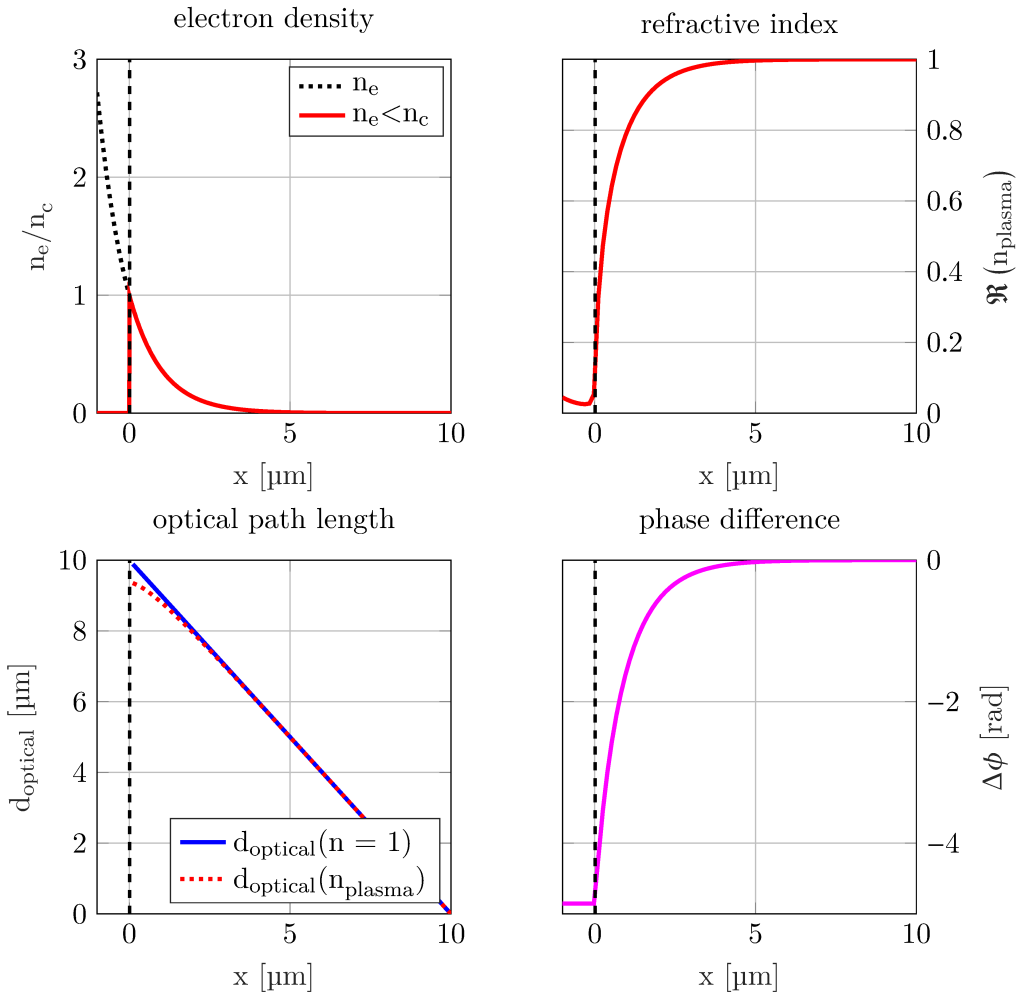


Figure 4.10: Phase shift of light propagating through Cu plasma density gradient with $T = 1\,\mathrm{keV}$, $L = 1\,\mu\mathrm{m}$. n_c positioned at $x = 0$. Top left shows the density distribution, with the red curve denoting the area where light can propagate. Top right shows the real part $\Re(n_{\mathrm{plasma}})$ of the refractive index inside the plasma. Bottom left shows the optical path length of a beam traversing through vacuum and through plasma. Bottom right shows the current phase difference due to the optical path difference between those two beams. Note, that the final phase difference of $\Delta\phi_{\mathrm{final}} \approx -4.8$ has to be doubled, if the beam is reflected at the critical density and travels out of the plasma again.

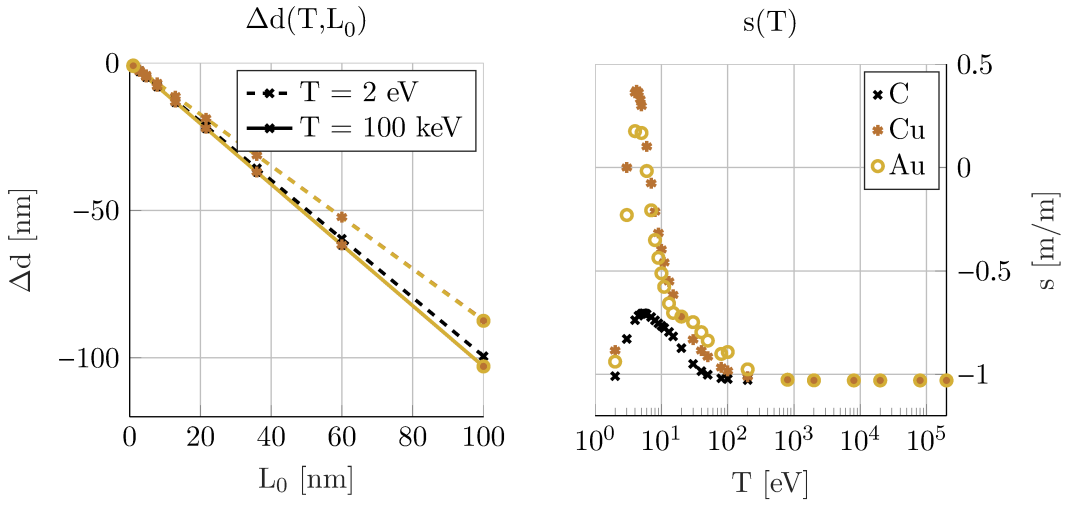


Figure 4.11: Left: optical path difference $\Delta d(T, L_0)$ of incoming beams at $\alpha = 23°$ depending on the plasma size L_0 for different plasma temperatures T are fitting a linear function $\Delta d = s(T) \cdot L_0$. Right: Slope $s(T)$ as OPD per scale length of the 1D plasma gradient in [m/m], since the slope $s(T = const.) = const.$.

reflecting at $x = 0$ is plotted. With the used algorithms, those temperatures have to be higher than 2 eV (which is most likely a numerical artifact, as will later be discussed). Also, given the fact that the beam curves away, it will always end up at the expected reflection angle (i.e., $\alpha_{in} = \alpha_{out}$), as if the beam was reflecting from a surface. Only the y position will be shifted, similarly to the Goos-Hänchen-shift (see section 2.8).

Lower temperatures than $T < 2$ eV may allow the beam to reach the critical density, where the simulation breaks. Analysis of different numerical methods have, however, revealed, that higher order algorithms, allow smaller temperatures (i.e., Runge-Kutta, or 3rd order Taylor allow $T > 2$ eV, while 2nd order Taylor allows only $T > 10$ eV), whereas the different methods do not yield different results in the regions where all converge. Therefore, it can be assumed that the breaching of the critical density is only a numerical artifact and not actually a physical process. Since no temperatures below $T < 10$ eV are relevant for this work, the Runge-Kutta algorithm is considered to be sufficient and no higher order algorithms are necessary.

The peak around $T \approx 5$ eV as a consequence of the discussion around fig. 2.6.

When analyzing the converging results, on the left side of fig. 4.11 data points are plotted which have the temperature held constant while the plasma size is varied. It is evident, that the corresponding Δd follows a linear correlation of the form

$$\Delta d = s(T) \cdot L_0. \tag{4.16}$$

The slopes, which will be called scaling factors $s(T)$ from now on, are therefore only temperature dependent for the different materials. As can be seen in the right graph (fig. 4.11), those do not follow a simple function, which is expected, since the relationship between ionization level and temperature is of complex nature. It shall be reminded here that this relationship is given by either the FLYCHK [37] simulation or the implemented Saha-equation solver [46], depending on the available ionization state data. If both data was available, the Saha solver is used, but the effective difference for the scaling factor is negligible.

Most interesting is the fact that at $T > 100\,\mathrm{eV}$ for low Z atoms like Carbon and high Z atoms like Gold this scaling factor seems to be $s \approx -1.05$ independent of material choice. Since for high temperatures fully ionized plasma can be assumed, and the effect of the ion collision frequency can be neglected, as the density is dominated by electrons, this effect can be expected. The value implies due to $L_0 = \frac{\Delta d}{s(T)}$ that the actual plasma scale length is about as big as the Δd. But most importantly, the ionization states do not impact the phase-shift significantly, as it is mostly temperature driven.

The data points at $5\,\mathrm{eV}$ shall be mentioned since the scaling factor produces an interesting spike there, which even produces a positive scaling factor. In this temperature area the ionization energies/levels of the atoms are very dominant for the relation between temperature and free electron density, as given by the Saha equation eq. (2.75). Those effects carry over into the collision frequencies, which yield the noticeable behavior.

It shall be reminded that a negative Δd implies that the light traveled faster through the plasma than through vacuum, wherefore, the negative sign for $s(T)$ implies that an expanding and positive plasma scale length boosts the speed of light, relative to a situation without plasma. It can be seen that an infinitesimally small plasma gradient would not produce a phase shift, only once the plasma reaches a significant extension does this shift reach a meaningful magnitude.

It shall be noted, that this work's interpretation of a plasma and the results differ fundamentally from the work of Frolov [35], which is currently the only other work known to the other which tries to explain phase shift and lateral displacement due to reflection on a plasma. Since Frolov assumes a sharp boundary between critical density and vacuum, he interprets the plasma as a parameterized surface, which yields him both phase and lateral displacements, similar to a metal. Using this work's interpretation of the plasma gradient however, for many temperatures it is not possible to even reach the critical density, wherefore a step like transition from plasma to vacuum would create no displacement and phaseshift. For this work, such a step like plasma gradient is obviously not an adequate assumption.

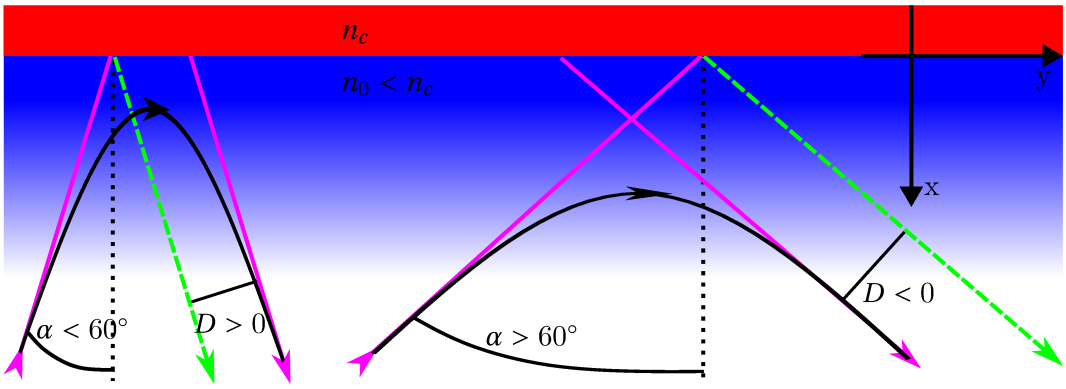


Figure 4.12: Sketch for lateral displacement in under-critical plasma gradient. For the analyzed material (copper with $T_p > 2\,\mathrm{eV}$) the displacement D switched sign around the $\alpha \approx 60°$ mark (see fig. 4.14), which implies the switch in direction. The green line shows the classical direct reflection on the critical density, while the purple line shows the perceived reflected ray.

However, this implies, that there exists at least a subset of plasma parameters, where the scale length is very short and the ray reaches the critical density thus that the beam receives both phase and later shift.

Comparing these results with the perpendicular reflection path (fig. 4.10), it can be seen that the phase shift does not have the value of $\Delta\phi_\perp = 2 \cdot 5.8\,\mathrm{rad} = 11.6\,\mathrm{rad} \neq \Delta\phi_{23°} \approx 2\pi \cdot -1.05\frac{1\,\mu\mathrm{m}}{\lambda} \approx 8.2\,\mathrm{rad}$. This is to be expected, since the movement on a curved path approaching the critical density should result in a longer total path than in the case of direct perpendicular reflection, thereby negating the speed gains.

Interpretation of this result must consider, that the position of the critical density mostly lies in front of the target surface, usually about $x(n_c \approx 3.5 \cdot L_0$ higher than the scale length of the plasma. Thereby, the overall wavefront deformation is dominated by the critical density position, but the phase shift due to $\Re(n) < 1$ inside the plasma still contributes $\sim \frac{1.05L_0}{3.5L_0 \cdot 2 + 1.05L_0} \approx 13\%$ to the overall phase shift.

4.2.4.3 Angular Dependence and Lateral Displacement

While not of high necessity for the following work, a brief discussion about the angular dependence of the scaling factor and lateral shift (GH-style-shift) shall be made. All simulations here are made for a copper plasma.

As can be seen in fig. 4.13 the scaling factor has a high dependence on the angle of incidence α. While its stays quite constant for low angles, high angles above $\alpha > 60°$ show a huge drop. This implies, that the light leaves the plasma much faster than if reflected classically.

This corresponds to the lateral displacement as seen in fig. 4.14. There it can

be seen that the lateral shift for an angle of incidence $\alpha > 60°$ is negative. This means, opposite to fig. 4.9, that the beam curves "faster" and is reflected "inside" the classical reflection rays as shown in right sketch of fig. 4.12. A positive displacement $D > 0$ however implies behavior identical to fig. 4.9, where the beam takes a "longer" path. It is still interesting, that, despite taking a "longer" path, the scaling factor $s(T, \alpha)$ is still for most temperatures and angles negative, which means, that the phase velocity $c_{\text{phase}} > c_0$ is able to compensate the longer way. Only for the curves given with $T = 3\,\text{eV}$ and $T = 5\,\text{eV}$, the scaling factor becomes positive, implying overall a delay to the reference beam. This correlates well with the lateral displacement for those temperatures, implying a longer way, which can here not be compensated. But even for those temperatures, the limit for high α is dominated by the shorter path inside the plasma.

Since for an angle of incidence $\alpha = 23°$ the displacement $D \approx 1.5 \cdot L$, i.e., in the order of magnitude of the scale length of the plasma. It has to be discussed, how this would affect the phase image.

Firstly, the plasma shape is assumed to be $L \sim L_0 \cdot \exp\left(\frac{-y^2}{2\sigma^2}\right)^p$. As the simulation was conducted for a 1D gradient, and the geometry of a ray curving through a plasma with $L \sim \sigma$ will obviously break the concept of the given D/L values, it has to be assumed that $L < \sigma$. In this case, for every ray passing through position y, the gradient $L(y)$ can be assumed to be constant over the ray's whole path, from which the respective $D(y)$ can be calculated. For the angle of incidence $\alpha = 23°$ the shift scales with $D/L \approx 1.55$, thus, if the beam travels in the positive y-direction (like in fig. 4.12) the shift would yield a final ray position slightly further with such that the final ray position $y_{\text{plasma,out}} > y_{\text{target,out}}$, compared to a classical reflection directly on the surface at $x = 0$[3].

Thus a beam, traveling through the side of the plasma, where L is small, the beam would be shifted less to the positive y direction, than if it moved through the middle part, where L is bigger. The shift for the rays would however not produce a lateral shift of the image, only it would change, from which position in the initial beam profile the light was coming from. If the beam profile would have a uniform intensity distribution, this would change for the imaged plasma, as now one side would be brighter than the other. The phase of the rays however would be unaffected by this, therefore not deforming the phase images.

A big scale length $L \sim \sigma$ however would be able to distort the phase image of the plasma, as now $L(y)$ for a single ray cannot be assumed to be constant any

[3]One shall be reminded here, that the surface at $x = 0$ is the critical density n_c of the plasma, which is not necessarily the reference surface in an experiment, since the critical density also expands away from a solid density target!

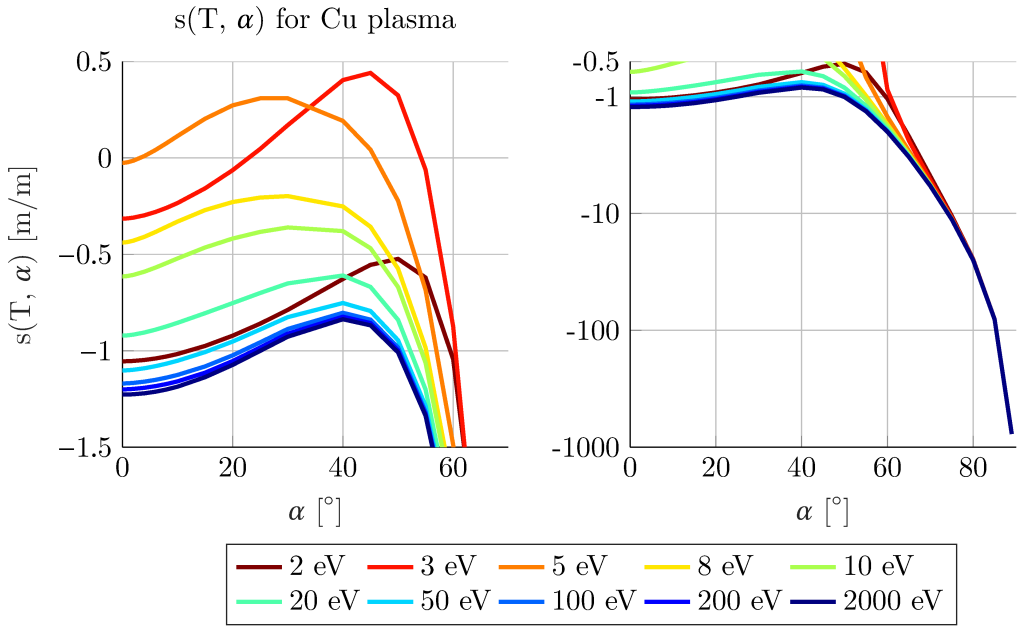


Figure 4.13: Scaling factor $s(T, \alpha)$ depending on plasma temperature T and angle of incidence α for Cu plasma.

more. In this case, the equation $\alpha_{\text{in}} = \alpha_{\text{out}}$ also breaks, as the plasma starts to create lens-like effects (those are not symmetrical, but conceptually similar). Since those effects are however impossible to calculate without exact knowledge about the actual plasma shape, and as it will be later seen (section 4.4), that images of such a big plasma (i.e., $L \sim \sigma$) are highly deformed by the imaging system, the presented approximation of the problem is just as informative as any other.

4.2.4.4 Discussion About Possible Relativity-Law Violation

To immediately address the elephant in the room, wavefronts that are bent forward (i.e., arrive earlier than their reference/travel faster) do not violate Einstein's theory of relativity. At first glance, it might appear that the information about the position of the plasma is transmitted faster than the speed of light in a vacuum ($c_{\text{phase}} = \frac{c_0}{n_{\text{plasma}}} \geq c_0$), since the part of the wavefront that is reflected beside the plasma appears to reach the detector much later than the part of the wavefront that is reflected at the plasma. However, this is not actually the case, as the wavefront continues to be enclosed by the envelope of the laser pulse. The explanation is as follows: The deformed wavefront would move into the early part of the pulse where there is no intensity, with a new wavefront moving into the pulse from the backside. Therefore, although the wavefront is deformed forward, it could not be measured before the actual intensity of the pulse reaches the detector, which is moving at the

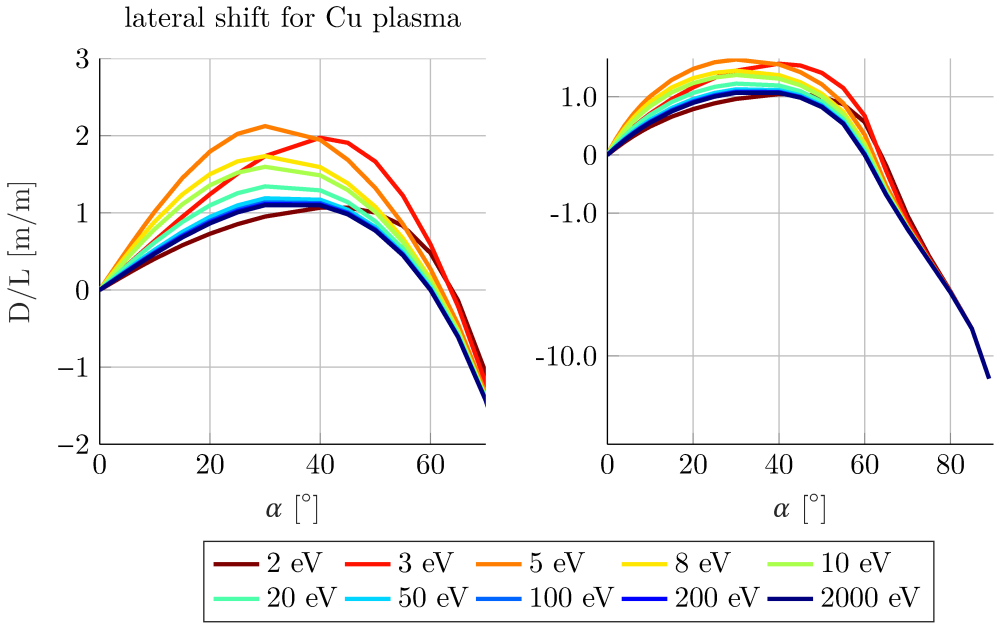


Figure 4.14: Ratio of lateral displacement D and plasma scale length L of ray reflected on uniform 1D-plasma gradient, similar to GH-shift section 2.8, depending on plasma temperature T and angle of incidence α for Cu plasma.

group velocity $c_{\text{group}} = c_0 \cdot n_{\text{plasma}} \leq c_0$. Thus, there is no violation of Einstein's law.

4.3 Combined Multi-fs and Ray Tracing

As seen in fig. 4.1 the temperature in front of the critical density is approximately constant, therefore, fig. 4.2 shows a short heating process in the first 20 fs and subsequent decay from $T_e(t = 20\,\text{fs}) \approx 10\,\text{keV}$ down to $T_e(t = 10\,\text{ps}) \approx 20\,\text{eV}$. While the exponential decay for the electron temperature is approximately the same for each target, the Ion temperature does not follow comparable patterns for each species, but stays mostly in the range from $T_i \approx 0.1\,\text{eV}$ to 10 eV.

Using those simulations in combination with the scaling factor between the optical path difference in a 1D plasma gradient against its scale length from fig. 4.11, the correct scaling factor depending on the plasma's lifetime can be approximated (see fig. 4.15). Since the temperature dependency of the scaling factor for Carbon is already very weak (see fig. 4.11), also the time dependent scaling factor is approximately constant $s_C(t) \approx -1$. For Gold the scaling factor changes more significantly, by almost a factor of two over the time span with $s_{\text{Au}}(t \approx 10\,\text{fs}) \approx -1$ rising to $s_{\text{Au}}(t \approx 10\,\text{ps}) \approx -0.7$, similarly as the $s_{\text{Cu}}(t)$. This graph assumes ideal (i.e., 100%)

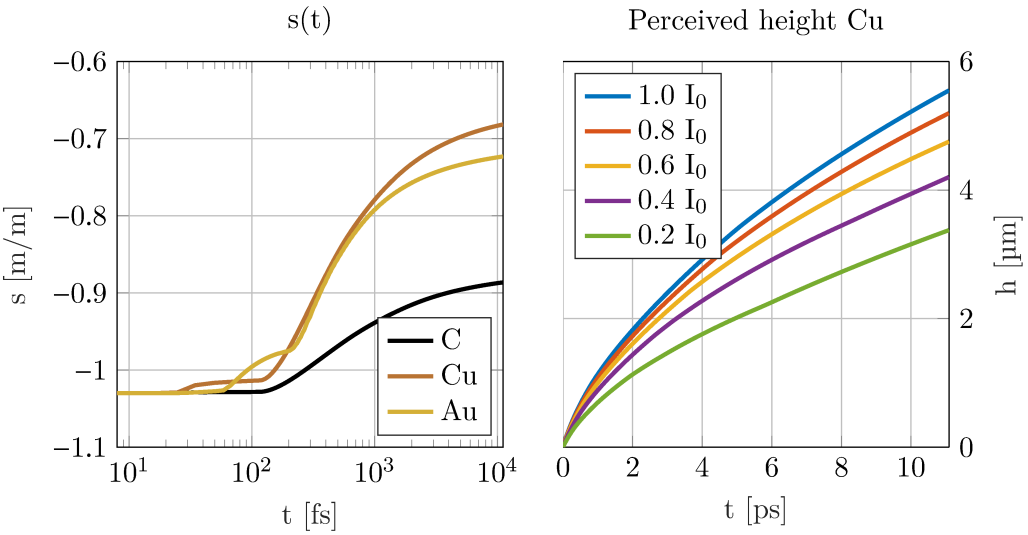


Figure 4.15: Left: scaling factor (4.16) between OPD (4.15) and plasma scale length (G.2) depending on time (i.e., temperature $T(t)$) from Multi-fs simulation. Right: perceived height of the center of the plasma, depending on time and different coupling intensities of the incoming laser pulse and a solid copper target.

coupling from laser to plasma. Taking the scaling factor together with the critical density position (i.e., scale length of the plasma) results in the right hand graph (fig. 4.15), displaying the perceived plasma height in the center of the plasma

$$h(t) = s(t) \cdot L_0(t) + 2 \cdot x(n_c(t)) \tag{4.17}$$

which are are calculated with the exact $s(t, I_0)$. Here $x = 0$ is assumed to be the position of the target from which the critical density n_c moves away in time. Those heights are effectively the same as the OPD, just from a different point of view. They are declared independently now since they will be used as the height of the phase distortion which will be needed in future chapters when calculating the diffraction and consequently measured phase shift on the CCD camera.

4.4 Diffraction

When a wave travels through time and space, the deformation it experiences is not trivial to calculate. While the intensity profile of aperture limited imaging systems is broadly described, the effects on phase images is often neglected and no standard literature addresses this particular issue. It is well known that for high NA phase images remain unaffected by magnification (i.e., while the intensity scales with magnification of the image, the phase-deformation changes its lateral size, but not the height of the phase). The following sections show, that the influence of apertures on phase images is much more critical than on the amplitudes, because not only the exact shape of the phase object is blurred, but also the absolute phase shift is diminished. Since these effects are crucial not only for this work, but for all phase-image diagnostics, a formalism to estimate the aberrations and a recipe to correct them in a certain range is presented here.

To develop this formalism, the underlying mathematical systems with their different implementations are benchmarked in the following sections. Since calculations of the effects of different optical systems scale widely different in computational time, but the effects relevant for phase-perturbations are not common knowledge, the next section starts from the overall most well defined, but computationally expensive formalism. The following sections simplify the mathematics but therefore create specific limitations. Thus less relevant parameters are eliminated to finally run more efficient simulations, specifically suited for the edge case relevant for this work.

The shape of the complex field[4] $U(\vec{s})$ is theoretically given by the Helmholtz equation.

Different approaches like the Kirchhoff, or Rayleigh Sommerfeld Diffraction Integral, yield correct results in most cases, but are often impossible to solve analytically and expensive to compute numerically. Therefore, in practice it is mostly more suitable to use the Fresnel, and Fraunhofer approach, which have even more boundaries, but are more efficient to compute. The next sections until section 4.4.5 are based on the widely available theory on numerical diffraction formalisms, as presented in [76–80]

[4] We use $\vec{s}$ as a position vector, instead of $\vec{r}$, which would be more common. This is necessary since three radii ρ, ϱ and r will be later introduced. To avoid even further confusion and separate them concisely, this approach was taken.

4.4.1 2D-Integrals

The incoming field $U(\vec{s})$ is always considered as the electric field $E(\vec{s})$ (amplitude and phase deformation) in combination with an aperture, i.e., a field distribution function $g(\vec{s})$, as is often found in other literature. For simplicity, they are combined in advance in all of the following formulas as $U(\vec{s}) = E(\vec{s}) \cdot g(\vec{s})$. It should also be noted that although the following analysis only considers linear polarization, both states (i.e., s- and p-pol or x- and y-pol) can be calculated independently of each other due to superposition. It is important to note, however, that some of the following approximations no longer apply to more complex types of polarization, such as radial or azimuthal polarization. If such are needed, refer to [81].

4.4.1.1 Kirchhoff Diffraction Integral

The complete description of wave propagation through apertures follows from the Helmholtz equation and Green's theorem. If the field $U(\vec{s})$ satisfies

$$(\nabla^2 + k^2)U(\vec{s}) = 0, \tag{4.18}$$

with the wavenumber $k = 2\pi/\lambda$, the field at point $\vec{p} = (x, y, z)$ can be expressed using the closed surface A surrounding $\vec{p}$ with

$$U(\vec{p}) = \frac{1}{4\pi} \int_A U(\vec{q}) \frac{\partial}{\partial \vec{n}} \left(\frac{e^{iks}}{s} \right) - \frac{e^{ikd}}{s} \frac{\partial U(\vec{q})}{\partial \vec{n}} \mathrm{d}A, \tag{4.19}$$

where $\vec{q} = (x', y', z')$ is a point on A,

$$s = |\vec{p} - \vec{q}|, \tag{4.20}$$

and $\partial/\partial\vec{n}$ denotes differentiation along the outward normal.

Applying Kirchhoff's boundary conditions, i.e., the field at the aperture is equal to the incident field without the aperture and zero wherever it is blocked, and the disturbance at distance s is given by $U(\vec{s}) = \frac{ae^{iks}}{s}$, the expression simplifies to the Kirchhoff diffraction integral

$$U(\vec{p}) = \frac{1}{i\lambda} \iint_A U(\vec{q}) \frac{e^{iks}}{s} (\cos\theta_0 + \cos\theta) \, \mathrm{d}A, \tag{4.21}$$

where A is the aperture plane (i.e., shining plane), θ_0 is the angle between the incident ray and the aperture normal, and θ is the angle between the observation point and the aperture normal.

While the integral is exact under Kirchhoff's assumptions (and while not close

to the aperture), its analytical evaluation is typically impossible. Hence, approximations are introduced to describe different diffraction regimes.

4.4.1.2 Rayleigh-Sommerfeld Diffraction Integrals

To begin with, the incoming wave can often be assumed to travel perpendicular to the aperture, i.e., $\theta_0 = 0$. Then each point of the wave passing through the aperture are expressed as a spherical wave, propagating in all directions, according to the Huygen-Fresnel principle. This approach formulated by Rayleigh and Sommerfeld leads to a solution of the Helmholtz equations which is correct for near and far field (i.e., close and far from the aperture)

$$U(x,y,z) = -\frac{1}{2\pi}\iint_{-\infty}^{+\infty} U(x',y',0)\,\frac{ze^{iks}}{s^2}\left(ik-\frac{1}{s}\right)\mathrm{d}x'\mathrm{d}y', \tag{4.22}$$

where, due to the definition of $z' = 0$

$$s = \sqrt{(x-x')^2+(y-y')^2+z^2}. \tag{4.23}$$

Direct numerical evaluations of the Rayleigh–Sommerfeld diffraction integral are usually computationally extremely expensive, scaling as $O(N^4)$ for an $N \times N$ grid. Which makes them most often not feasible to use since grid resolutions lower than the wavelength are necessary for correct phase resolution. A more efficient approach can be its Fourier representation, which corresponds to the angular spectrum method. The concept is to decompose the initial field into plane-wave components by a 2D Fourier transform, propagate each spectral component with the exact propagator, and then inverse transform back to the spatial domain.

If the input field in the source plane ($z = 0$) is $U(x, y, 0)$, its 2D Fourier transform is

$$\tilde{U}(f_x, f_y, 0) = \iint U(x,y,0)\, e^{-i2\pi(f_x x + f_y y)}\mathrm{d}x\mathrm{d}y,$$

where f_x and f_y are the spatial frequencies.

Propagation over a distance z is obtained by multiplying each spectral component with the transfer function

$$H(f_x, f_y, z) = \exp(ik_z z), \quad k_z = \sqrt{k^2 - (2\pi f_x)^2 - (2\pi f_y)^2},$$

with the wavenumber $k = 2\pi\lambda$. Evanescent waves with imaginary k_z decay exponentially and can be retained or neglected depending on the application.

The propagated field in the detection plane $U(x, y, z)$ is then given by the inverse

Fourier transform:

$$U(x,y,z) = \iint \tilde{U}(f_x,f_y,0)H(f_x,f_y,z)e^{i2\pi(f_x x+f_y y)}\,\mathrm{d}f_x\mathrm{d}f_y. \tag{4.24}$$

Numerically, this procedure is implemented via FFT:

1. Apply a 2D FFT to $U(x,y,0)$ to obtain $\tilde{U}(f_x,f_y,0)$.
2. Multiply by the transfer function $H(f_x,f_y,z)$.
3. Apply an inverse 2D FFT to return to the spatial domain.

This reduces the complexity to $O(N^2 \log N)$, which may look faster, but will still run into scaling problems, when, for example, focusing a big beam down into a point, since input and output grid need to have the same size and sampling requirements discussed in section 4.4.3.

4.4.1.3 Fresnel Diffraction Approximation

The Fresnel approximation can be used when the observation point $\vec{p}$ is not infinitely far from the aperture (see Fraunhofer diffraction 4.4.1.4), but still sufficiently far so that the phase can be approximated as quadratic.

When the aperture is located at the $z = 0$ plane, illuminated by a plane wave of unit amplitude, and the distance s eq. (4.23) is approximated as

$$s = \sqrt{(x-x')^2+(y-y')^2+z^2} \approx z + \frac{(x-x')^2+(y-y')^2}{2z},$$

which is valid when $z \gg (x-x')^2/\lambda$ and $z \gg (y-y')^2/\lambda$. Thereby the term from Rayleigh-Sommerfeld $\frac{ze^{iks}}{s^2}\left(ik-\frac{1}{s}\right) \approx \frac{ike^{ikz}}{z}$ due to $z \approx s$. Which leads to the much simpler form for the field at an observation point $\vec{p}$ with $z > 0$, which is given by

$$U(x,y,z) = \frac{e^{ikz}}{i\lambda z}\iint_{-\infty}^{\infty} U(x',y',0)e^{\frac{ik}{2z}[(x-x')^2+(y-y')^2]}\mathrm{d}x'\mathrm{d}y'. \tag{4.25}$$

The Fresnel approximation corresponds to a quadratic phase factor multiplying the aperture field, integrated over the aperture. It describes near-to-intermediate field diffraction patterns and smoothly transitions into Fraunhofer diffraction for large z. Similar to the Rayleigh-Sommerfeld diffraction, the Fresnel diffraction integral can be expressed in terms of Fourier transformations. Expanding the quadratic term,

$$U(x,y,z) = \frac{e^{ikz}}{i\lambda z}e^{i\frac{k}{2z}(x^2+y^2)}\iint U(x',y',0)e^{i\frac{k}{2z}(x'^2+y'^2)}e^{-i\frac{2\pi}{\lambda z}(xx'+yy')}\mathrm{d}x'\mathrm{d}y'.$$

this integral can be rewritten as a Fourier transformation of the aperture field multiplied by a quadratic phase factor. With

$$U_F(x', y') = U(x', y', 0) e^{i\frac{k}{2z}(x'^2+y'^2)},$$

then the transfer function

$$H(f_x, f_y) = e^{-i\pi\lambda z(f_x^2+f_y^2)}$$

leads to a simple to compute solution of

$$U(x, y, z) = \mathcal{F}\left[H(f_x, f_y) \cdot \mathcal{F}\left\{U_F(x', y')\right\}\right], \tag{4.26}$$

where $\mathcal{F}$ denotes the symmetric 2D Fourier transform, with spatial frequencies proportional to $(x/\lambda z, y/\lambda z)$.

4.4.1.4 Fraunhofer Diffraction

In the limit that the observation distance z is very large compared to the aperture size (see eq. (4.29)), the quadratic phase terms in the Fresnel integral can also be neglected. The result is the Fraunhofer diffraction approximation

$$U(x, y, z) = \frac{e^{ikz}}{i\lambda z} e^{i\frac{k}{2z}(x^2+y^2)} \iint_{-\infty}^{\infty} U(x', y', 0) e^{-i\frac{2\pi}{\lambda z}(xx'+yy')} \mathrm{d}x' \mathrm{d}y'. \tag{4.27}$$

This is a scaled Fourier transform of the aperture function. Thus, the Fraunhofer diffraction pattern observed in the far-field corresponds to the Fourier transform of the aperture distribution, evaluated at spatial frequencies proportional to the observation coordinates.

While the Fresnel integral can be written as a Fourier transform of the aperture field multiplied by a quadratic phase term, the Fraunhofer integral reduces to a direct Fourier transform of the aperture function.

Specifically, when assuming that $f_x = \frac{x}{\lambda z}$ and $f_y = \frac{y}{\lambda z}$, then the integral becomes

$$U(x, y, z) = \frac{e^{ikz}}{i\lambda z} e^{i\frac{k}{2z}(x^2+y^2)} \iint_{-\infty}^{\infty} U(x', y', 0) e^{-i2\pi(f_x x'+f_y y')} \mathrm{d}x' \mathrm{d}y'.$$

which resolves to

$$U(x, y, z) = \frac{e^{ikz}}{i\lambda z} e^{i\frac{k}{2z}(x^2+y^2)} \mathcal{F}\left(U(x', y', 0)\right), \tag{4.28}$$

where the Fourier transform $\mathcal{F}$ directly translates into the spatial domain at large

distance z.

4.4.2 Fresnel Number

The Fresnel number

$$F = \frac{a^2}{L\lambda} \tag{4.29}$$

with the aperture a, the distance from the aperture L and the wavelength λ gives information if Fresnel diffraction ($F \gg 1$) or Fraunhofer diffraction ($F \ll 1$) are more suitable for the situation. In this work (see section 3.4), $a \approx 2\,\text{cm}$ and $L \approx 15\,\text{cm}$, so that $F \approx 3333 \gg 1$, meaning the situation lies deep in the near field and Fraunhofer diffraction is not applicable.

However, even within the Fresnel regime the paraxial (quadratic-phase) approximation requires the higher-order phase terms to be negligible, i.e.,

$$\frac{F\Theta^2}{4} \approx \frac{a^4}{4L^3\lambda} \ll 1 \tag{4.30}$$

must hold. For the first lens this evaluates to ≈ 15, which is not $\ll 1$. Hence not even the standard Fresnel approximation is uniformly valid here, and higher-order terms in the diffraction integral cannot be neglected.

4.4.3 Sampling Considerations and Nyquist Limits

Until now every consideration assumed perfect mathematical evaluation. In reality those integrals have to be performed numerically, where new limitations arise, as computational time scales with the resolution of the integral. Thus the limiting factors for stable numerical evaluation are discussed here.

In FFT-based propagation, spatial sampling must fulfill Nyquist constraints. If sampling intervals in the input plane are Δx and Δy, with N_x and N_y pixels. The corresponding sampling frequency is

$$\Delta f_x = \frac{1}{N_x \Delta x}, \quad \Delta f_y = \frac{1}{N_y \Delta y},$$

and the highest spatial frequencies (Nyquist limits) are

$$f_{x,\max} = \frac{1}{2\Delta x}, \quad f_{y,\max} = \frac{1}{2\Delta y}.$$

These limits constrain the maximum propagation angles that can be represented without aliasing. A plane wave of transverse wavevector components (k_x, k_y) corre-

sponds to spatial frequencies $f_x = k_x/2\pi$, $f_y = k_y/2\pi$. To avoid aliasing, it requires

$$|f_x| \leq \frac{1}{2\Delta x}, \qquad |f_y| \leq \frac{1}{2\Delta y}.$$

Equivalently, the sampling intervals must satisfy

$$\Delta x \leq \frac{\lambda}{2\,\mathrm{NA}_x}, \qquad \Delta y \leq \frac{\lambda}{2\,\mathrm{NA}_y},$$

where NA is the effective numerical aperture of the system (i.e., the maximum transverse spatial frequency present in the field).

Since the integral is not only evaluated in real space but also in complex space, the gradient of the phase must also be resolved, leading to a necessary phase resolution of

$$\Delta\phi_x \leq \mathrm{NA}_x \frac{2\pi}{2}, \qquad \Delta y \leq \mathrm{NA}_y \frac{2\pi}{2},$$

where 2π gives a whole phase revolution. This becomes especially important if the wavefronts are highly deformed, as the phase cannot be unwrapped any more.

If the sampling is to coarse (large $\Delta x, \Delta y$), high-angle components are folding back (aliasing). If the grid size (N_x, N_y) is to small, it causes insufficient field-of-view and artificial periodic repetitions due to FFT wrap-around, as well as unexpected behaviour due to possibly important waves for a stable Helmholtz solution. If the phase resolution is not fine enough the direction of the wavefront becomes ill defined and unpredictable effects can occur. While the propagation distance z does not appear explicitly in the sampling condition (unlike Fresnel-FFT methods), the angular spectrum methods still require a grid large enough to capture the diffracted beam at z.

4.4.4 2D Evaluation

Using 2D propagation algorithms, the whole imaging apparatus was one time modeled correctly with the actual focal lengths and distances given in the experiment, by:

- simulation of the probe beam coming from the parabola and propagation to the target (i.e., plasma position)
- reflection on the target, where the phase-shape and reflectivity of the plasma is applied
- propagation towards the first collimating lens
- propagation towards the lens imaging the plasma into the interferometer

- propagation to the 1:1 achromatic lens
- propagation to the microscope apparatus (taken as one piece)
- propagation onto the CCD

and compared with a simplified imaging system:

- simulation of the probe beam coming from the parabola and propagation to the target (i.e., plasma position)
- reflection on the target, where the phase-shape and reflectivity of the plasma is applied
- propagation towards the first lens, as if it was the only lens, creating the overall magnification of $V = 20$
- propagation onto the CCD with respective distance for $V = 20$

Comparing those results yielded an identical final image for intensity and phase, wherefore it was concluded that the first lens is the most relevant diffraction-limiting lens. Therefore, all future simulations are conducted with only one lens with its respective numerical aperture (i.e., aperture and focal length) which seemingly yields comparable results to the whole apparatus while reducing the computational complexity by a factor ~ 5.

4.4.5 Reduction to Radial Symmetry

Since the algorithms described above are often very computationally intensive, especially at high diffraction angles, it is advisable to look for a 1D approach that exploits the radial symmetry of this problem, thereby reducing the complexity from $\mathcal{O}(N^4)$ and $\mathcal{O}(N^2 \log N)$ to $\mathcal{O}(N^2)$ (without requiring approximations). Various approaches for configurations of varying complexity have been developed by Ochoa [81, 82], whose solutions have been adapted for this case.

If the input field $U(x', y', 0)$ is linearly polarized and depends only on the radial coordinate

$$\rho = \sqrt{x'^2 + y'^2},$$

and the propagated field is also evaluated at the radial coordinates

$$r = \sqrt{x^2 + y^2},$$

then the problem becomes rotationally symmetric.

Thereby switching to polar coordinates (ρ, ϕ) in the source plane and (r, θ) in the observation plane allows to write the original Rayleigh-Sommerfeld integral (eq. (4.22)) as

$$U(r,z) = -\frac{z}{2\pi}\int_0^\infty \int_0^{2\pi} U(\rho,\phi)\frac{e^{ikd(\rho,\phi)}}{s^2(\rho,\phi)}\left(ik - \frac{1}{s(\rho,\phi)}\right)\rho \mathrm{d}\phi \mathrm{d}\rho, \tag{4.31}$$

where $s(\rho,\phi) = \sqrt{r^2+\rho^2-2r\rho\cos(\theta-\phi)+z^2}$ similar to eq. (4.23).

Hidden in this equation is a Bessel function, which allows to compress the double integral to one single integral [83]

$$U(r) = -z\int_0^\infty U(\rho)\frac{e^{ik\left(\varrho+\frac{r^2}{2\varrho}\right)}}{\varrho^2}\left(ik-\frac{1}{\varrho}\right)J_0\left(\frac{ikr\rho}{\varrho}\right)\rho \mathrm{d}\rho \tag{4.32}$$

with the Besselfunction of order 0, $J_0\left(\frac{ikr\rho}{\varrho}\right)$ and the truncated propagation distance $\varrho = \sqrt{z^2+\rho^2}$.

4.4.6 Radial Diffraction Results

Using the 1D radial diffraction integrals the following simulation procedure was used:

- creation of a beam with Gaussian intensity profile and Super-Gaussian phase profile (according to the Multi-fs simulation and scaling factor section 4.3)
- application of phase curvature from parabola
- propagation towards the lens, creating the overall magnification of $V = 20$
- application of aperture and phase curvature from lens (focal length f, aperture radius r_{ap})
- propagation onto the CCD with respective distance for $V = 20$ and f.

The fixed parameters are the magnification of $M = 20$, the wavelength $\lambda = 800\,\mathrm{nm}$, the spatial resolution $\mathrm{d}r = \frac{\lambda}{20}$, the aperture radius $r_{\mathrm{ap}} = 12.8\,\mathrm{mm}$, the intensity beam width $\sigma_I = 0.1\,\mathrm{mm}$ (the size does not matter here, as long as the whole plasma bubble is illuminated), the parameters for the Super-Gaussian shape of the plasma bubble (see eq. (4.6)) $\sigma_{\mathrm{plasma}} = 3.8\,\mu\mathrm{m}$ and $p = 1.36$. The amplitude A for the plasma height was varied in the range from $\phi_{0,\mathrm{in}} \equiv A = 0.1\,\mathrm{rad}$ to $80\,\mathrm{rad}$.

An example run is shown in fig. 4.16, where the input fields with their respective phase curvatures, as well as the out-coming $\Delta\phi = \phi_{\mathrm{plasma}} - \phi_{\mathrm{ref}}$ are shown at different stages in the simulation. The top row shows the input field, with described initial phase curvature (i.e., divergent, since the probe beam is focused in front of the target/plasma). Two runs are depicted, one with the plasma-perturbation in the phase (dotted lines, plasma creates $\Delta\phi = 1\,\mathrm{rad}$ bump with $r = 0.01\,\mathrm{mm}$ width) and

one without a phase deformation (i.e., reflection on flat surface - solid lines). For this simulation the effect of intensity absorption by the plasma bubble is ignored, as the intensity profile has no effect on the phase deformation and is not further discussed in this work. Thus both runs show identical initial intensity profiles.

The right row shows the difference in the phase between those runs. Thereby a direct image of only the plasma is created without the underlying phase curvature from the lenses. The middle row shows the fields after they passed the lens. The phase is now convergent. The seemingly big difference in phase for $r > 1\,\mathrm{mm}$ is not an actual effect, just a numerical artifact from the unwrapping. Since further calculations do not need an unwrapped phase, this effect vanishes again in the next step.

The final row, where the fields hit the CCD show again the initial profile. The phase is divergent again, with the small bump below $r < 0.2\,\mathrm{mm}$ in the perturbed field. The intensity profile of the beam with the plasma now also has intensity perturbations in the center, while the reference beam is perfectly imaged. The difference in phase on the bottom right image displays almost exactly the same profile as the initial plasma profile, just with a higher width, according to the magnification of $M = 20$.

It can be seen, that the phase of the carrier field also seems to be magnified, since it started with $\phi = 1.5\,\mathrm{rad}$ at $r = 0.25\,\mathrm{mm}$ and rises to $\phi = 30\,\mathrm{rad}$ at $r = 5\,\mathrm{mm}$, i.e., while the "width" was magnified, the same magnification occurred on the phase, which did not happen to the "plasma-bubble" deformation, where only the width was magnified. This effect is expected, as the carrier field's phase does not represent a spatial feature located at an object/image plane that is simply relayed by the imaging system. It rather describes the wavefront curvature of the beam itself, i.e., the distance to a (real or virtual) focus. This is a fundamentally different quantity than a local phase object such as the plasma bump.[5]

This algorithm is first evaluated by comparing different numerical apertures. Those are created by varying the focal length without changing the aperture (see appendix H). While it seems technically more correct to change the size of the aperture, this would be highly unfeasible for numerical apertures NA ≈ 1 since the

[5] A phase perturbation like the plasma bump in an aberration free system would be imaged with $E_{\mathrm{out}}(r) \propto E_{\mathrm{in}}(r/M)$, wherefore a local feature is reproduced with unchanged phase magnitude, where only the width is scaled by M. The carrier curvature however relates to the "axial" focus position, which scales with M^2 rather than M. Since the CCD is placed at the fixed image distance defined by the transverse magnification M, rather than at the true focus position, the phase curvature detected at the CCD reflects this mismatch rather than a simple rescaled copy of the input curvature. While in this simulation the mismatch between focus and image position happens to produce an apparent magnification factor equal to $M = 20$, this coincidence is specific to the chosen input curvature (i.e., initial focal position). A different initial curvature would generally yield a different scaling of the phase magnitude.

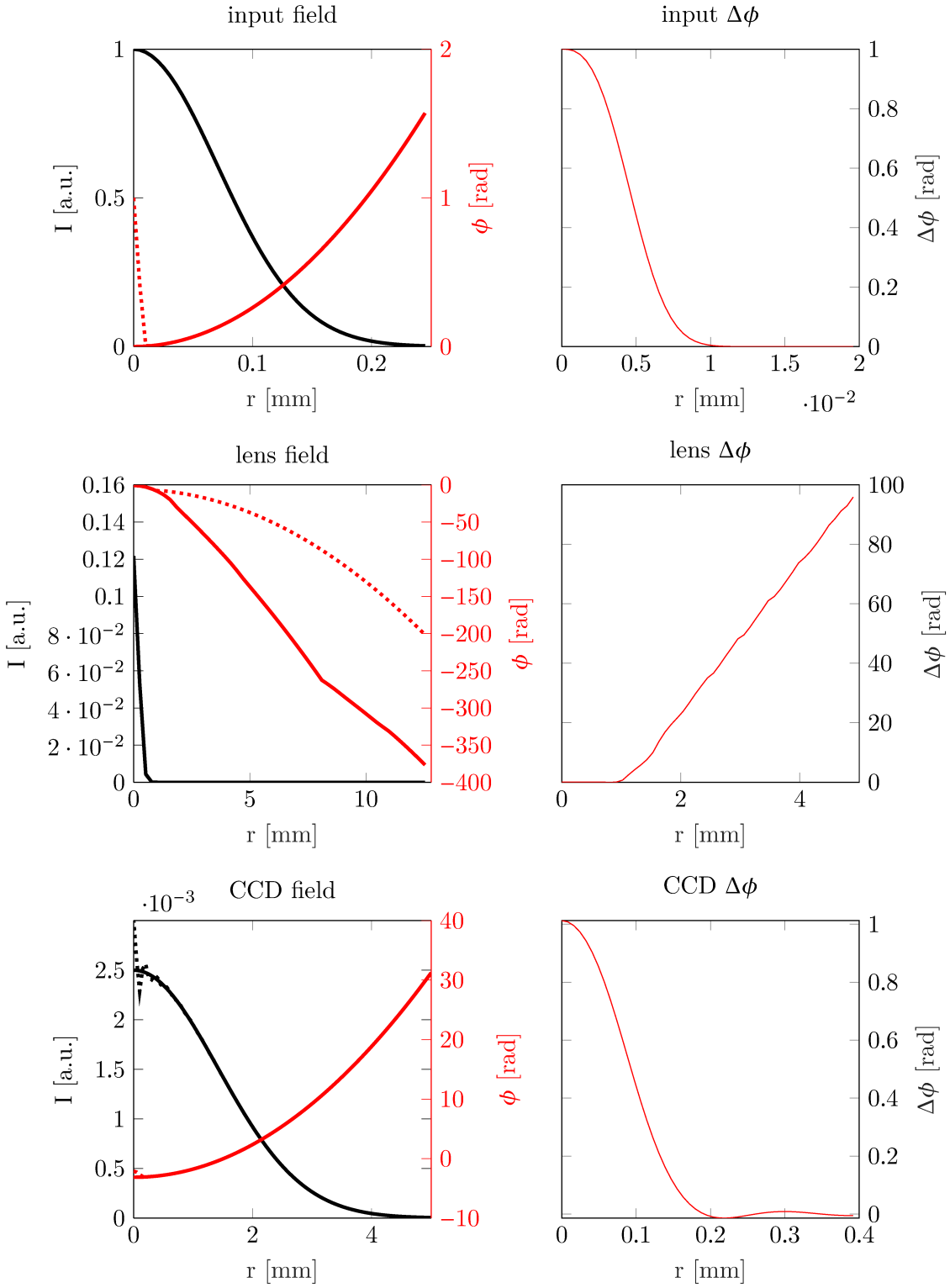


Figure 4.16: Radial diffraction simulation. Left side, intensity and phase of field at plasma, lens and CCD, with overall magnification $M = 20$. Solid lines show reference field without plasma, dotted line shows field with disturbance by plasma. Right side, phase difference between plasma and reference field. Phase image from input field is imaged well onto the CCD. The difference between the phases of the lens fields emerges mainly by unwrapping artifacts. See section 4.4.6 for a detailed explanation.

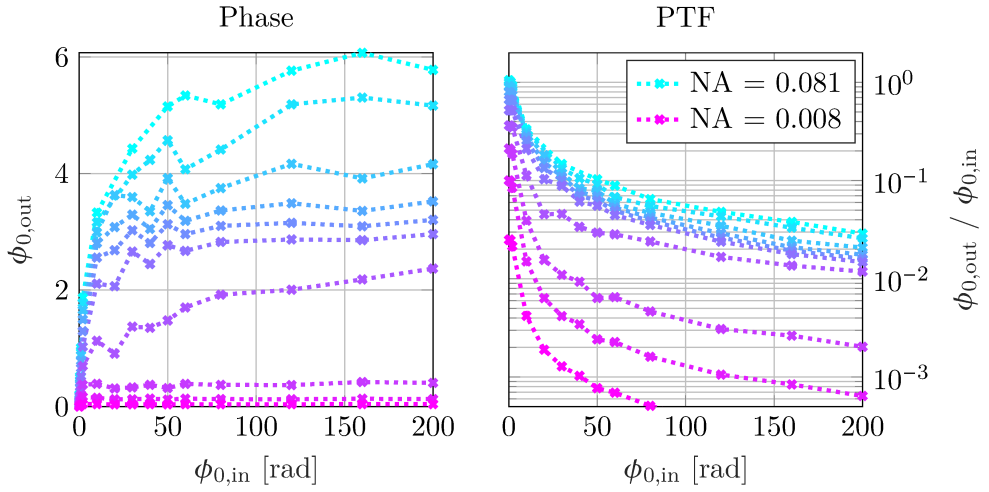


Figure 4.17: Phase transfer due to changing aperture size. Apertures sampled from $r_{\text{ap}} = 12.8\,\text{mm}$ in 10 equal steps down to 10% of the original size. Focal length $f = qty15cm = const.$, other parameters as described in section 4.4.6. Left picture shows direct phase matching, right figure shows PTF.

necessary resolution creates an incredibly huge grid at the aperture which would explode the computational time (also in appendix H it is shown that only the NA matters anyway). Thereby, the algorithm is benchmarked first and afterwards the experimentally more relevant NA are evaluated by changing the aperture (since it is small in the experiment) but fixing the focal length to $f = 15\,\text{cm}$. For a full evaluation see appendix H, here the most relevant results are solely presented. Figure 4.17 displays the phase transfer of a setup around the theoretical maximal possible NA of the imaging apparatus used in the experiment. The left plot shows the maximum height of the phase (i.e., central height) on the CCD against the initial phase-bump created by the plasma bubble. It can be seen, that high values get compressed very heavily. While low values get mapped correctly, as can be seen in the right graph, where the phase transfer function (PTF)

$$\text{PTF} = \frac{\phi_{0,\text{out}}}{\phi_{0,\text{in}}} \tag{4.33}$$

is ≈ 1 for high apertures and low phase bumps (NA > 0.04 and $\phi_{0,\text{in}} \leq 2\,\text{rad}$), for smaller apertures and higher $phi_{0,\text{in}}$ the output phase gets compressed and for very small NA $\phi_{0,\text{out}}$ becomes almost constant.

4.5 Reconstruction of Phase Images / Summary Simulations

In this section all pieces of the puzzle are combined to simulate an accurate phase image, regarding plasma expansion, phase speed in plasma gradients and phase compression due to NA.

A few parameters have to be assumed here, to a reasonable accuracy. At first the coupled intensity that heats the plasma and is not just reflected/scattered on the target and plasma surface is assumed to be $\sim 50\%$ [84]. As established in fig. 4.4 the plasma height after $t = 10\,\mathrm{ps}$ would be between $h = 1.5\,\mu\mathrm{m}$ to $2.2\,\mu\mathrm{m}$.

Also the width of the plasma can be assumed to be constant with $\sigma \approx 3.8\,\mu\mathrm{m}$. The scaling factor for the perceived height $s = -13$ to -8 combined with the previously described Multi-fs plasma parameters was already shown in fig. 4.15.

Combining those assumptions with the diffraction simulations, allows to predict the measured plasma height with time fig. 4.18.

When the parameters for diffraction have to be assumed, as already stated in the previous chapter (see section 3.4.2), the magnification of $V = 20$ is known and the dominant resolution limiting lens is known to be the second one, with focal length $f = 30\,\mathrm{mm}$. Calculating the numerical aperture NA simply from the approximate distance to the lens and its diameter results in $\mathrm{NA}_{\mathrm{optimal}} = \frac{r_{\mathrm{ap}}}{f} \approx 0.04$, which gives the upper limit, since it neglects all possible subsequent restrictions. To better visualize the effect of the NA in the region of interest, all subsequent plots use the range from $2 \cdot \mathrm{NA}_{\mathrm{optimal}} \approx 0.08$ to $0.2 \cdot \mathrm{NA}_{\mathrm{optimal}} \approx 0.008$.

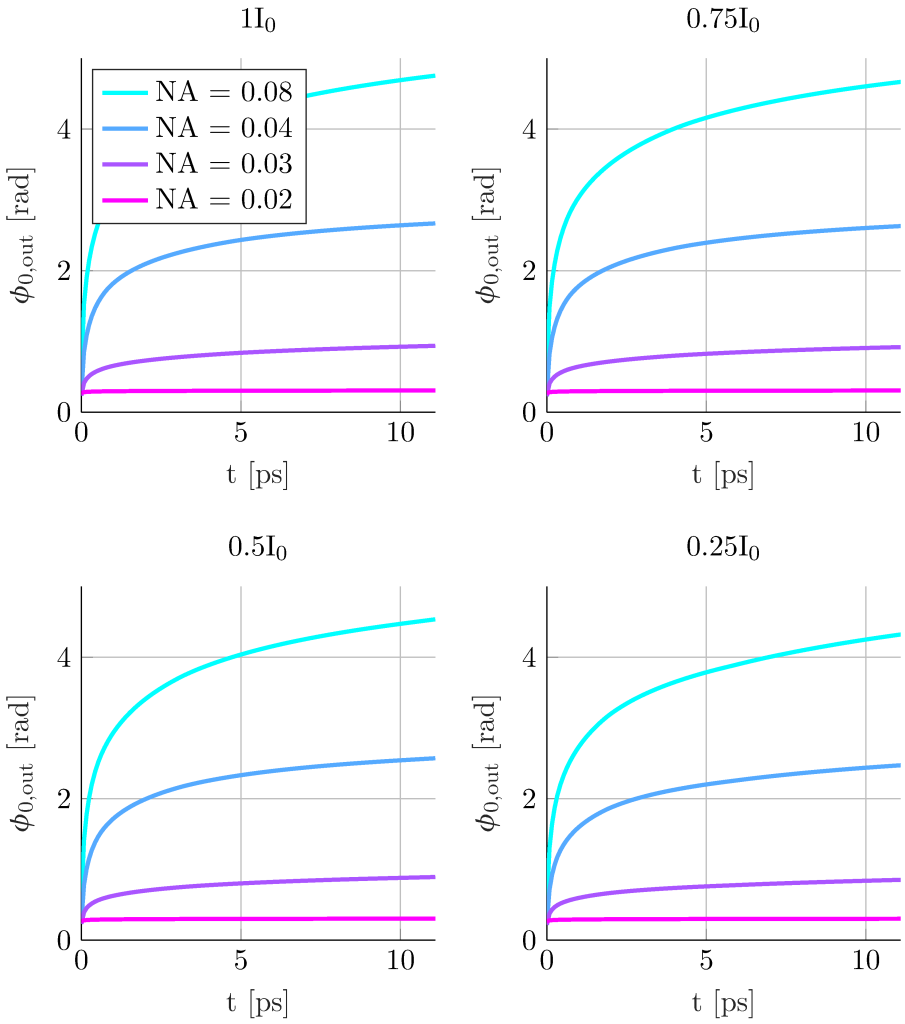


Figure 4.18: Simulated plasma height as measured on CCD, due to combination of Multi-fs plasma height, scaling factor from plasma gradient and phase compression due to diffraction. Each plot contains the time dependent phase-development according to the coupled intensity I_0 and NA.

Chapter 5

Results

In this chapter, the quantitative results of the phase shifts produced by plasma on solids are displayed. First, the phase shift of the plasma and its evolution are analyzed and compared with the predictions of the simulations. Afterwards, the phase rings, predicted by the simulations, are compared with the actual images.

5.1 Plasma Phase Images

The phase images (see fig. 5.1) are calculated according to section 2.10.1. The displayed early and late plasma images already present some of the most important characteristics. The height of the phase profile is developing in the range from ~ 0.1 rad up to ~ 1.5 rad over the span of up to 30 ps. This will be further discussed in section 5.2. The diameter of the late plasma appears to be $d \sim 30\,\mu m$, while for early plasma the central blob has $d < 50\,\mu m$ with a ring-like structure around it having a diameter of $d_{ring} \sim 100\,\mu m$. Those rings will be further discussed in section 5.3. From the here selected phase images, it is already clearly visible that the center of the plasma seems to move. This is further analyzed in appendix D.

The time scale of the plasma is defined by visually analyzing the phase pictures and identifying the first set of images (a set are images with an identical time stamp), where every single picture displays the same characteristics as the left image in fig. 5.1 (i.e., a central round structure with a ring around it). Since at every time step there are usually five interference images taken, there are usually at least three analyzable images in each set. About 20% of the total images cannot be evaluated due to noise distortion and forked fringes in the interference image. This effect is described in section 2.10.2. Also the ASE is sometimes able to produce a very thin plasma far earlier than the time when the actual pulse arrives, resulting in rare occasions where random single images, far earlier than the actual laser pulse

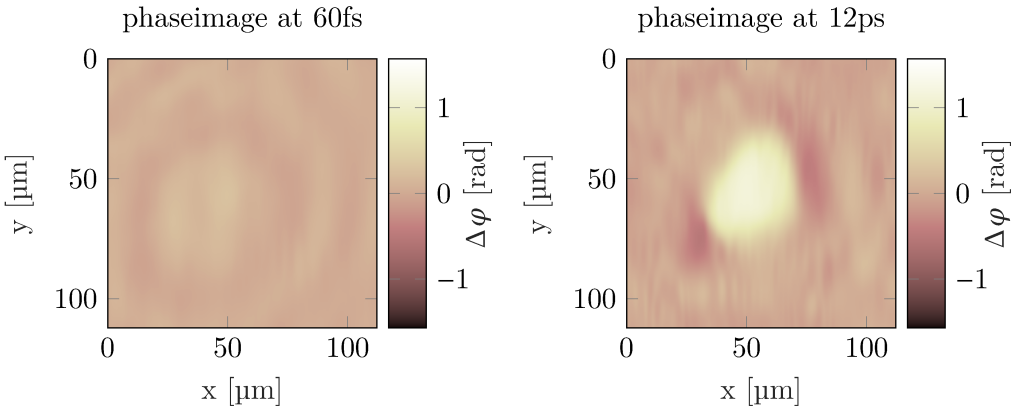


Figure 5.1: Phase images for early and late gold plasma.

interaction, show the signs of a plasma. The phase image at 60 fs describes the first time step after which every single image contains the plasma characteristics, while before $t \leq 0$ fs there is no plasma visible (except the rare random thin plasma bubbles).

5.2 Plasma Phase Development

The phase development of the plasma is characterized by the mean phase shift of the central area of the phase images. The center is determined by a 2D Gaussian fit, which is thereafter only used to verify the results, not to give any information about the plasma, since the plasma shape cannot be modeled by a simple Gaussian shape (at least in the phase image, due to NA phase-compression, section 4.4.6).

Figure 5.2 displays the development of the plasma-induced phase shift by gold, glassy carbon, and copper. The gold (Au-FS) target, shows an increase over the first 5 ps up to $\Delta\varphi \approx 1.2$ rad. Afterwards the phase seems to slowly decrease again.

In the case of carbon, the increase appears to be fairly linear, here it takes twice as long, up to 12 ps where the phase reaches $\Delta\varphi \approx 0.6$ rad. Also the phase does not seem to drop in the evaluated time frame but seems to stay approximately constant after 15 ps. In the period between 2 ps to 6 ps the amount of evaluable data points is due to noisy images very low, resulting in bigger errorbars and also some unusual outliers (like the data point at $t \approx 4$ ps, with $\Delta\varphi \approx 1$ rad). It seems nevertheless reasonable to assume approximately linear progression inside this time frame.

Finally, the copper target shows the smoothest curve. During the time frame of 25 ps the phase increases up to $\Delta\varphi \approx 1.3$ rad where it seems to plateau. It should be noted that the Cu measurement was the last measurement performed and also had the best target surface of all the materials analyzed. Therefore, the potential

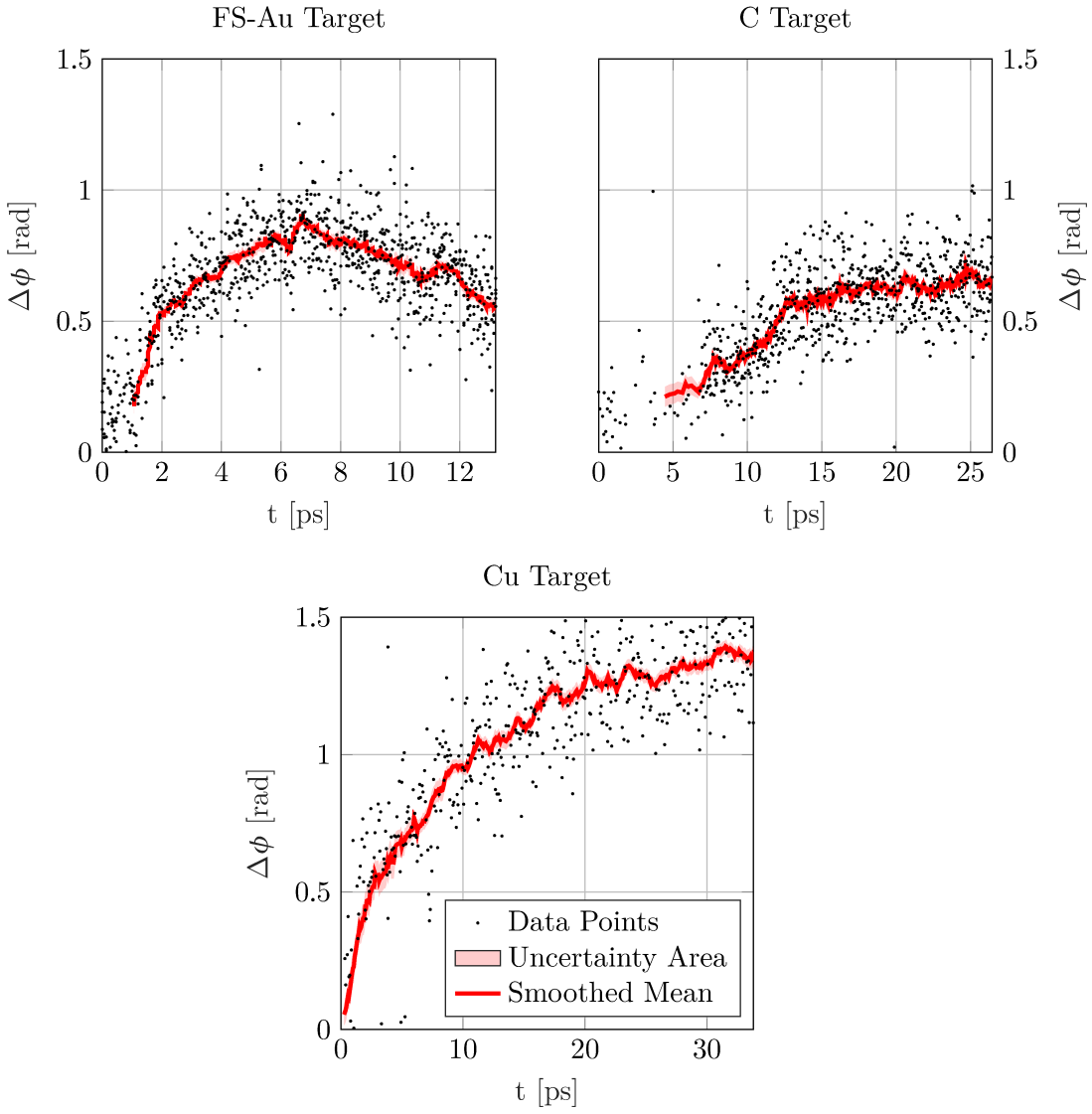


Figure 5.2: Phase shift development during early plasma.

errors due to misalignment of the optical devices or similar user errors are lowest in this series of measurements. In addition, this series contains only one sample per time step, as the evaluation process was also optimized.

Each series has a smoothed mean average curve plotted, which is calculated by taking a moving mean average over 31 data points, thus every mean point $p_{\text{mean},i} = \sum_{j=i-15}^{j=i+15} p_j/31$. The uncertainty area is the uncertainty of the mean value, calculated as the standard deviation of this data point divided by the square root of 31.

On closer inspection, it seems counterintuitive that the phase for the first gold values and also for the first carbon values is already in the range of $\Delta\varphi \approx 0.15\,\text{rad}$. One could argue that this is only slightly above the resolution limit for the phase, but that would be incorrect. As already earlier described, the evaluation algorithm works by fitting a Gaussian profile to find the central position of the plasma in the image. Since the noise often exceeds values of $\Delta\varphi \approx 0.2\,\text{rad}$, for small plasma sizes the algorithm is dominated by the noise, which is why it converges at a position of locally high noise values. As the plasma is always positive, the distortion produced by the plasma always pushes the fitted Gaussian distribution toward a positive "peak" and only rarely into "valley", resulting in this noise-dominated offset for the early averages. This effect is no longer relevant for later stages, as the center of the Gaussian distribution now matches the plasma position and not the noise, thereby the noise is symmetrical and does not produce an offset any more.

5.2.1 Relation to Reference Phase Shift

As discussed in section 2.9 reflection on a surface, especially if the surface is metallic, the reflected beam experiences a phase shift. Since the reference beam is taken from the surface next to the plasma, the reference beams phase is shifted against an absolute 0 phase. Those shifts are given in table 5.1. Since p-polarization is used for the probe beam, $\phi_p \approx 0.4\,\text{rad}$ with positive sign, should be expected for all targets.

	Au	Cu	C
n	0.16293	0.25	2.8
k	5.1813	5.1326	1.6
ϕ_p [rad]	0.414	0.417	0.355
ϕ_s [rad]	-2.791	-2.788	-2.838

Table 5.1: Optical parameters for different materials

The expected behavior would be as follows. When plasma is ignited, all the solid-state parameters are lost instantaneously, but the plasma has no initial ex-

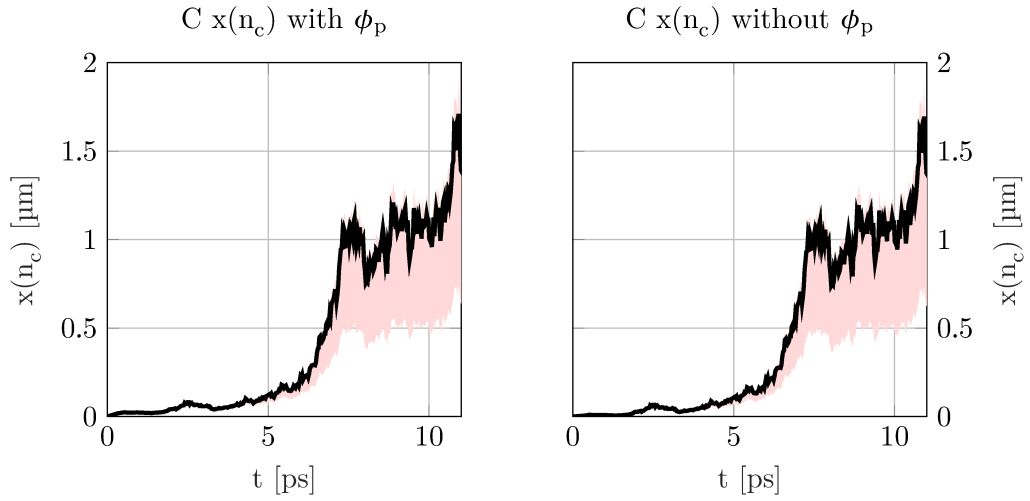


Figure 5.3: Calculated area of confidence for the C target due to NA estimation. Since overestimation is limited, but higher NA could be possible, the resulting errorbars are higher in direction of lower $x(n_c)$. Left image includes the phase shift ϕ_p at reference surface reflection, right image ignores it.

pansion. Therefore, the reference phase would be at $\phi_{ref} = \phi_p \approx 0.4\,\text{rad}$, while the absolute plasma shift would be $\phi_{plasma} = 0$ resulting in a measured shift of $\Delta\phi \approx -0.4\,\text{rad}$. This is not observed in the experiments. Rather the plasma is constantly developing upwards from the initial reference phase. This implies that the plasma seems to retain some of its solid state properties to some extent (i.e., extremely sharp plasma gradients cannot be described only with plasma ray tracing, but still contain some metal-like properties resulting in a similar phase shift). At later plasma stages however, with softer gradients and a further extended critical density, the relative phase shift should be regarded as completely present. The effect on the calculated critical density position is however negligible as displayed in figs. 5.3 to 5.5.

5.2.2 Comparison with Simulation

Using the scaling factor from section 4.2.4 in combination with the Multi-fs temperature/time simulation (see fig. 4.15) and the PTF from the NA the phase shift can be converted into a plasma height, i.e., the position of the critical density. The PTF was selected by finding the maximum value in the phase profile, thereby predicting the NA of the current imaging apparatus according to appendix H and fig. H.6. The predicted values are $\text{NA}_{Au} = 0.305$, $\text{NA}_{C} = 0.28$, and $\text{NA}_{Cu} = 0.31$. Figure 5.6 displays the back-transformed plasma sizes (right) and compares them to the predicted size due to the Multi-fs simulation (left). While the plasma size of the C

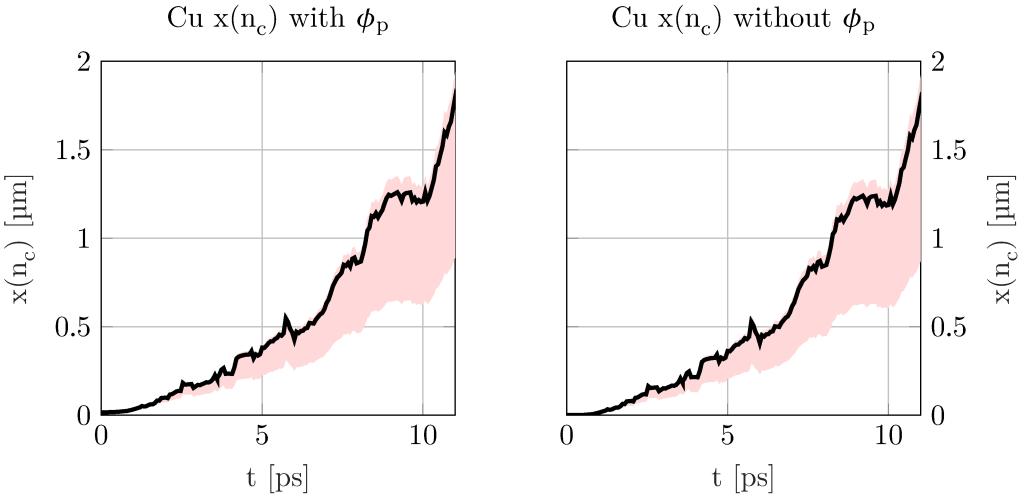


Figure 5.4: Calculated area of confidence for the Cu target due to NA estimation. Since overestimation is limited, but higher NA could be possible, the resulting errorbars are higher in direction of lower $x(n_c)$. Left image includes the phase shift ϕ_p at reference surface reflection, right image ignores it.

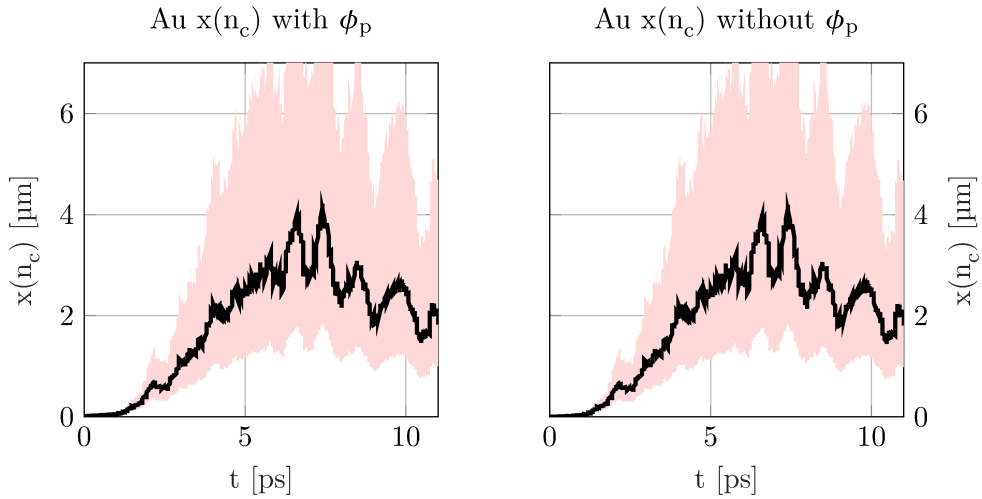


Figure 5.5: Calculated are of confidence for the Au-FS target due to NA estimation. Since the phase is not monotonically rising, overestimation of NA is likely. The area of confidence is symmetrical around the minimal possible NA and maximal reasonable NA. Left image includes the phase shift ϕ_p at reference surface reflection, right image ignores it.

and Cu targets appears comparable, albeit approximately 20% below the simulation predictions at $t = 10\,\text{ps}$, the Au plasma nevertheless exhibits a completely different behavior. This could either be explained by a wrongly assumed NA, as a higher NA would mean less compression, which in return would predict a lower initial profile. But then the $\max(\phi_{out})$ value would have never been reached, which would imply, that the plasma is much smaller than expected. For the FS-Au target this could actually be plausible, since $\Delta\phi$ (see fig. 5.2 does not plateau, but immediately starts falling after reaching its peak. Thereby the numerical aperture cannot be calculated by the given data.

On the other hand, a different explanation could be that the thin gold layer actually behaves like shown, reaching its maximum phase, and then starts dropping. Since the Multi-fs simulation may not be accurate for such thin layer interactions with a bulk target of a different material.

Even if the maximum height of the FS-Au plasma cannot be decisively obtained, it is still evident, that the initial expansion is significantly faster than for copper and carbon plasma. It can be assumed that this is an effect of coulomb explosion (CE) [85], since it is widely accepted that CE is feasible for plasma on dielectric targets, but only under specific circumstances obtainable for bulk-metal targets [86–89]. Since the thickness of the gold layer is only $\sim 60\,\text{nm}$, the whole layer becomes plasma within a few fs, while the plasma depth is in the range of $\sim 1\,\mu\text{m}$ on the timescale of $\sim 1\,\text{ps}$ according to Multi-fs, wherefore the plasma consists mainly of FS and perpetrates deep into the dielectric. Thus, fast charge neutralization by electron flow into the plasma would not be possible for the inward propagating plasma.

Since reflective phase imaging with pump-probe experiments is not a common procedure, comparable experimental data is rare. Data from [22] shows the expansion of aluminum plasma within $t < 0.3\,\text{ps}$ (intensity $I = 3 \times 10^{15}\,\text{W/cm}^2$, pulse length $\tau = 77\,\text{fs}$, central wavelength $\lambda = 620\,\text{nm}$, focal spot size $x \approx 7\,\mu\text{m}$) reaches only $x_{cr} = 12\,\text{nm}$. Those measurements do not contradict the here presented results, given their two orders of magnitude lower intensity and thereby expected smaller plasma sizes. Also the phase resolution used in the experiment for this thesis would not be able to replicate their early plasma measurements. Interestingly their results also show a lower plasma expansion rate than Multi-fs hydro simulations would predict.[1]

[1] Still I would argue their proposed phase resolution of $\lambda/2000$ is quite optimistic.

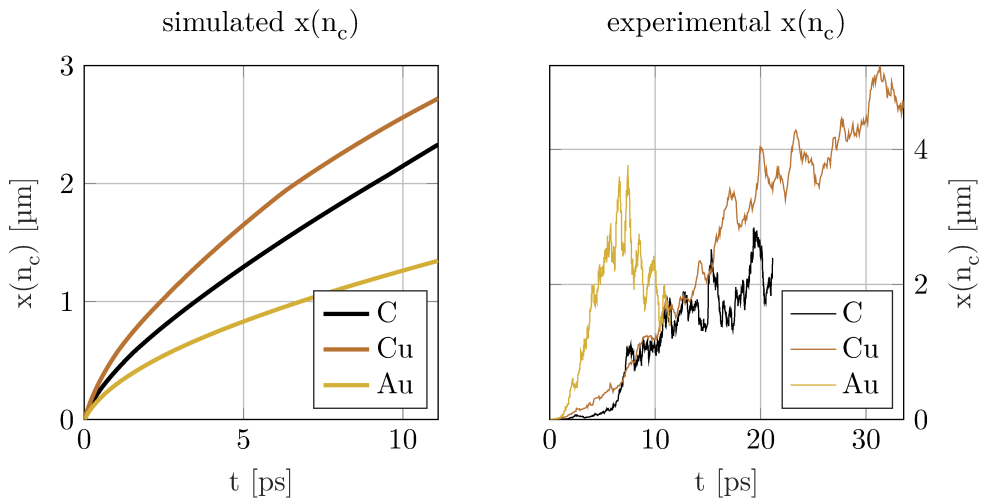


Figure 5.6: Left: position of critical density according to Multi-fs, up to $t = 11\,\mathrm{ps}$ Right: back transformed position of critical density according to the phase development (see fig. 5.2) in combination with section 4.3 and PTF.

5.3 Phase Rings

The early plasma on all targets displays an interesting feature. Around the middle position of the plasma are ring like structures in the phase (see fig. 5.7), which do not correlate with anything directly visible in the intensity (i.e., classical diffraction rings). A short discussion here shall explain this phenomenon.

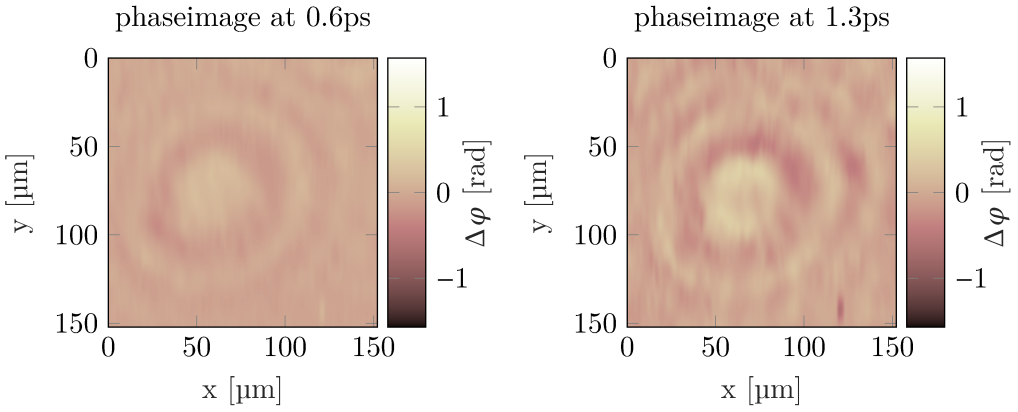


Figure 5.7: Phase images for early gold plasma with multiple rings.

5.3.1 Time Frame

Those rings exist on different time scales for different materials. For the Au-FS target the rings can be detected from $t_{rings} = 0\,\text{ps}$ to $8.5\,\text{ps}$, in the phase range of $\Delta\phi = 0\,\text{rad}$ to $0.8\,\text{rad}$ and $x_{cr} < 4\,\mu\text{m}$ while they are starting to become less prominent at about $t \approx 3\,\text{ps}$. For the carbon target the rings (i.e. ring like structures, since the quality of the images is not as good as the Au-FS and Cu target) can be seen at about $t_{rings} \approx 0\,\text{ps}$ to $10\,\text{ps}$, respectively $\Delta\phi = 0\,\text{rad}$ to $0.4\,\text{rad}$ and $x_{cr} < 1.8\,\mu\text{m}$. For the copper target the rings are clearly visible for $t_{rings} \approx 0\,\text{ps}$ to $0.7\,\text{ps}$. One could maybe consider some of the images up to $t = 3.5\,\text{ps}$ to contain some ring shaped structures, but they are much less prevalent, respectively $\Delta\phi = 0\,\text{rad}$ to $0.6\,\text{rad}$ and $x_{cr} < 1.3\,\mu\text{m}$.

5.3.2 Phase Rings by Diffraction

In fig. 5.8 an interesting diffraction pattern is presented. The simulated plasma and imaging parameters ($\sigma = 3.8\,\mu\text{m}$, $p = 1.36$, NA = 0.032) are consistent with all the other diffraction simulations (see appendix H). Figure 5.8 shows the intensity profile as dotted points overlayed on the phase profile. It can be seen, that the diffraction profile in intensity does not directly correlate with the rings. Some bumps in the intensity exist at the same radial positions where the rings occur, but it is not trivial to conclude the existence and relative dominance of the phase rings, just by taking the intensity profile into account. Especially interesting here is, that the phase rings seem to weaken with higher input phases, while the intensity rings seem to become more prominent. Figure 5.9 shows that this decrease in amplitude is not just an effect of relative amplitude to the main phase peak, but that in fact, the absolute value of the rings is lower.

This is also consistent with the experiment, where for later stages the rings vanish. Nevertheless, there are two more effects are also working together on letting the rings vanish. One is simply the resolution limit of the apparatus, as small phases lower than $\Delta\phi < 0.1\,\text{rad}$ cannot be confidently resolved. Additionally, one has to assume that at a reasonable size the plasma expansion has to be regarded in 3D, and cannot only be approximated in 1D, wherefore the simulation parameters (especially the plasma width) would be underestimated by the simulation. This would also reduce the maximal phase gradient, relative to the numerical aperture which leads to higher imaging precision resulting in less dominant phase rings.

As can be seen for carbon and copper, the phase rings disappear when the position of critical density is in the range of $x_{cr} = 1.3\,\mu\text{m}$ to $1.8\,\mu\text{m}$. While the plasma width is approximately $\sigma \approx 3.8\,\mu\text{m}$. It is prevalent that 1D expansion should not be

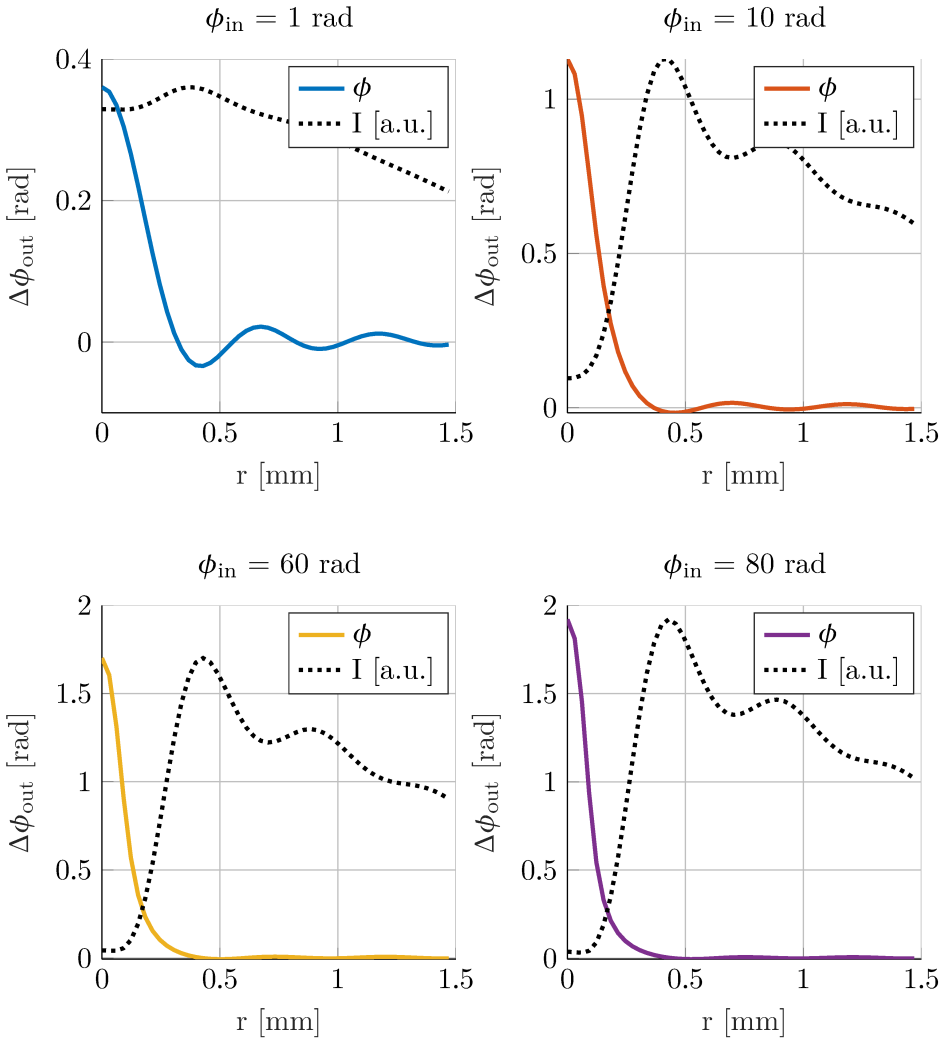


Figure 5.8: Phase rings simulated by radial diffraction integrals of comparable plasma sizes (width σ = 3.8 µm, Gaussian order p = 1.36) at specified heights through a 20 times magnifying lens with NA = 0.032. (Explosion plot of top right plot in fig. H.3). The colored lines display the phase profile, the black dotted lines the shape of the intensity profile.

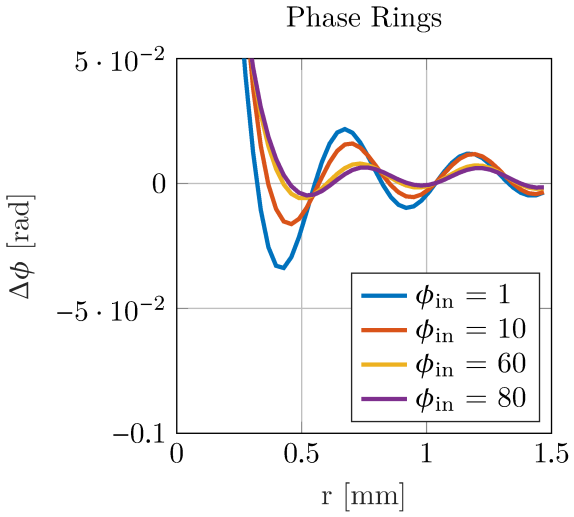


Figure 5.9: Zoomed comparison of phase rings by different input fields. Counter-intuitively, higher input field deformations create less pronounced rings.

assumed here any more, indicating that the given hypothesis is consistent. In the case of the gold target, where the errorbars are especially high, it can therefore be assumed, that the critical density should also not travel further than about half the plasma width, before the phase rings disappear. Therefore, the fastest expanding gold curves can with high certainty be disregarded.

Chapter 6

Conclusion

This thesis investigates the properties of a developing and expanding laser induced solid-surface plasma with high spatial and temporal resolution during its first picoseconds by interferometric phase imaging. The experimental method, appearing straight-forward at first glance, contains a multitude of subtle but crucial details never considered so far. By combining the concepts of high intensity solid state plasma physics with fluid simulations, the development of ray-tracing algorithms, wavefront imaging simulations, and phase-diffraction calculations a more comprehensive understanding of the experimental technique has been developed.

It was shown, that propagation through the electron density gradient of an expanding plasma bends the ray path. While the incoming and outgoing ray still show typical reflection behavior, the curve in front of the critical density creates a different optical path length due to a different geometrical path as well as the phase velocity $c_{\text{phase}} < c_0$, resulting in an overall phase shift relative to a direct reflection on the critical density. Additionally a geometrical lateral shift is introduced, similar to the Goos-Hänchen-shift in metals, where the angle of incidence has high impact on direction and magnitude of the shift. The refractive index has to be modeled accordingly to estimate the respective shifts, which shows a high dependence on plasma temperature and density. Thus additional information is necessary to accurately interpret the phase images, as this data is not directly accessible from them. For this work the predictions are done with the Multi-fs code, allowing estimations for plasma temperature and density at different expansion times. The scaling factor between the phase shift and the scale length of the plasma for the analyzed targets for temperature $T_p > 10\,\text{eV}$ is in the range $s(\alpha = 23°) \approx -1$ relative to direct reflection at the critical density. For lower temperatures the ionization levels play a big role on the refractive index which allows for some angle and temperature combinations even $s > 0$. It was found that in a 1D gradient the lateral shift for all

temperatures stays positive for angles of incidence below $\sim 60°$ and negative above with the exact crossover angle displaying a weak plasma temperature dependence.

The phase shift and Goos-Hänchen-shift upon reflection on metal was calculated, since the metal surface is used as the reference. Since the plasma-driven phase deformation is much bigger, the effects of the metal are currently smaller than the noise on the experimental data and thereby not relevant for this work. However, for similar experiments analyzing only the very start of the plasma development within $t < 100\,\mathrm{fs}$ after plasma ignition, these effects have to be considered.

Diffraction simulations showed, that wavefront imaging through finite numerical aperture (NA) compresses phase peaks. The compression scales with the peak height and saturates ("phase-clipping") for high phase deformations. While this inhibits accurate measurements for big plasmas, it allows to accurately determine the actual NA of the optical system, which in turn enables more precise reconstruction of early plasma phase profiles, where compression occurs but full clipping has not yet set in.

The experimental data conducted by igniting plasma on gold coated fused silica, glassy carbon and copper targets confirmed the simulated plasma size trends. The phase compression was directly observed as well as diffraction-phase-rings, validating the diffraction simulations. It was shown, that the phase rings do not carry direct information about the plasma or the surrounding region and are rather an artifact of the NA of the imaging system. The small NA used in the experimental setup limits the range that can be accurately evaluated to the early plasma $t \lesssim 5\,\mathrm{ps}$ where compression is not as present and the resulting errorbars much lower. Comparison between the targets showed that in these early phases, the conductivity of the target does not significantly influence the early plasma development. Previous measurements were evaluated and guidelines for the alignment of the setup were created by displaying the important benchmarks necessary to create correct phase images.

The plasma development on the thin layered Au-FS target shows interesting behavior for future research, as either the NA was underestimated, leading to an apparently slower plasma expansion than predicted, or complex behavior occurred in the later plasma development $t > 5\,\mathrm{ps}$ that cannot be reproduced by the hydrodynamic Multi-fs code.

It is shown, that the developed setup is well suited for future experiments targeting small or early plasma. Here a high numerical aperture is suggested to be chosen, allowing higher precision in plasma height analysis with less phase compression. Especially the initial plasma ignition can be studied much more precise, allowing high accuracy analysis of the scale length and critical density position and movement.

Using the high temporal resolution $\tau < 30\,\mathrm{fs}$ precise measurements allow further investigation into ultra fast laser-solid-plasma interactions. Also the diffraction simulations predict that NA clipping with deformed wavefronts creates a characteristic pattern in the intensity profile, distinct from clipping with flat wavefronts. Since this pattern is a direct signature of the underlying wavefront deformation, it may be possible to reconstruct the deformation from intensity measurements alone. This would eliminate the need of the whole interferometic setup, relying only on a camera and the imaging lenses, simplifying the experimental system.

The plasma gradient ray tracing predicts now a correction factor for the critical density position, displaying how naive interpretation of the data would overestimate the plasma size. Countering this effect, a phase transfer function for different numerical apertures predicts compression of the phase image, making actually big phase deformations appear much smaller after they passed an imaging apparatus. In combination those simulations establish, that for very early plasma stages ($t < 1\,\mathrm{ps}$) the correction factor is necessary to conduct accurate predictions, while observations of big and late plasma necessitate an imaging apparatus with exceptionally high numerical apertures to acquire reproducible results with qualitative and quantitative significance.

Bibliography

[1] Koji Sugioka and Ya Cheng. Ultrafast lasers - reliable tools for advanced materials processing. Light: Science & Applications, 3(4):149, April 2014.

[2] S. Svanberg. Some Medical and Biological Applications of Ultrafast Lasers, pages 437–448. Springer New York, 2004.

[3] M. Hentschel, R. Kienberger, Ch. Spielmann, G. A. Reider, N. Milosevic, T. Brabec, P. Corkum, U. Heinzmann, M. Drescher, and F. Krausz. Attosecond metrology. Nature, 414(6863):509–513, November 2001.

[4] Xijie Hu, Ka Fai Mak, Jinwei Zhang, Zhiyi Wei, and Ferenc Krausz. Ultrafast lasers for attosecond science. Light: Science & Applications, 15(1), January 2026.

[5] Le Gao, Qiming Zhang, and Min Gu. Femtosecond laser micro/nano processing: from fundamental to applications. International Journal of Extreme Manufacturing, 7(2):022010, December 2024.

[6] Dimitri Batani. Matter in extreme conditions produced by lasers. EPL (Europhysics Letters), 114(6):65001, June 2016.

[7] M. Trtica, J. Savovic, M. Kuzmanovic, D. Rankovic, and J. Stasic. Libs hydrogen isotopes detection: Significance in nuclear/fusion technology. Journal of Applied Spectroscopy, 90(6):1318–1324, January 2024.

[8] Steffen Mittelmann, Kévin Touchet, Xianglei Mao, Minok Park, Sebastijan Brezinsek, Georg Pretzler, and Vassilia Zorba. Hydrogen isotope analysis in w-tiles using fs-libs. Scientific Reports, 13(1), February 2023.

[9] L. Gallais, D.-B. Douti, M. Commandré, G. Batavičiūtė, E. Pupka, M. Ščiuka, L. Smalakys, V. Sirutkaitis, and A. Melninkaitis. Wavelength dependence of femtosecond laser-induced damage threshold of optical materials. Journal of Applied Physics, 117(22), June 2015.

[10] H.J. van der Meiden, S. Almaviva, J. Butikova, V. Dwivedi, P. Gasior, W. Gromelski, A. Hakola, X. Jiang, I. Jõgi, J. Karhunen, M. Kubkowska, M. Laan, G. Maddaluno, A. Marín-Roldán, P. Paris, K. Piip, M. Pisarčík, G. Sergienko, M. Veis, P. Veis, S. Brezinsek, and the EUROfusion WP PFC Team. Monitoring of tritium and impurities in the first wall of fusion devices using a libs based diagnostic. Nuclear Fusion, 61(12):125001, November 2021.

[11] J. Oelmann, N. Gierse, C. Li, S. Brezinsek, M. Zlobinski, B. Turan, S. Haas, and Ch. Linsmeier. Depth-resolved sample composition analysis using laser-induced ablation-quadrupole mass spectrometry and laser-induced breakdown spectroscopy. Spectrochimica Acta Part B: Atomic Spectroscopy, 144:38–45, June 2018.

[12] Maria Balcerzak. An overview of analytical applications of time of flight-mass spectrometric (tof-ms) analyzers and an inductively coupled plasma-tof-ms technique. Analytical Sciences, 19(7):979–989, July 2003.

[13] Jan Riedlinger, Lars Torben Schwabe, Qëndresa Ibraimi, and Georg Pretzler. Electromagnetic thomson parabola spectrometer for detection of fs laser-driven kev ions. AIP Advances, 14(8), August 2024.

[14] Richard B Miles, Walter R Lempert, and Joseph N Forkey. Laser rayleigh scattering. Measurement Science and Technology, 12(5):R33–R51, April 2001.

[15] S. S. Harilal, M. C. Phillips, D. H. Froula, K. K. Anoop, R. C. Issac, and F. N. Beg. Optical diagnostics of laser-produced plasmas. Reviews of Modern Physics, 94(3):035002, August 2022.

[16] M. B. Schwab, A. Sävert, O. Jäckel, J. Polz, M. Schnell, T. Rinck, L. Veisz, M. Möller, P. Hansinger, G. G. Paulus, and M. C. Kaluza. Few-cycle optical probe-pulse for investigation of relativistic laser-plasma interactions. Applied Physics Letters, 103(19):191118, November 2013.

[17] Taylor. Transmission and reflection of electromagnetic waves by a hot plasma. Journal of Research of the National Bureau of Standards, Section D: Radio Science, 69D(5):735, 03 1958.

[18] Y-Q Cui. Laser absorption and hot electron temperature scalings in laser–plasma interactions. Plasma Physics and Controlled Fusion, 55(8):085008, June 2025.

[19] J. Hernandez-Rueda, D. Puerto, J. Siegel, M. Galvan-Sosa, and J. Solis. Plasma dynamics and structural modifications induced by femtosecond laser pulses in quartz. Applied Surface Science, 258(23):9389–9393, September 2012.

[20] Fatemeh Rezaei. A new method for calculation of thick plasma parameters by combination of laser spectroscopy and shadowgraphy techniques. J. Anal. At. Spectrom., 29(12):2371–2378, October 2014.

[21] D. S. Sitnikov, P. S. Komarov, A. V. Ovchinnikov, and S. I. Ashitkov. Femtosecond fourier interferometry of a nonideal plasma. Technical Physics, 54(4):520–526, April 2009.

[22] J. P. Geindre, A. Mysyrowicz, A. Dos Santos, P. Audebert, A. Rousse, G. Hamoniaux, A. Antonetti, F. Falliès, and J. C. Gauthier. Frequency-domain interferometer for measuring the phase and amplitude of a femtosecond pulse probing a laser-produced plasma. Optics Letters, 19(23):1997, December 1994.

[23] V. Schmidt, W. Husinsky, and G. Betz. Dynamics of laser desorption and ablation of metals at the threshold on the femtosecond time scale. Physical Review Letters, 85(16):3516–3519, October 2000.

[24] S. Kahaly, S. Monchocé, H. Vincenti, T. Dzelzainis, B. Dromey, M. Zepf, Ph. Martin, and F. Quéré. Direct observation of density-gradient effects in harmonic generation from plasma mirrors. Physical Review Letters, 110(17):175001, April 2013.

[25] C. Rödel, D. an der Brügge, J. Bierbach, M. Yeung, T. Hahn, B. Dromey, S. Herzer, S. Fuchs, A. Galestian Pour, E. Eckner, M. Behmke, M. Cerchez, O. Jäckel, D. Hemmers, T. Toncian, M. C. Kaluza, A. Belyanin, G. Pretzler, O. Willi, A. Pukhov, M. Zepf, and G. G. Paulus. Harmonic generation from relativistic plasma surfaces in ultrasteep plasma density gradients. Physical Review Letters, 109(12):125002, September 2012.

[26] C. Thaury, F. Quéré, J.-P. Geindre, A. Levy, T. Ceccotti, P. Monot, M. Bougeard, F. Réau, P. d'Oliveira, P. Audebert, R. Marjoribanks, and Ph. Martin. Plasma mirrors for ultrahigh-intensity optics. Nature Physics, 3(6):424–429, April 2007.

[27] Constantin Bernert, Stefan Assenbaum, Florian-Emanuel Brack, Thomas E. Cowan, Chandra B. Curry, Marco Garten, Lennart Gaus, Maxence Gauthier, Sebastian Göde, Ilja Goethel, Siegfried H. Glenzer, Thomas Kluge, Stephan Kraft, Florian Kroll, Michael Kuntzsch, Josefine Metzkes-Ng, Markus Loeser,

Lieselotte Obst-Huebl, Martin Rehwald, Hans-Peter Schlenvoigt, Christopher Schoenwaelder, Ulrich Schramm, Mathias Siebold, Franziska Treffert, Tim Ziegler, and Karl Zeil. Off-harmonic optical probing of high intensity laser plasma expansion dynamics in solid density hydrogen jets. Scientific Reports, 12(1), May 2022.

[28] M. Borghesi, A. Giulietti, D. Giulietti, L. A. Gizzi, A. Macchi, and O. Willi. Characterization of laser plasmas for interaction studies: Progress in time-resolved density mapping. Physical Review E, 54(6):6769–6773, December 1996.

[29] E. Tokunaga, T. Kobayashi, and A. Terasaki. Frequency-domain interferometer for femtosecond time-resolved phase spectroscopy. Optics Letters, 17(16):1131, August 1992.

[30] Z. Chen, M. Mo, L. Soulard, V. Recoules, P. Hering, Y. Y. Tsui, S. H. Glenzer, and A. Ng. Interatomic potential in the nonequilibrium warm dense matter regime. Physical Review Letters, 121(7):075002, August 2018.

[31] T. Ao, Y. Ping, K. Widmann, D. F. Price, E. Lee, H. Tam, P. T. Springer, and A. Ng. Optical properties in nonequilibrium phase transitions. Physical Review Letters, 96(5):055001, February 2006.

[32] F Goos and H Hänchen. A new and fundamental experiment on total reflection. Ann. Phys.(Leipzig), 1(7-8):333–346, 1947.

[33] Christian Imbert. Calculation and experimental proof of the transverse shift induced by total internal reflection of a circularly polarized light beam. Physical Review D, 1972.

[34] H. Vincenti, S. Monchocé, S. Kahaly, G. Bonnaud, Ph. Martin, and F. Quéré. Optical properties of relativistic plasma mirrors. Nature Communications, 5(1), March 2014.

[35] A. A. Frolov. Spatiotemporal goos–hänchen effect at a laser pulse reflection from boundary of supercritical plasma. Physics of Plasmas, 30(1):013103, 01 2023.

[36] K. Eidmann, J. Meyer-ter Vehn, T. Schlegel, and S. Hüller. Hydrodynamic simulation of subpicosecond laser interaction with solid-density matter. Physical Review E, 62(1):1202–1214, July 2000.

[37] H.-K. Chung, M.H. Chen, W.L. Morgan, Y. Ralchenko, and R.W. Lee. Flychk: Generalized population kinetics and spectral model for rapid spectroscopic analysis for all elements. High Energy Density Physics, 1(1):3–12, 2005.

[38] Michael Stumpf. Pump-Probe-Experimente zur Diagnostik von Ultrakurzpuls-Laser-Plasmen. Master's thesis, Heinrich-Heine-Universität Düsseldorf, February 2017.

[39] H. J. Eichler und J. Eichler. Laser: Bauformen, Strahlführung, Anwendungen. Springer, 2010.

[40] Georg Pretzler. Höchstleistungs-Kurzpulslaser. Vorlesungsskript, 2000.

[41] Drude model (pdf). `https://campus.mst.edu/physics/courses/4323/drude.pdf`, 2023. Accessed: 2023-02-06.

[42] H. M. Rosenberg. The Solid State: An Introduction to the Physics of Solids for Students of Physics, Materials Science, and Engineering. Oxford University Press, Oxford, 3 edition, 1988.

[43] Max Born and Emil Wolf. Principles of Optics, chapter XIII. Pergamon Press, 1975.

[44] Lyman Spitzer. Physics of Fully Ionized Gases. New York, Interscience Publishers, 1962.

[45] J.A.M. van der Mullen. Excitation equilibria in plasmas; a classification. Physics Reports, 191(2):109–220, 1990.

[46] Mofreh R. Zaghloul. Reduced formulation and efficient algorithm for the determination of equilibrium composition and partition functions of ideal and nonideal complex plasma mixtures. Physical Review E, 69(2):026702, February 2004.

[47] Jan Riedlinger, Qëndresa Ibraimi, Lars Torben Schwabe, Simon Lohnert, and Georg Pretzler. Temperature and density measurement of an ultra short laser pulse driven carbon plasma by skin-layer ion emission analysis. Journal of Applied Physics, 137(19), May 2025.

[48] P. E. Ciddor. Refraction into an absorbing medium. American Journal of Physics, 44(8):786–787, 08 1976.

[49] Fedor I Fedorov. To the theory of total reflection. Journal of Optics, 15(1):014002, January 1955.

[50] Andrea Aiello. Goos–hänchen and imbert–fedorov shifts: a novel perspective. New Journal of Physics, 14(1):013058, January 2012.

[51] Kurt Artmann. Berechnung der seitenversetzung des totalreflektierten strahles. Annalen der Physik, 437(1-2):87–102, 1948.

[52] Mitsuo Takeda, Hideki Ina, and Seiji Kobayashi. Fourier-transform method of fringe-pattern analysis for computer-based topography and interferometry. Journal of the Optical Society of America, 72(1):156, January 1982.

[53] G. Pretzler, H. Jäger, and T. Neger. High-accuracy differential interferometry for the investigation of phase objects. Meas. Sci. Technol, 4:649–658, 1993.

[54] FemtosourceTM rainbowTM - User Manual.

[55] FemtosourceTM rainbowTM CEP4 - User Manual.

[56] D. Strickland and G. Mourou. Compression of amplified chirped optical pulses. Optics communications, 55(6), 1985.

[57] FemtopowerTM HE CEP - User Manual.

[58] Amplitude Technologies. Dazzler User Manual, 2025.

[59] Amplitude Technologies. Sequoia User Manual, 2025.

[60] Florian Kasper Kleeschulte. Analyse der Elektronenemission bei der Wechselwirkung ultrakurzer, hochintensiver, CEP-stabilisierter Laserpulse mit Festkörperplasmen. PhD thesis, Heinrich-Heine-Universität Düsseldorf, 2017.

[61] I. H. Malitson. Interspecimen comparison of the refractive index of fused silica∗,†. J. Opt. Soc. Am., 55(10):1205–1209, Oct 1965.

[62] Michele Magnozzi, Marzia Ferrera, Lorenzo Mattera, Maurizio Canepa, and Francesco Bisio. Plasmonics of au nanoparticles in a hot thermodynamic bath. Nanoscale, 11(3):1140–1146, 2019.

[63] HTW Hochtemperatur Werkstoffe GmbH. Datasheet SIGRADUR® Glassy Carbon. 86672 Thierhaupten Germany, 8667.

[64] P. B. Johnson and R. W. Christy. Optical constants of the noble metals. Physical Review B, 6(12):4370–4379, December 1972.

[65] Dr. Rolf T. Borlinghaus. Super-resolution - on a heuristic point of view about the resolution of a light microscope. Technological Readings, 2014.

[66] R. Ramis, K. Eidmann, J. Meyer-ter Vehn, and S. Hüller. Multi-fs – a computer code for laser–plasma interaction in the femtosecond regime. Computer Physics Communications, 183(3):637–655, March 2012.

[67] A. Sommerfeld. Zur Elektronentheorie der Metalle auf Grund der Fermischen Statistik: I. Teil: Allgemeines, Strömungs- und Austrittsvorgänge. Zeitschrift für Physik, 47(1–2):1–32, January 1928.

[68] J.A. Gaunt. Continuous absorption. Royal Society of London, 1930.

[69] G.D. Tsakiris and K. Eidmann. An approximate method for calculating planck and rosseland mean opacities in hot, dense plasmas. Journal of Quantitative Spectroscopy and Radiative Transfer, 38(5):353–368, November 1987.

[70] Alexander Rickert. Zustand und optische Eigenschaften dichter Plasmen, volume MPQ-Report 175. Max-Planck-Institut für Quantenoptik, 1993.

[71] K. Eidmann. Radiation transport and atomic physics modeling in high-energy-density laser-produced plasmas. Laser and Particle Beams, 12(2):223–244, June 1994.

[72] M.S. Cho, K. Matsuo, S. Fujioka, S.J. Hahn, B.I. Cho, and H.-.K. Chung. Opacity calculation for aluminum, iron, and gold plasmas using flychk code. Journal of Quantitative Spectroscopy and Radiative Transfer, 257:107369, December 2020.

[73] Stephen Seltzer. X-ray form factor, attenuation and scattering tables, nist standard reference database 66, 1995.

[74] Lucian Montagnino. Ray tracing in inhomogeneous media. J. Opt. Soc. Am., 58(12):1667–1668, Dec 1968.

[75] Anurag Sharma, D. Vizia Kumar, and A. K. Ghatak. Tracing rays through graded-index media: a new method. Applied Optics, 21(6):984, March 1982.

[76] Max Born and Emil Wolf. Principles of Optics, chapter VIII. Pergamon Press, 1975.

[77] Arnold Sommerfeld. Optics, lectures on physics. Academic Press inc., 1954.

[78] Joseph W. Goodman. Introduction to Fourier Optics, chapter 3-4. McGraw-Hill Inc.,US, 1968.

[79] David G. Voelz. Computational Fourier Optics: A MATLAB Tutorial. Digital Library, SPIE PRESS, jan 2011.

[80] Tomasz Kozacki, Konstantinos Falaggis, and Malgorzata Kujawinska. Computation of diffracted fields for the case of high numerical aperture using the angular spectrum method. Appl. Opt., 51(29):7080–7088, Oct 2012.

[81] Noé Alcalá Ochoa. One-dimensional integrals to calculate the two-dimensional rayleigh–sommerfeld diffraction integrals for non-rotationally symmetric functions and general polarizing illuminating fields. Optics Communications, 437:264–270, April 2019.

[82] Noé Alcalá Ochoa. Accurate non-paraxial approximation to the vectorial rayleigh–sommerfeld diffraction integrals for elliptical, radial, azimuthal and other polarized illuminating fields. Optics Communications, 429:112–118, December 2018.

[83] Noé Alcalá Ochoa. Alternative approach to evaluate the rayleigh-sommerfeld diffraction integrals using tilted spherical waves. Opt. Express, 25(10):12008–12019, May 2017.

[84] Prashant Kumar Singh, Y. Q. Cui, Amitava Adak, Amit D. Lad, Gourab Chatterjee, P. Brijesh, Z. M. Sheng, and G. Ravindra Kumar. Contrasting levels of absorption of intense femtosecond laser pulses by solids. Scientific Reports, 5(1), December 2015.

[85] T. Ditmire, J. W. G. Tisch, E. Springate, M. B. Mason, N. Hay, R. A. Smith, J. Marangos, and M. H. R. Hutchinson. High-energy ions produced in explosions of superheated atomic clusters. Nature, 386(6620):54–56, March 1997.

[86] N. M. Bulgakova, R. Stoian, A. Rosenfeld, I. V. Hertel, and E. E. B. Campbell. Electronic transport and consequences for material removal in ultrafast pulsed laser ablation of materials. Physical Review B, 69(5):054102, February 2004.

[87] N.M. Bulgakova, R. Stoian, A. Rosenfeld, I.V. Hertel, W. Marine, and E.E.B. Campbell. A general continuum approach to describe fast electronic transport in pulsed laser irradiated materials: The problem of coulomb explosion. Applied Physics A, 81(2):345–356, July 2005.

[88] W. Wendelen, D. Autrique, and A. Bogaerts. Space charge limited electron emission from a cu surface under ultrashort pulsed laser irradiation. Applied Physics Letters, 96(5), February 2010.

[89] Sha Tao and Benxin Wu. The effect of emitted electrons during femtosecond laser–metal interactions: A physical explanation for coulomb explosion in metals. Applied Surface Science, 298:90–94, April 2014.

[90] Konrad Kopitzki and Peter Herzog. Einführung in die Festkörperphysik. Springer Berlin Heidelberg, 2017.

[91] Shaista Babar and J. H. Weaver. Optical constants of cu, ag, and au revisited. Appl. Opt., 54(3):477–481, Jan 2015.

[92] S. I. Ashitkov, M. B. Agranat, P. S. Kondratenko, S. I. Anisimov, V. E. Fortov, V. V. Temnov, and K. Sokolowski-Tinten. Ultrafast laser-induced phase transitions in tellurium. Journal of Experimental and Theoretical Physics Leftters, 76(7):461–464, October 2002.

[93] DeepL GmbH. DeepL Translator, 2022-2026. Neural machine-translation service.

[94] OpenAI. ChatGPT (Version 1 - GPT-5.6 Luna), nov 2022-2026. Large language model.

[95] Anthropic. Claude (Sonnet 5), 2026. Large language model.

Acronyms

AFM atomic force microscopy

AOPDF Acousto-Optic Programmable Dispersive Filter

ASE amplified spontaneous emission

Au-FS gold - Fused Silica

CCD charge-coupled device

CE coulomb explosion

CEP Carrier Envelope Phase

CPA chirped-pulse amplification

EOS equation of state

FFT Fast Fourier Transformation

FS Fused Silica

FWHM full width at half maximum

GH Goos-Hänchen

HHG High Harmonic Generation

IF Imbert–Fedorov

iFFT Inverse Fast Fourier Transformation

LTE local thermal equilibrium

NA numerical aperture

ND:YAG neodymium-doped yttrium aluminum garnet

ND:YLF neodymium-doped yttrium lithium fluoride

OPD optical path difference

PTF phase transfer function

Ti:Sa titanium-sapphire

Appendix A Phase Shift Due to Drude Model

At the beginning of the work, the hypothesis was put forward that the phase rings (see fig. 5.7) could be related to moving currents in the metal generated by the plasma. However, this is not the case here, as the discovery of more than one ring has effectively disproved this hypothesis. Especially, as it can now be explained much more easily by the diffraction simulations. Nevertheless, the conceptual work should not be lost and is therefore presented here.

A.1 Solid State

Since the plasma studied in this work is ignited on a solid target, the reflective properties of the solid are used as a baseline for the analysis of the plasma. However the interaction between the plasma and the solid introduces additional effects, such as the induction of currents within the material and heating of its electrons. These interactions not only influence the solid's behavior but also provide insight into the dynamic relationship between the plasma and the substrate.

The following considereations are needed to include them into the Drude model for approximations of the scattering times in relation to the temperature.

A.1.1 Debye Temperature

The Debye temperature Θ_D is a characteristic temperature representing the energy scale of lattice vibrations in a solid. It is derived from the Debye model, which approximates the phonon spectrum of a solid and is directly related to the maximum vibrational frequency (Debye frequency) of the lattice.

$$\Theta_D = \frac{hc_s}{2k_B}\left(\frac{6N}{\pi V}\right)^{1/3} \tag{A.1}$$

where h is Planck's constant, c_s is the speed of sound in the material, k_B is Boltzmann's constant and N/V is the number density of atoms in the solid. Θ_D provides a reference point for distinguishing between different temperature regimes of phonon behavior:

- At temperatures $T \ll \Theta_D$, only low-frequency acoustic phonons are active, leading to quantum effects in the vibrational behavior.
- At $T \gg \Theta_D$, the phonon spectrum becomes classical, with phonons occupying higher energy states.

In metals, the Debye temperature determines the phonon wave vectors contributing to scattering processes and is used in scaling relations for resistivity and scattering rates.

A.1.1.1 Temperature Dependence of Electron Scattering Time

Electron-phonon scattering dominates electron scattering in metals, and its behavior depends significantly on the temperature regime relative to Θ_D:

A.1.1.2 High-Temperature Regime ($T > \Theta_D$)

Phonons in the high-temperature regime $T > \Theta_D$ are thermally excited, with their density being proportional to the temperature T. The scattering in this regime becomes quasi-elastic, characterized by large-angle scattering due to the high energies of the phonons. Consequently, the electron scattering rate $1/\tau$ is directly proportional to the temperature, leading to an electrical conductivity σ that varies inversely with temperature $\sigma \sim T^{-1}$.

A.1.1.3 Low-Temperature Regime ($T < \Theta_D$)

In the low-temperature regime $T < \Theta_D$, only low-frequency acoustic phonons are available, and their density varies as T^3. Scattering in this regime involves small-angle interactions and can be inelastic. The scattering rate follows a T^5 dependence due to the combined effects of low phonon energy and limited phase space. Consequently, the electrical conductivity σ varies as $\sigma \sim T^{-5}$, as described by the Bloch–Grüneisen formula.

A.1.1.4 Intermediate and Practical Considerations

- At very low temperatures, other scattering mechanisms like impurity and boundary scattering dominate.
- Umklapp processes, where momentum conservation involves a reciprocal lattice vector, enhance scattering at high temperatures by increasing the range of phonon modes contributing to the process.

A.2 Phase Shifts by Electron Density and Collision Time Variation

As seen in the section for the Drude Model 2.3 the refractive index for metals is dependent on the plasma frequency 2.54 of the metal, therefor it is possible to

describe the complex refractive index n in relation to the electron density, the collision time, and the reduced mass of the electrons

$$n(n_e, \tau, m^*) = \sqrt{1 - \frac{n_e e^2}{m^* \varepsilon_0 \left(\omega^2 + i\frac{\omega}{\tau}\right)}} \tag{A.2}$$

Using this the phase jump from reflection can be described using the Fresnel description, if the reflection coefficients r_p and r_s get calculated using 2.86 and 2.87. Therefor the phase jump for each polarization can be expressed using

$$\delta_\alpha = \arctan\left(\frac{\Im(r_\alpha)}{\Re(r_\alpha)}\right). \tag{A.3}$$

which allows to calculate the expected delta in phase jumps

$$\Delta\delta_\alpha = \delta_\alpha(n_{e0} \cdot a_{n_e}, \tau_0 \cdot a_\tau) - \delta_\alpha(n_{e0}, \tau_0) \tag{A.4}$$

depending on a distortion of the electron density or the collision time. It is useful to describe the phasejump as a delta, since a phase picture will always have an arbitrary offset, since it is not possible to define the absolute phase of one position. This delta would be visible as a distortion of a phase in a phase image. If the parameters of the Drude-Model have been fitted to experimental values of the refractive index, like for example for Au in the range from 100 nm to 1200 nm (fig.A.1) one obtains values for $n_e = 5.847\,109\,268\,173\,177 \times 10^{28}\,\mathrm{m}^{-3}$, $\tau = 3.0916 \times 10^{-14}\,\mathrm{s}$ and $m^* = 1.1216 m_e$, which are all within the range of measured values [90]. Accordingly, the phase distortion resulting from the electron density and collision time variation can be plotted according to (A.4) as shown in the figure A.2. It can be seen that in order to produce a significant phase jump, the collision time must decrease by several orders of magnitude, or the free electron density must drop to a tenth.

A.3 Phaserings Described by Drude Model

The now proposed explanation for this involves electron movement according to the Drude model (section 2.3). It is fair to assume that there may be electron density perturbations disrupting this area together with the thermal effects taking place at timescales of a few picoseconds [92]. As described in section 2.3 such a perturbation (either in electron density, or in temperature) changes the refractive index of a metal. Figure A.3 displays the areas of fig. A.2 where the delta in phase shift matches the phase shift of the rings of $\Delta\varphi \approx 0.1\,\mathrm{rad} \pm 0.02\,\mathrm{rad}$. Since the probe beam is p-polarized towards the target, the purple area gives the possible combinations of

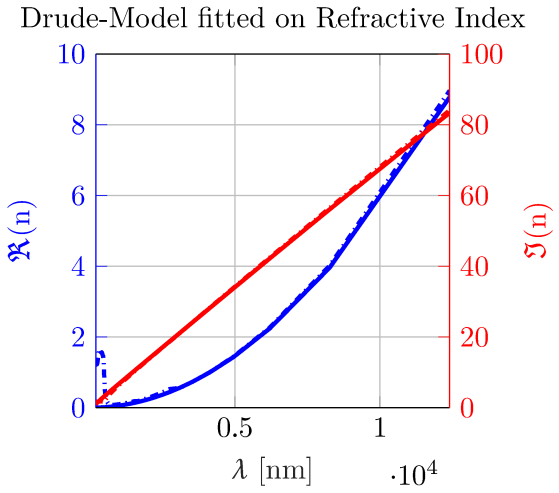


Figure A.1: Drude Model fitted to experimental values of the refractive index of Au [91]. Fitted parameters are $n_e = 5.847\,109\,268\,173\,177 \times 10^{28}\,\mathrm{m}^{-3}$, $\tau = 3.0916 \times 10^{-14}\,\mathrm{s}$, $m^* = 1.1216 m_e$.

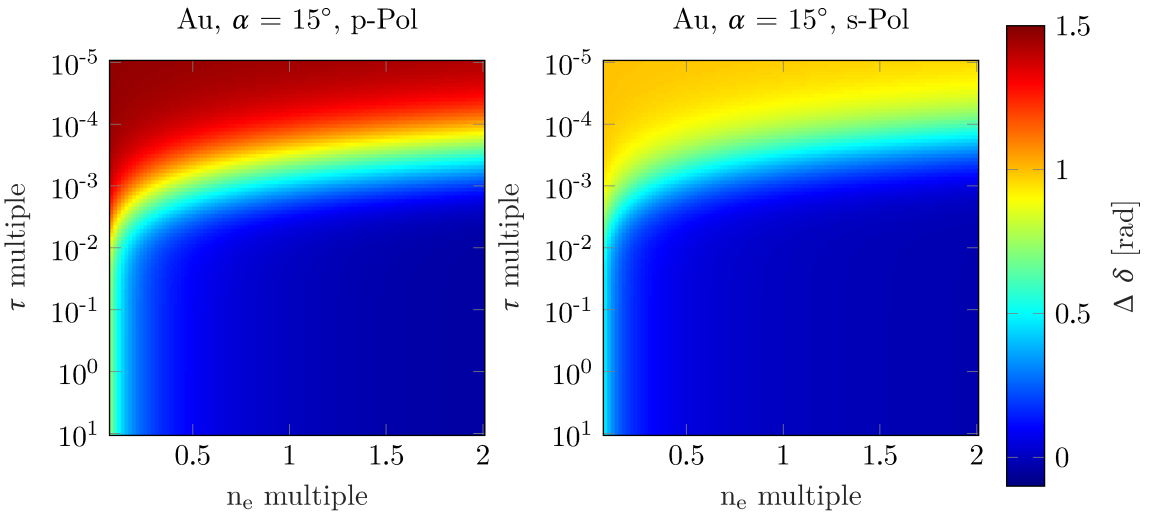


Figure A.2: Difference in phase shift due to collision time τ and electron density n_e variations. A considerable shift is obtained at electron densities of 0.1 times of the original density as well as collision times 100 times lower than the original τ.

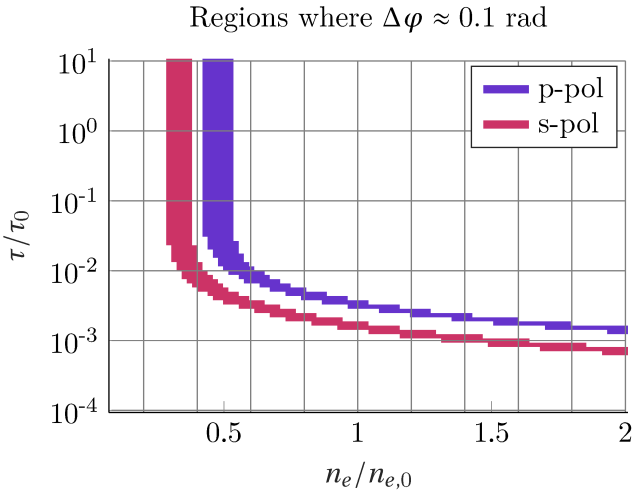


Figure A.3: Subset of Fig. A.2. Combinations of collision time τ and conduction band electron density n_e perturbations that lead to a phase shift of $\Delta\varphi = 0.08\,\text{rad}$ to $0.12\,\text{rad}$ according to the Drude model.

collision time and electron density perturbation which would predict such a shift. Assuming the collision time stays constant this would need a loss in conduction band electrons of about 50%. Otherwise, if the electron density stayed constant, this would need a shorter collision time i.e. higher collision frequency between two and three orders of magnitude.

Appendix B Pulse Contrast Measurement

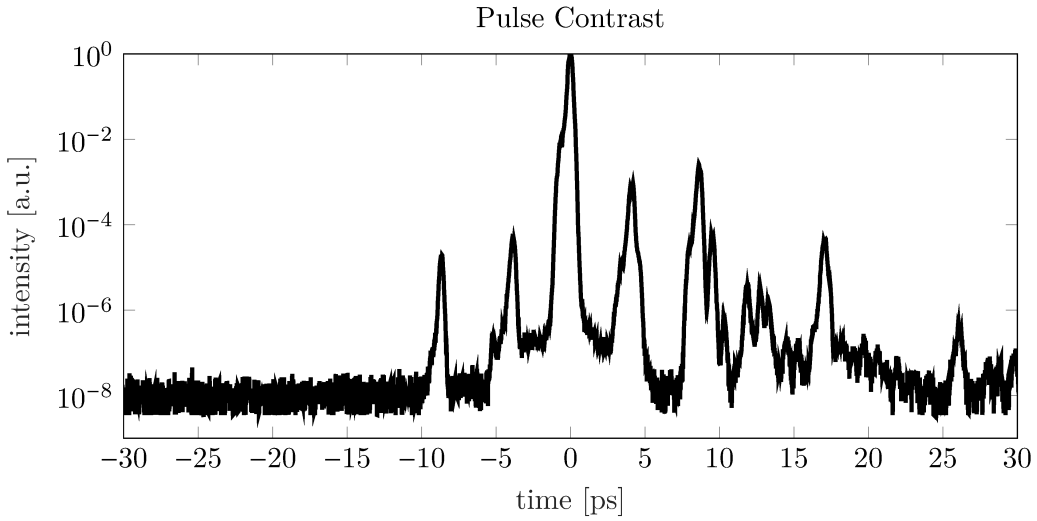


Figure B.1: Sequoia measurement to determine pulse contrast for the experimental setup.

To analyze the pulse contrast of the laser system, a Sequoia [59] measurement was conducted. The Sequoia was placed in air, before compression, but with full bandwidth. The laser pulse was additionally attenuated and spectrally squeezed to accommodate the working environment of the Sequoia. fig. B.1 shows that the overall pulse contrast reaches the resolution limit of the Sequoia of 10^{-8}, which implies that the pulse has at least a contrast of eight orders of magnitude. The spikes that can be seen symmetrically around the main pulse at $t = 0\,\mathrm{ps}$ have a constant distance of $\Delta t = 4.4\,\mathrm{ps}$, which implies that those are ghost artifacts, presumably due to inner reflection inside the BBO crystal. At a crystal length of 400 µm those re-reflections, interacting with the reference beam would result in the given symmetrical pattern.

Appendix C Carbon Crater Corona

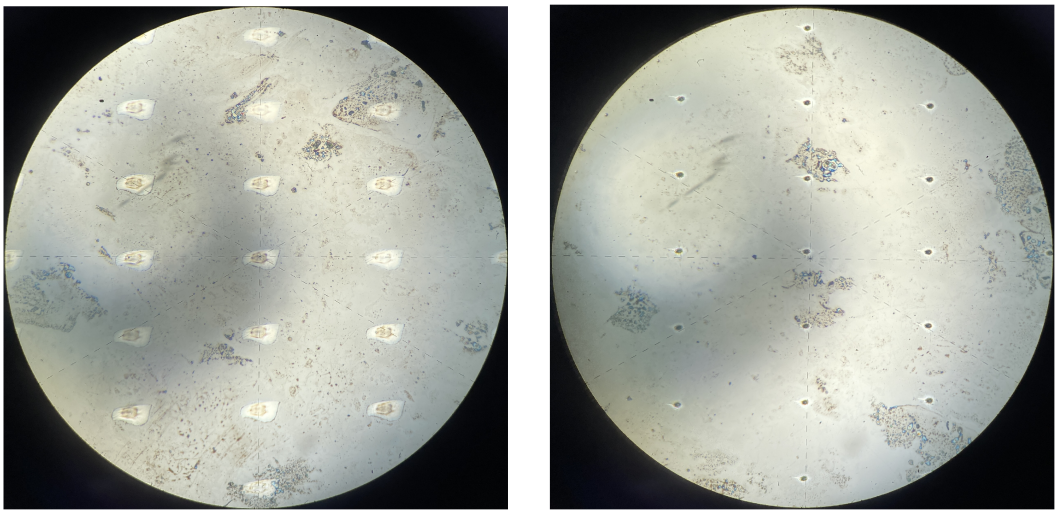


Figure C.1: Craters on carbon target under microscope. Left image shows corona around the craters, right image does not.

fig. C.1 shows microscopic images of craters on the glassy carbon target. The left image has coronas around the craters ($\varnothing \approx 80\,\mu m$) while the right does not. The right image displays craters from the measurement series, that was used in this thesis, while the left image contains images from a series when the imaging apparatus got aligned and is thereby not suitable for evaluation. Since the laser parameters are usually identical between each workday, it is currently not fully explained why at most work-days the craters have coronas, and some days they do not. It is highly suspected that it is related to the ASE, since this parameter cannot be measured daily and could have a slightly different divergence, therefore creating a bigger spot in the focal plane.

Appendix D Correlation and Error Analysis of Phase Movements

In figure 5.2 can be seen that the phase appears to exhibit slightly oscillatory behavior in the later stage of the plasma (especially for Au, if the window for the moving mean is taken a bit smaller). In this chapter shall be discussed, where this may or may not come from. As previously described, the phase images where automatically analyzed by fitting a 2D-Gaussian shape to the plasma. While this shape is not a sufficient fit, it nevertheless can give insights about the general behavior of the plasma. The first obvious metric is the middle point of the plasma, which is shown on the left plot in Fig. D.1. It can be seen that the movement in x and y direction have some kind of oscillatory change underlying the relatively high noise level. This can be seen very well when looking at the floating mean (red and blue lines). Also the FWHM does seem to change periodically. This shall not be confused with the actual width of the plasma. This value just represents the FWHM of the Gaussian fit, thereby indicating a real change in plasma width, but not directly corresponding to it. Especially interesting is the fact that the position and FWHM seem the change drastically around the 6 ps mark, which also is the mark where the oscillatory behavior in the phase seems to start.

A typical explanation, why the central position changes with time is a tilted target. Since every shot is performed at at new position and those positions are all inside a rectangle, if the target is slightly tilted or not perfectly flat, the position slowly changes while moving along one axis.

Now the question arises, if the change in position does correlate with the change in phase. Looking at left fig. D.2 the normalized phase does not seem to share a similar oscillation as the center position or FWHM. And when analyzing the frequencies in the right plot, there also do not seem to be any matching pattern between phase and both center position and FWHM.

In fig. D.3 correlation plots for phase-center, phase-FWHM and FWHM-center are shown. It can be seen, that for the phase-center plot there seems to be some kind of underlying function - a line with little variance weaves between the upper and lower bubble. This does not look random, but also not easily correlated. The same goes for the phase-FWHM plot, again it does not seem to be completely random, rather, one can see that for high phase values the FWHM seems to be more random. However this does not give information about the oscillatory behavior of the phase. For the sake of completeness also the FWHM is plotted against the phase which does seem to be completely uncorrelated.

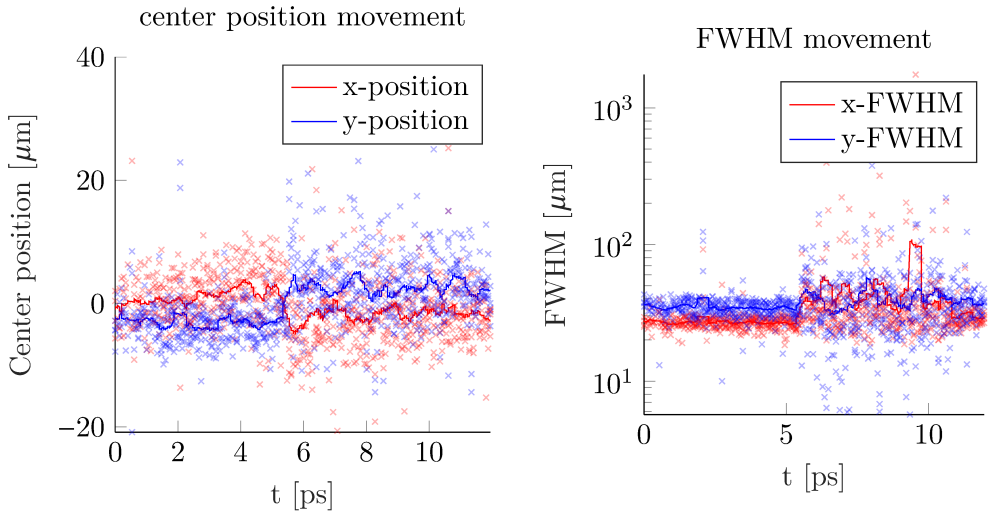


Figure D.1: Left: Movement of the central position of the Gaussian fit of the plasma. Right: FWHM of the Gaussian Fit.

Also it shall be discussed why the variances of the central plasma position are unexpectedly high. The floating mean of the central position (fig. D.1) has a variance of $\sigma_x \approx 2.8\,\mu\text{m}$ and $\sigma_y \approx 7\,\mu\text{m}$ with an overall variance of all the data points of $\sigma_x \approx 14\,\mu\text{m}$ and $\sigma_y \approx 26\,\mu\text{m}$. Those variances are much higher than the actual movement of the focus position. On one hand this can be attributed to the comparably low spatial resolution of around $10\,\mu\text{m}$. Therefor a variance in that range would be expected. Also interesting is that the variance changes after the edge at $t \approx 6\,\text{ps}$ from $\sigma_x(t < 5.5\,\text{ps}) \approx 10\,\mu\text{m}$ to $\sigma_x(t > 6\,\text{ps}) \approx 18\,\mu\text{m}$. The same goes for the y-axis with $\sigma_y(t < 5.5\,\text{ps}) \approx 13\,\mu\text{m}$ to $\sigma_y(t > 6\,\text{ps}) \approx 28\,\mu\text{m}$. Thus it can be assumed that for early plasma the fitting function works as good as possible, since it is just as precise as the resolution. For later plasma, after the edge, there seems to be a problem however. It would be quite unexpected if the fitting function suddenly stopped working correctly. More plausible seems that there is a problem with the experiment. It could be a malfunction of the beam stabilizer at the front of the laser system, which always produces more inconsistent beam parameters. Or it could be a problem with the motors of the target, or the target itself, resulting in a slight tilt, which would produce exactly the measured results.

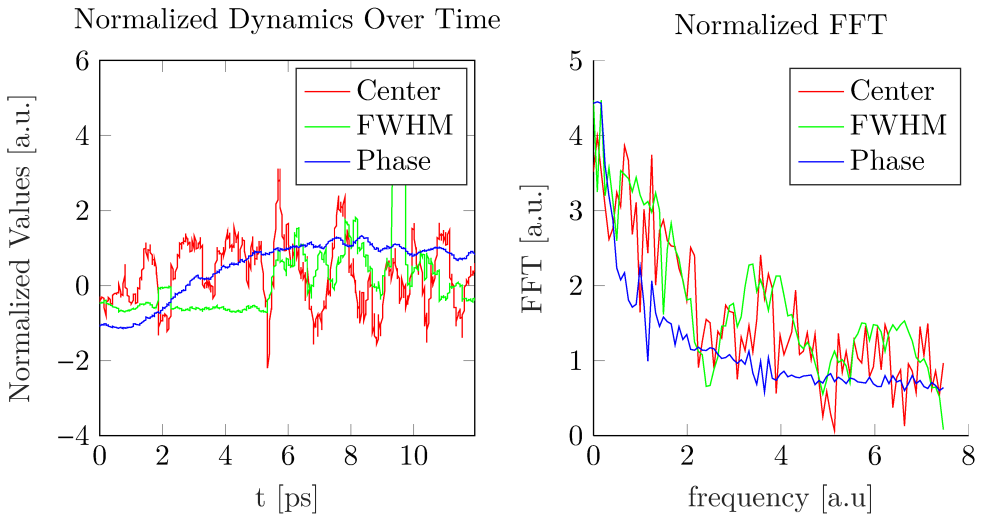


Figure D.2: Comparison between center position, FWHM and measured phase. Left in real space, right in Fourier domain.

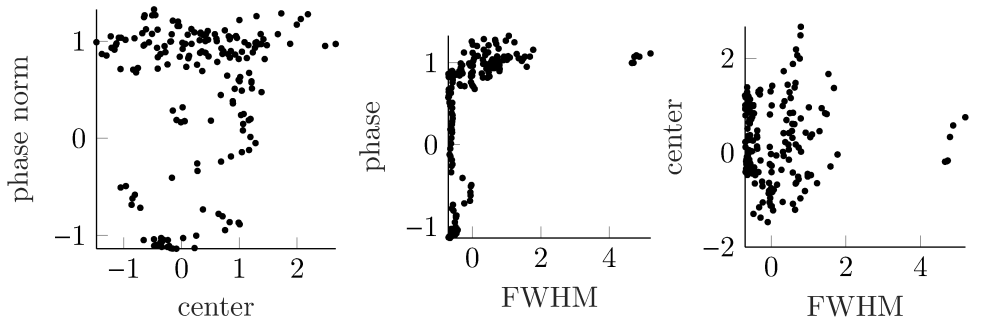


Figure D.3: Correlation plots between phase, center position and FWHM.

Appendix E Multi-fs: Practical Configuration Notes

This appendix summarizes the practical configuration of the Multi-fs code [66] used to produce the results in section 4.1, intended as a reference for future use of the code.

The fort.12 file specifies the plasma model and its parameters, as well as the target material (atomic number, atomic weight, and density). For all simulations, the Drude-Sommerfeld model [67] was selected, with non-reflective boundaries, radiation and hydrodynamic transport enabled, and a p-polarized pulse introduced at $\alpha_i = 45°$.

The fort.13 file contains the ionization-state, EOS, and opacity maps as functions of temperature and density. The EOS maps used are taken from the aluminum baseline for all target materials, since the electron EOS is essentially identical across materials, while the ion EOS contributes negligibly to the results of interest. The ionization states were computed with a Saha solver similar to that of Zaghloul [46], implemented by Riedlinger [47].

Complete simulation output is stored in fort.10, from which all lineouts and plasma-shape reconstructions in section 4.1 were extracted.

Since the code runs in cgs, the input peak intensity $P_0 \approx 8.6 \times 10^{17}\,\mathrm{W/cm^2}$ has to be input as $P_{max} = 8.6 \times 10^{24}\,\mathrm{erg\,cm^{-2}s^{-1}}$.

For the opacity maps, κ is given in units of $\mathrm{cm^2/g}$, while ν and T are in eV. Normalization constants cancel and are omitted, since both κ^R and κ^P are normalized quantities.

Appendix F Plasma Shape Fitting

Fitting functions to the Multi-fs plasma shape simulation with a simulated ideal laser intensity profile in focus are evaluated in fig. F.1

First the laser intensity profile in the focal position was simulated. The parameters are consistent with the actual shape and intensity measurements of the laser (see section 3.2), just a bit smoother. Using those local intensities the Multi-fs simulation calculated the propagation of the critical density for each point in 1D. This is obviously only an approximation which could be suitable for early plasma, while the scale length (i.e. position of the critical density) is smaller than the width of the plasma. Since we know that within the first 10 ps the critical density propagated about the same length as the width of the plasma, it should be assumed that the simulation overestimates the size relatively early. Nevertheless the approximate shape can be estimated (fig. F.1).

The evaluated shapes are a Gaussian

$$G(x) = Ae^{-\frac{x^2}{2\sigma^2}} + B, \tag{F.1}$$

a Super-Gaussian

$$SG(x) = Ae^{-\left(\frac{x^2}{2\sigma^2}\right)^p} + B, \tag{F.2}$$

and a Half-Sphere

$$HS(x) = \sqrt{A^2\left(1 - \frac{x^2}{\sigma^2}\right)}, \forall |x| > \sigma. \tag{F.3}$$

It can be seen, that the Super-Gaussian outperforms both other functions. This holds true for all relevant plasma life-times. The shape does not significantly change, as discussed in section 4.1, only the height A depends on the time.

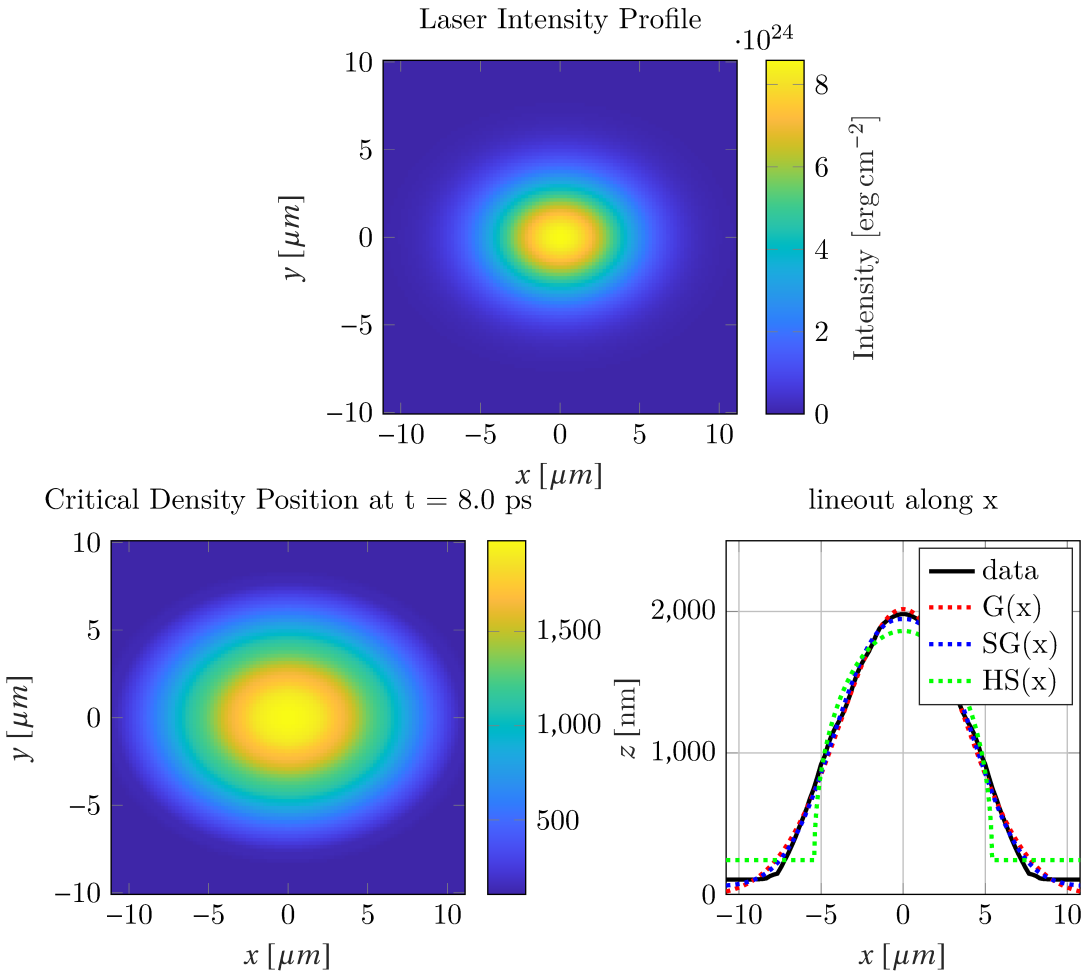


Figure F.1: Top: Simulated Laser profile. Bottom Left: Plasma shape according to Multi-fs with the given laser profile. Bottom right: lineout through the middle with different fitting functions.

Appendix G Electron Density Model for a Plasma Bubble

We define a piece-wise function $\rho(x)$ to model a density profile with a constant value for $x < -b$ and an exponential decay for $x \geq -b$. The function is given by

$$\rho(x) = \begin{cases} \rho_0, & x < -b, \\ \rho_0 \exp\left(-\frac{x+b}{L}\right), & x \geq -b, \end{cases} \tag{G.1}$$

where ρ_0 is the constant density for $x < -b$, b is the transition point, and L is the scale length. The function is continuous at $x = -b$ since both pieces yield $\rho(-b) = \rho_0$. Moreover, the total integral of $\rho(x)$ from $x = -d_0$ to ∞ (with d_0 being the depth of the plasma which assumes to be equally ionized plasma) should contain the amount of electrons in the plasma and should therefor be constant

$$\int_{-d_0}^{\infty} \rho(x)\, dx = N = const.,$$

wherefore

$$\int_{-b}^{0} \rho_0 dx = b \cdot \rho_0 \stackrel{!}{=} \int_{-b}^{inf} \rho_0 \exp\left(-\frac{x+b}{L}\right) = L \cdot \rho_0$$

which is only true if $b = L$, which allows the simple expression

$$\rho(x) = \min\left[\rho_0, \rho_0 \exp\left(-\frac{x+L}{L}\right)\right] \tag{G.2}$$

which is now only depending on the scale length.

For the simulated parameters in fig. 4.2 this predicts a critical density position of $x(n_c) \approx 3.5 \cdot L$ which is comparable to the actual value seen in the figure. Without better knowledge this approximation would therefor be suitable.

The same approach applies to a 3D gradient (4.8), with the new

$$\rho_0 = \frac{N}{8\pi L^3}$$

to ensure

$$\int_0^{2\pi}\int_0^{\pi}\int_0^{\infty} \rho_0 e^{-r/L} r^2 \sin\theta \,\mathrm{d}r \,\mathrm{d}\theta \,\mathrm{d}\varphi = N = const.$$

In figure G.1 the OPD between a plasma initially forming around $x = 0$ and a beam traveling through vacuum and reflecting at $x = 0$ is plotted. It is observed

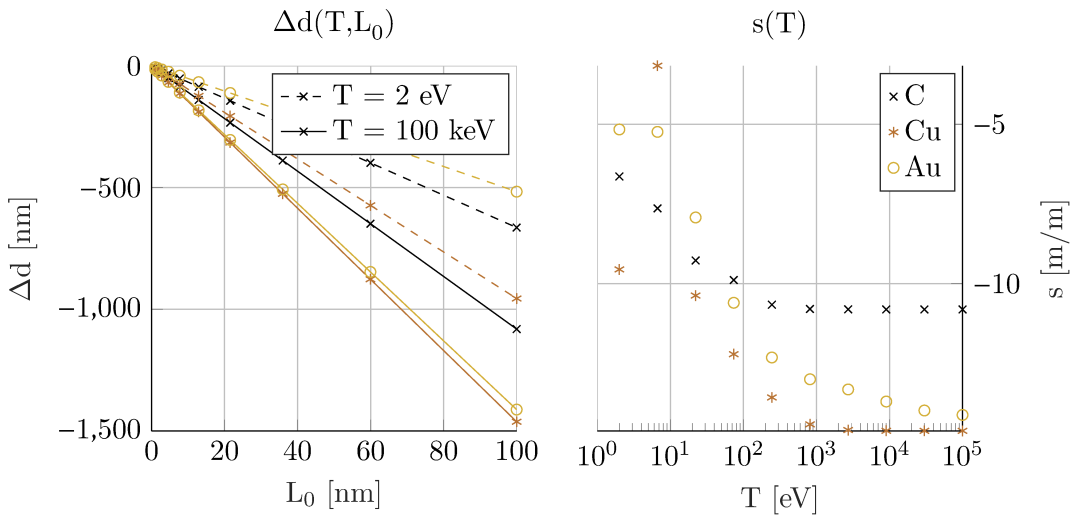


Figure G.1: Left: optical path difference $\Delta d(T, L_0)$ depending on the plasma size L_0 for different plasma temperatures T are fitting a linear function $\Delta d = s(T) \cdot L_0$. Right: Slope $s(T)$ as OPD per scale length of the 1D plasma gradient in [m/m], since the slope $s(T = const.) = const.$ In difference to fig. 4.11, this includes the critical density in the scaling factor.

that only for temperatures high enough the plasma gradient is able to curve the beam away from the critical density. Those temperatures are in the range of 2 eV to 100 keV. This figure is similar to the figure 4.11, the only difference is, that the scaling factor here already incorporates the position of the critical density (as an approximation with above given G.2). Whereas 4.11 evaluates only the OPD in front of the critical density (i.e. the critical density is set at $x = 0$) thus allowing better approximations as the movement of the critical density can be simulated independently. In practice those differences are neglectible. When inverse calculating the position of the critical density from the OPD the here described scaling factor of $s \approx 10$ is just as precise.

Appendix H Diffraction Integral Evaluation

In section 4.4.6, the diffraction algorithm used to evaluate the phase images after propagation through the lens system is established.

Here, the algorithm is tested and presented in a more illustrative form. fig. H.1 shows how high NA (generated by varying the focal length at a constant aperture) can perfectly reproduce the original phase profile according to theory. There, the height of the wave fronts (i.e., the phase) is completely preserved, and the spatial size of the structure (the super-Gaussian profile) is scaled by the calculated magnification $V = \frac{b}{g}$. It can also be seen how higher phase perturbations are compressed at lower NA. There a reduction in NA not only increases the compression but also changes the threshold at which compression begins.

The simulation parameters were $V = 20$, $\lambda = 800\,\mathrm{nm}$, spatial resolution $\mathrm{d}r = \frac{\lambda}{20}$, aperture radius $r_{ap} = 12.8\,\mathrm{mm}$, the intensity beam width $\sigma_I = 0.1\,\mathrm{mm}$, and the intensity height $I_{max} = 1$. The plasma bubbles (i.e., the shape of the phase) were super-Gaussian with a width of $\sigma_{plasma} = 3.8\,\mu\mathrm{m}$ and $p = 1.36$. The height of the Super-Gaussian distribution was varied in the range of the simulated perceived plasma height (i.e. Multi-fs + ray-tracing) between $\phi_{0_in} = 0.1\,\mathrm{rad}$ to $200\,\mathrm{rad}$. The plots show $\Delta\phi_{out} = \phi_{out}(\phi_{0,in} = ...) - \phi_{out}(\phi_{0,in} = 0)$, which means that the phase of the output field of an input field without plasma (i.e., $\phi_{0,in} = 0$) is always subtracted from a field with plasma, thereby eliminating all field curvatures that were not generated by the plasma but by the carrier field. This essentially corresponds to the interference of two beams, one with and one without plasma. The influence of the carrier field is usually extremely small; it normally contributes only a small amount of total curvature.

Notes about the importance of some input parameters:

- While the height of the plasma bubbles was the most important parameter for this work, the diffraction/diffusion of the phase profile technically results from its initial curvature/inclination. The higher the slope, the faster the phase is cut off, resulting in compression. Since the plasma size here appears to be very constant (according to Multifs simulation), only the effect of the resulting variation in plasma height is considered. If the plasma were to expand (or contract) in width, these calculations would have to be repeated accordingly.
- The sampling of $\mathrm{d}r$ does not really depend on λ, but rather on the slope of the phase. This means that it is important to choose the phase steps small enough to obtain correct results without creating random reversals in the

output phase. It is often not sufficient to consider only the intensity of the output field, since a "negative" phase (or an incorrectly calculated phase) often does not lead to an incorrect intensity.

- The curvature of the input field is generally not important (in all reasonable imaging systems). This means that it does not matter if the curvature caused by the parabola, which focuses the beam in the plasma region, has a different focal length and therefore curves the phase more strongly, or if the input curvature is completely neglected. Since the image plane contains an image of the plasma and the reference beam contains the information about the "background curvature", these effects can usually be neglected.
- It is important that the intensity profile is sufficiently wider than the phase profile, otherwise information within the lens may be lost. Once the intensity profile is sufficiently large, the shape of the profile no longer matters (except in some random cases where the diffracted intensity can become exactly zero, which can lead to jumps in phase or problems unwrapping the phase from $[-\pi, \pi]$).

Additional notes: Sometimes the algorithm fails (presumably) due to numeric reasons in the phase space, creating unexpected patterns (for example, for $\mathrm{d}r = \frac{\lambda}{5\pi}$ for different NA it was observed that if $\phi_{0,in} = 2\pi$ the phase-profile became negative, instead of the compressed Super-Gaussian shape. But only for some focal lengths (i.e. NA), but if dr or $phi_{0,in}$ was chosen slightly differently the anomaly disappeared again. For the presented data those effects happened ($\mathrm{d}r = \frac{\lambda}{20}$) sometimes for $\phi_{0,in} = 20$ and $\phi_{0,in} = 40$ (the steps can be seen in the bottom right PTF graph in fig. H.1). I assume there are sometimes numerical anomalies if the phase gets sampled unluckily and unexpected interference patters occur. I experimented with different irrational numbers to create $\mathrm{d}r = \frac{\lambda}{x}$ to minimize those effects, but even tho almost all output phase-fields did not react to those changes, some of them sometimes flipped, usually with some connection to the chosen fraction (i.e. if $x = n * pi$ some values related to π flipped, but not necessary). The flipping was just observed for large $\phi_{0,in} > 2\,\mathrm{rad}$, thus the assumption it is related to unlucky slope-sampling.

The next bunch of figures fig. H.2 and fig. H.3 had the focal length of the lens fixed with $f = 15\,\mathrm{cm}$ (like the experiment) and the size of the aperture is varied. It was observed, that the PTF for the same NA is similar no matter if f or r_{ap} are varied (compare NA = 0.08 and 0.04). The overall behavior is therefor similar (if not identical) to the previous figures, wherefore it seems as if the NA is usually an sufficient indicator of the performance of the lens system in phase-space, similar to

intensity-space.

From those figures, the maximal compression was obtained, displayed in fig. H.4 and fig. H.5. Here the PTF is fitted for different NA, since the numerical simulation created some edges which seem unphysical and create wave-like structures in time on the input phase/plasma size. Those figures shall document that a fit with a function of the form

$$\phi_{out} = a(1 - \exp\left(-\frac{\phi_{in}^{c}}{b}\right) \tag{H.1}$$

is reasonable and expresses the simulated behavior to an accurate degree. Both figures show effectively the same graphs, the latter is only zoomed in on the smaller input phases, to show that the fit is reasonable for small and huge compression.

Additionally fig. H.6 shows the limit of the compression. Since all the functions become very flat for high ϕ_{in}, the values of $\phi_{out}(NA, \phi_{in} = 200)$ are plotted. This function can be used as an approximation for the numerical aperture of a system, when the phase reaches a plateau and compression is suspected as the reason, then the height of the plateau gives the NA.

Also shortly discussed shall be the ripples in the phase for small NA (see fig. H.3, NA = 0.024 and 0.015). one may assume that those ripples are connected to the observed phase rings (see section 5.3). I presume it to be unlikely tho, since those ripples get more prominent with a higher input phase $\phi_{0,in}$ (i.e. higher compression), but in the experimental results the rings disappear later on (when the higher compression is supposed to happen). Therefore I assume it to be highly unlikely that those are the same effects. Also the current assumption is compression due to NA $\approx$ 0.03 where those ripples are not as prominent as in the experiment.

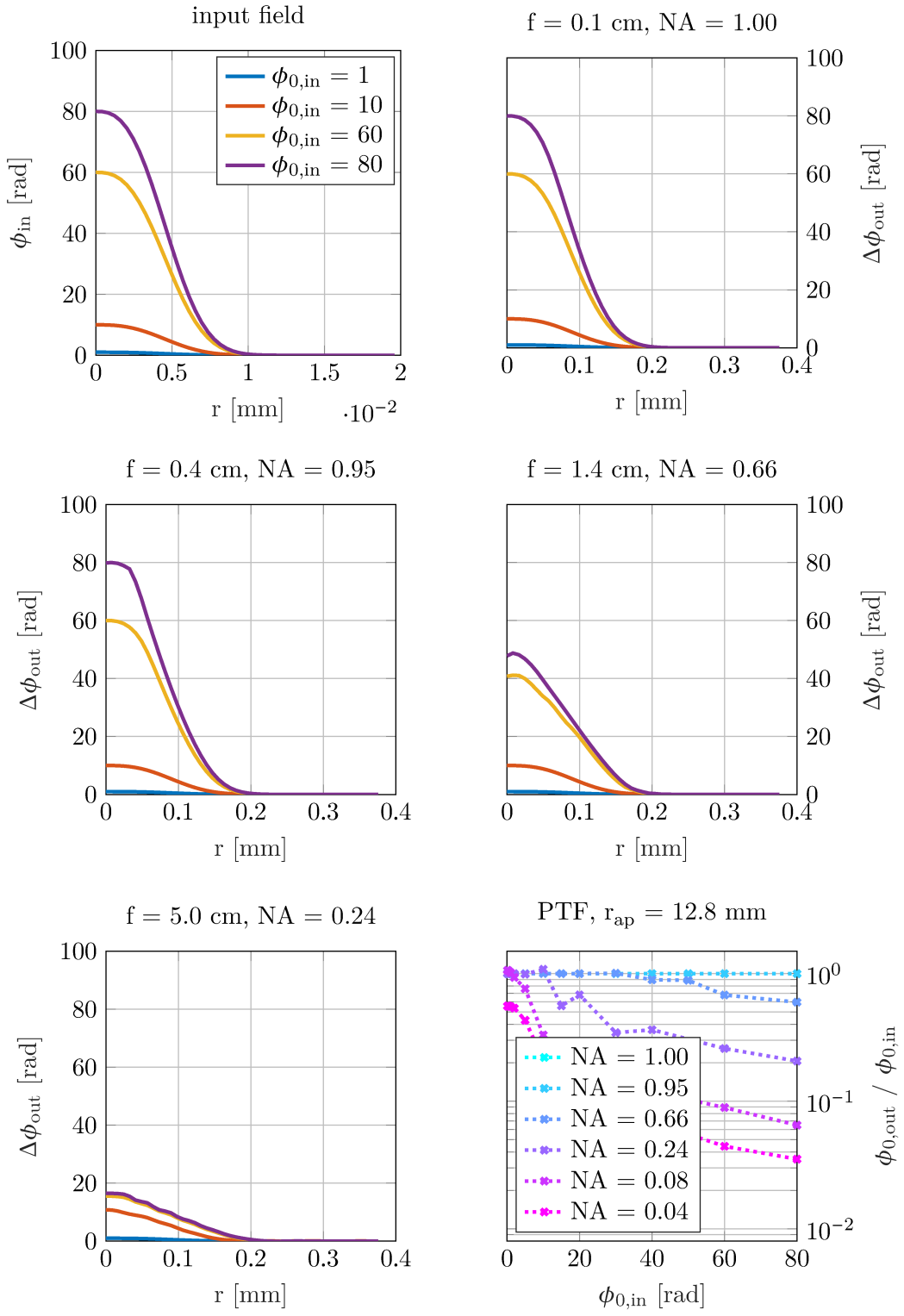


Figure H.1: Top left: phase profile of input fields with different heights. Top + middle right, middle + bottom left: phase profile of output fields of the respective input fields, after imaging with given NA and f. Bottom right: PTF of given NA

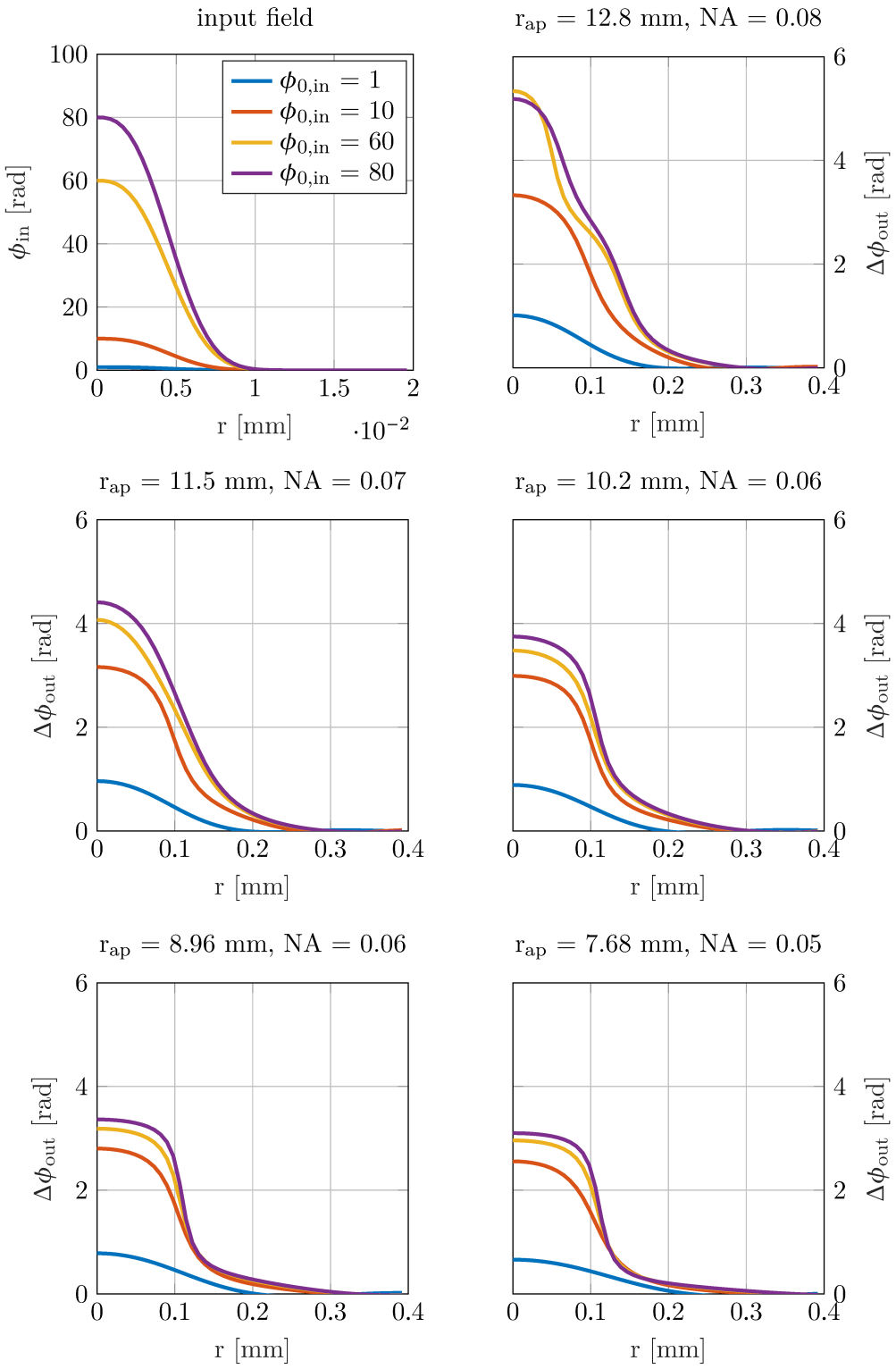


Figure H.2: Top left: phase profile of input fields. Everything else: phase profile of output fields of the respective input fields, after imaging with given NA and r_{ap}.

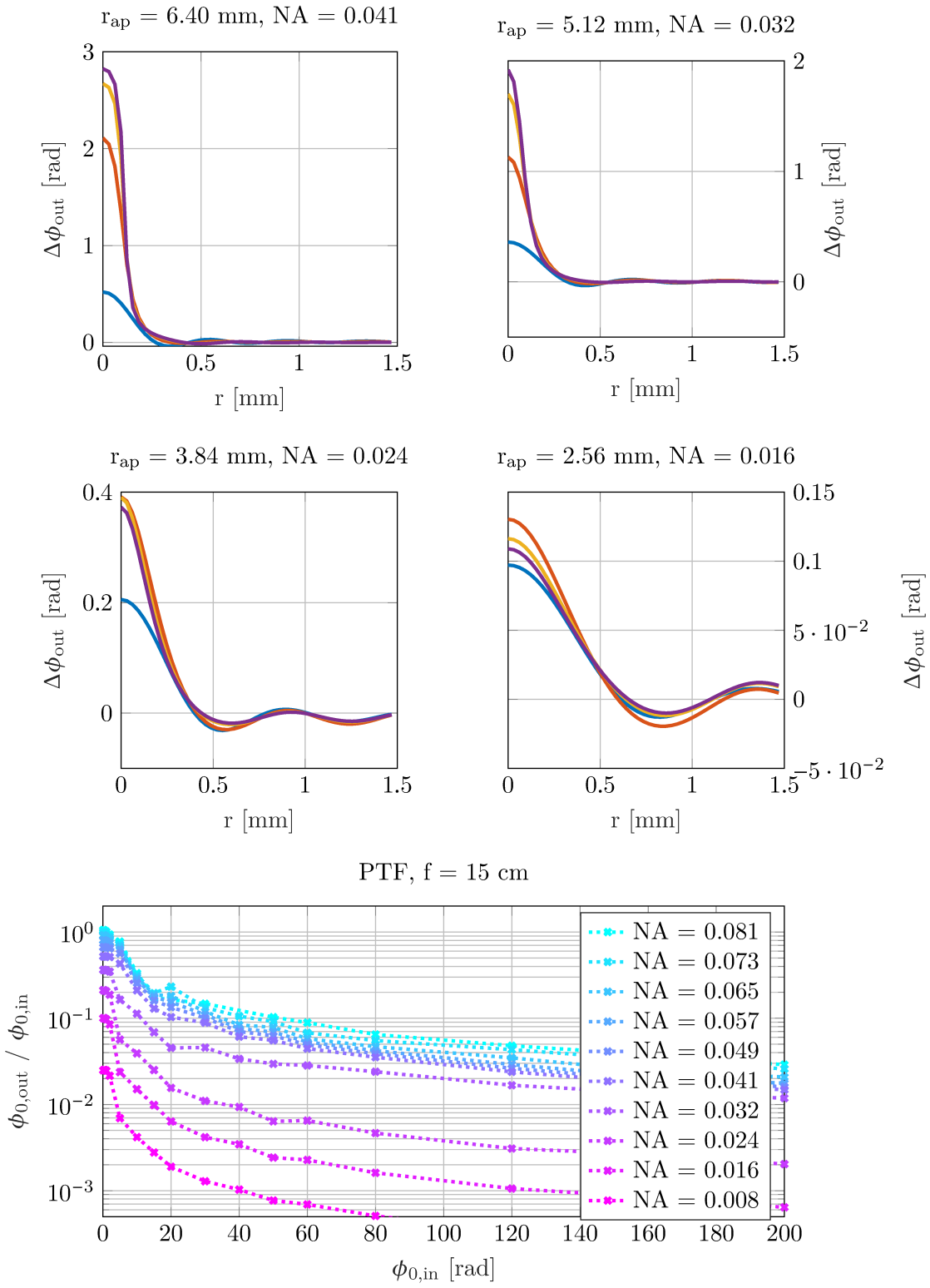


Figure H.3: Continuation of fig. H.2. Bottom graph: PTF of given NA

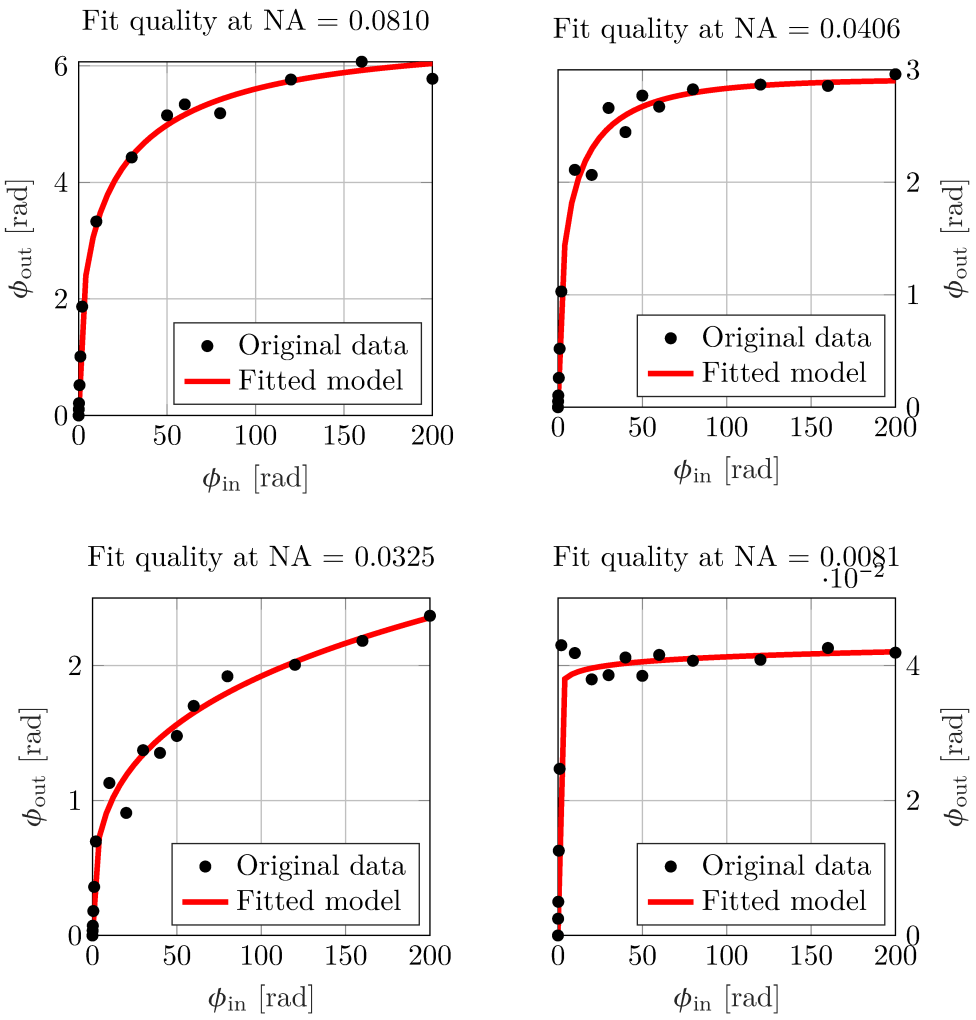


Figure H.4: Fit of inverse PTF for different NA.

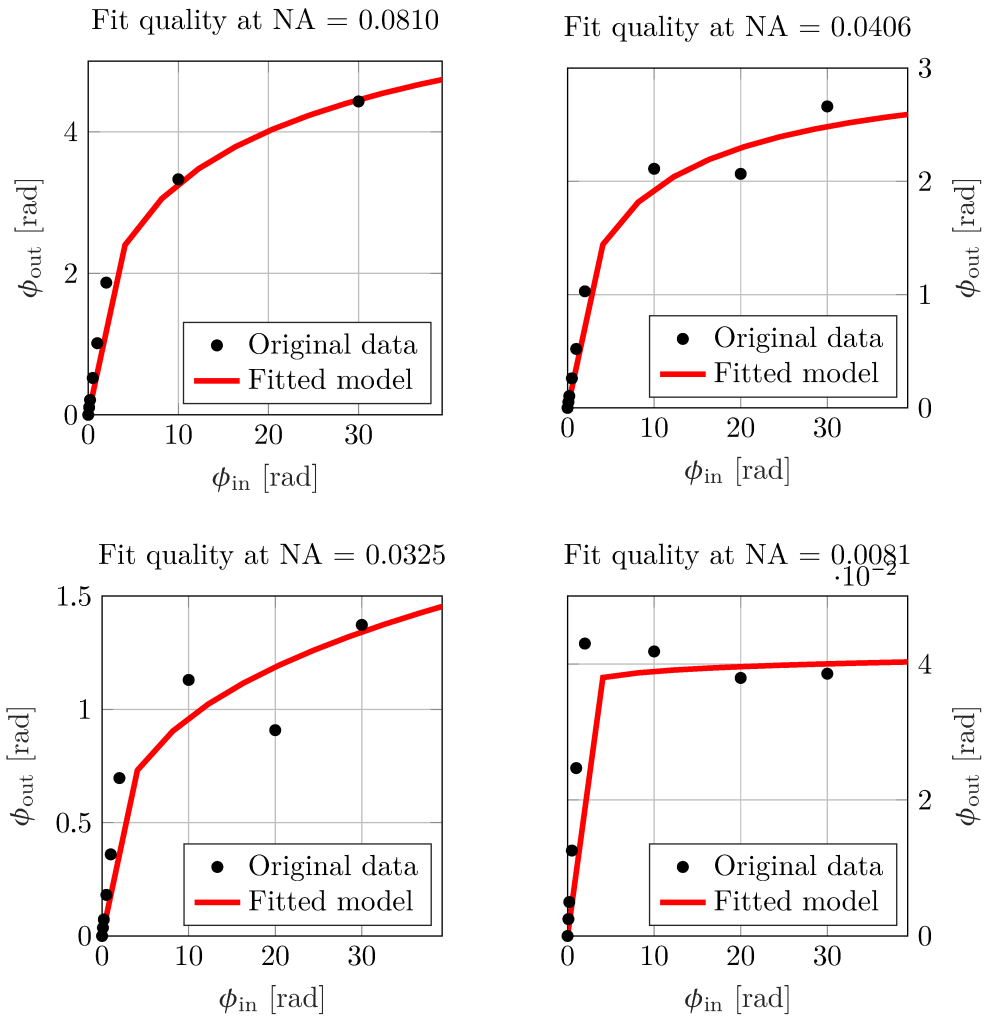


Figure H.5: Same Fit of inverse PTF for different NA as in fig. H.4, but zoomed onto the smaller phases.

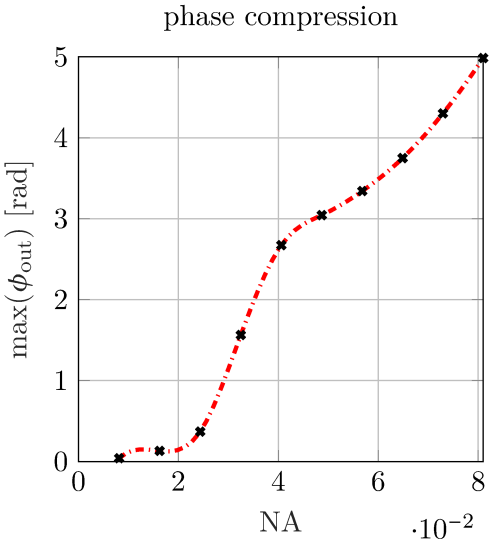


Figure H.6: Ceiling of fit given in fig. H.5 and fig. H.4. Predicts maximal measurable phase after compression by NA.

Appendix I Analyzing Different Simulation Combinations

Since the implementation of the ray-tracing algorithm has to my knowledge never appeared in any literature before, it has to be analyzed with utmost rigor. Therefore the experimental results were compared to different configurations of simulations to determine if the simulations are actually improved to fit the measured data. fig. I.1 shows the experimental data overlayed with different simulation parameters (i.e. the numerical aperture and coupling intensity are varied) when using the Multi-fs into ray-tracing (scaling factor) into diffraction (phase compression) approach.

On the other hand fig. I.2 shows the same parameters, but if only the Multi-fs Data is directly fed into the diffraction simulation.

It is evident that, even tho the fit is not perfect, there is no combination in the Multi-fs-Diffraction simulation, that fits the data better than than the Multi-fs-Ray-Tracing-Diffraction simulation. Thus it seems fair to assume, that the theoretical model of the ray-tracing is not obviously contradicted. However other simulations (most likely the Multi-fs code) predict faster plasma expansion than occurs in reality. For a complete discussion, why the data does not match the simulations see section 5.2.2.

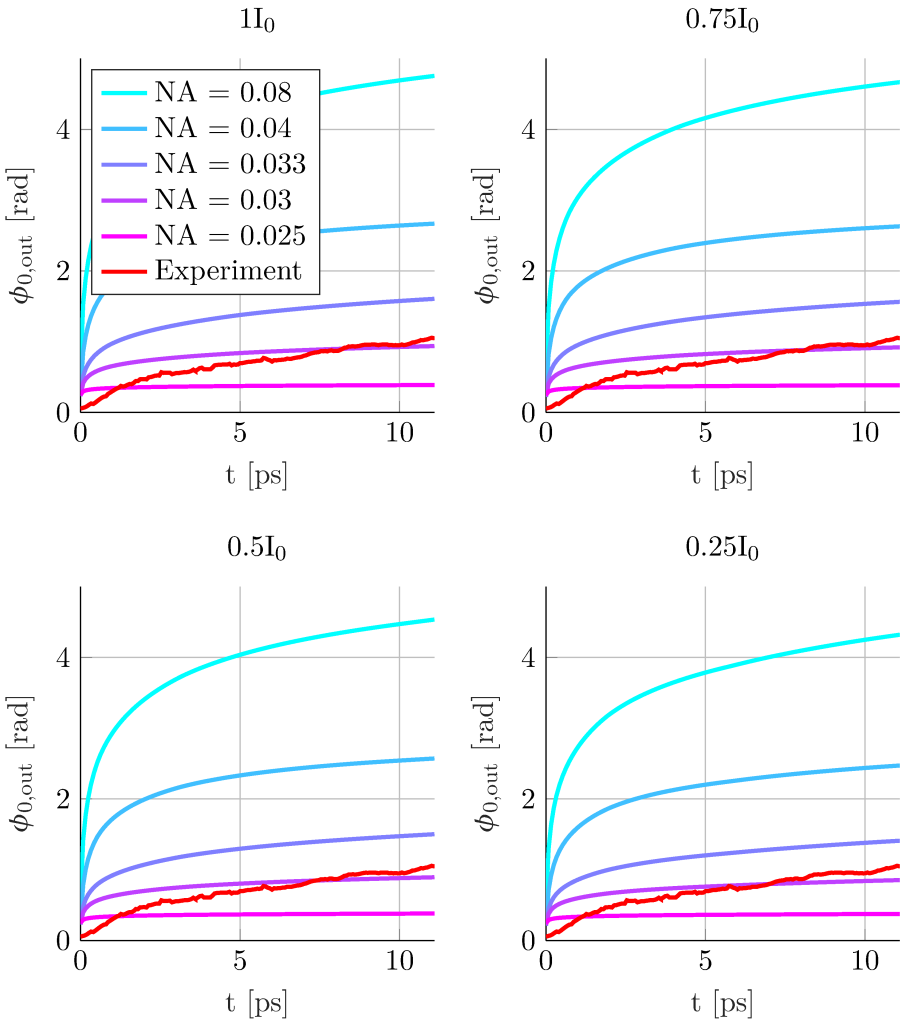


Figure I.1: Multi-fs into Scaling Factor into Diffraction.

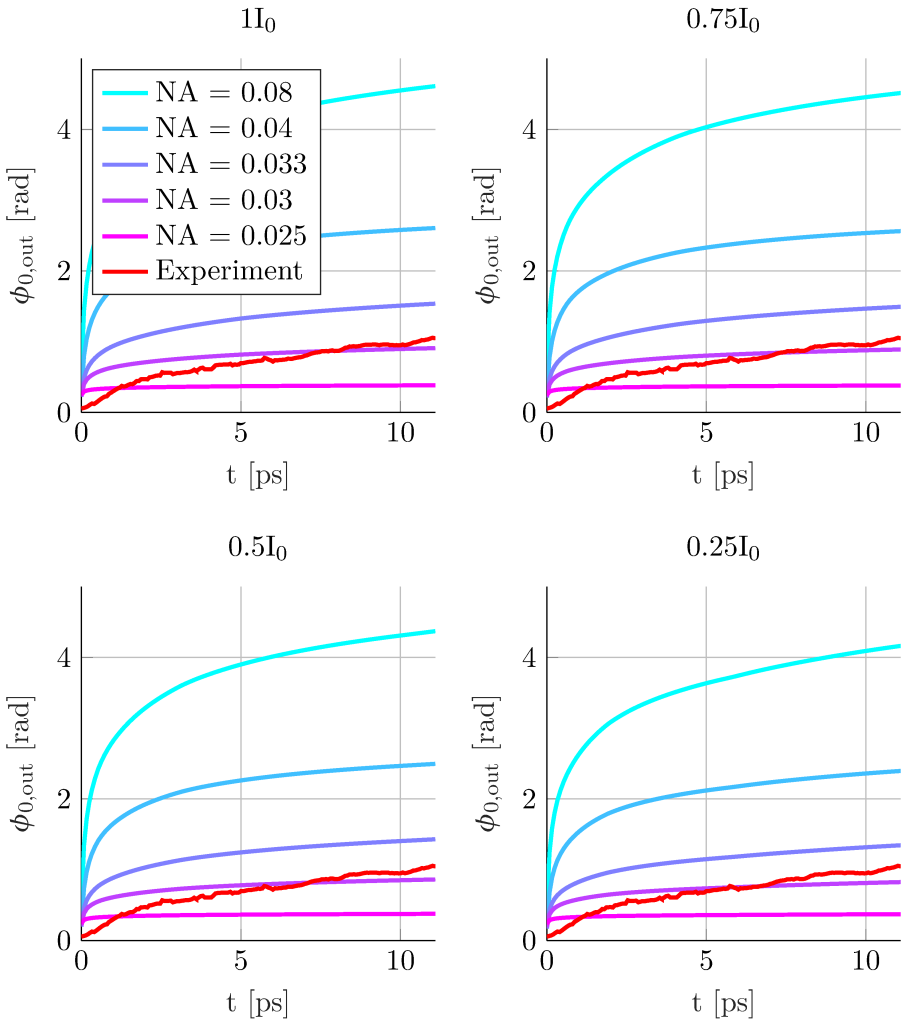


Figure I.2: Multi-fs into Diffraction.

AI Disclosure

This work was proof-read and edited for grammar and semantics with the assistance of the language model Deepl [93].
ChatGPT [94] was used as an advanced search engine and for programming syntax.
Claude's Sonnet [95] was used as an editor to advice on formulations, grammar and overall readability for the reader.
No part of this work's conceptualization or content was generated by AI, all intellectual work originates from the author.

Danksagung

So nun diese Arbeit zu ihrem Ende kommt, möchte ich noch meinen Dank ausdrücken an all jene, die mich auf diesem Weg begleitet haben.

An Professor Georg Pretzler, vielen Dank, dass Sie sich stets Zeit nehmen und nie einen vor Ihrer Tür stehen lassen. Für all die Stunden, die Sie uns gelehrt und beraten haben. Für die Zeit, die wir einfach nur plauderten, und dafür, dass Sie geduldig stets an uns geglaubt haben.

An Professor Götz Lehmann, vielen Dank, dass Sie immer so ruhig und bedacht sind, man jederzeit mit Ihnen reden kann, und für all die Programmier-Skills, die Sie mir beigebracht haben. Ohne Sie wäre diese Arbeit nicht möglich gewesen.

An meine Kollegen, Jan und Marc, die ihr von Anfang an mit mir dabei wart. Für all die Jahre, die wir zusammen diskutierten, philosophierten und lachten. Für all die Male, wo ihr mir zugehört habt, wenn ich wieder an der Tafel stand, wenn wir versuchten, neue Theorien zu be- und widerlegen, und die Welt ein bisschen besser zu verstehen.

An meine ehemaligen Studenten, Johanna, Qëndresa, und Nik, die ihr Monate lang mit mir an den Aufbauten justiert, hunderte von Fehlerquellen analysiert und etliche Diskussionen geführt habt, die uns näher an unser Ziel geführt haben. Eure Hilfe und Begeisterung für das Thema war unbezahlbar und unersetzlich.

An Torben, Stefan, und Dirk, für all die schönen Tage, unzählige Sonderanfertigungen, und einen funktionierenden Laser.

Und allen voran an meine Eltern und meinen Bruder, dass ihr mich die ganze Zeit unterstützt und immer an mich geglaubt habt (außer du, Mick). Ohne euch wäre diese gesamte Arbeit nie entstanden, und ich wäre nicht der Mensch, der ich nun bin. Ich kann nicht in Worte fassen, was ich für euch fühle. Ein Danke, gedruckt auf Papier, ist das Einzige, was mir hier möglich ist, doch die Wirklichkeit umfasst so viel mehr.

Declaration

Ich versichere an Eides Statt, dass die Dissertation von mir selbständig und ohne unzulässige fremde Hilfe unter Beachtung der „Grundsätze zur Sicherung guter wissenschaftlicher Praxis an der Heinrich-Heine-Universität Düsseldorf“ erstellt worden ist.

I hereby declare that I have prepared this dissertation independently and that I have not used any sources or aids other than those stated. The dissertation has not been submitted to any other examining body in this or any other form, and it has not yet been published.

Düsseldorf, 09.09.2026

(Nico Potzkai)